REPORT DOCUMENTATION PAGE

Form Approved
OMB NO. 0704-0188

1. AGENCY USE ONLY (Leave Blank)	2. REPORT DATE -	3. REPORT TYPE AND DATES COVERED Technical report

4. TITLE AND SUBTITLE
Locating and Characterizing Unexploded Ordnance Using Time Domain Electromagnetic Induction

5. FUNDING NUMBERS
DAAD19-00-1-0120

6. AUTHOR(S)
Leonard R. Pasion & Douglas W. Oldenburg

7. PERFORMING ORGANIZATION NAME(S) AND ADDRESS(ES)
University of British Columbia

8. PERFORMING ORGANIZATION REPORT NUMBER

9. SPONSORING / MONITORING AGENCY NAME(S) AND ADDRESS(ES)
U. S. Army Research Office
P.O. Box 12211
Research Triangle Park, NC 27709-2211

10. SPONSORING / MONITORING AGENCY REPORT NUMBER
41262.3-EV

11. SUPPLEMENTARY NOTES
The views, opinions and/or findings contained in this report are those of the author(s) and should not be construed as an official Department of the Army position, policy or decision, unless so designated by other documentation.

12 a. DISTRIBUTION / AVAILABILITY STATEMENT
Approved for public release; distribution unlimited.

12 b. DISTRIBUTION CODE

13. ABSTRACT (Maximum 200 words)

A technique for interpreting Time Domain Electromagnetic (TEM) Data was proposed in "Detecting Unexploded Ordnance with Time Domain Electromagnetic Induction" (Pasion, 1999). An approximate forward modeling for the TEM response of compact metallic objects, an inversion for recovering model parameters, and relationships between model parameters and a target's physical parameters were established. These findings were combined to form an algorithm for locating and determining the approximate shape of a buried target.

14. SUBJECT TERMS

15. NUMBER OF PAGES
82

16. PRICE CODE

17. SECURITY CLASSIFICATION OR REPORT	18. SECURITY CLASSIFICATION ON THIS PAGE	19. SECURITY CLASSIFICATION OF ABSTRACT	20. LIMITATION OF ABSTRACT
UNCLASSIFIED	UNCLASSIFIED	UNCLASSIFIED	UL

Locating and Characterizing Unexploded Ordnance Using Time Domain Electromagnetic Induction

Leonard R. Pasion and Douglas W. Oldenburg

March 28, 2001

UBC - Geophysical Inversion Facility
Department of Earth and Ocean Sciences
University of British Columbia
Vancouver, B.C., V6T 1Z4, CANADA

Report Prepared for the US Army Environmental Research and Development Center (ERDC)
U.S. Army Research Office Grant 41262-EV

Contents

Preface

A technique for interpreting Time Domain Electromagnetic (TEM) Data was proposed in "Detecting Unexploded Ordnance With Time Domain Electromagnetic Induction" (Pasion, 1999). An approximate forward modelling for the TEM response of compact metallic objects, an inversion for recovering model parameters, and relationships between model parameters and a target's physical parameters were established. These findings were combined to form an algorithm for locating and determining the approximate shape of a buried target.

A study to evaluate the effectiveness of the technique when applied to Geonics EM63 Time Domain Electromagnetic Sensor data was undertaken as part of the research project "Locating and Characterizing Unexploded Ordnance Using Time Domain Electromagnetic Induction" (41262-EV), funded by the U.S. Army Engineer Research and Development Centre (ERDC). A series of TEM measurements was carried out between April 5 and April 21, 2000 at the ERDC UXO test site in Vicksburg, Mississippi. The data were then analysed at the University of British Columbia Geophysical Inversion Facility in Vancouver, British Columbia, Canada.

The findings of the study are reported here. The report is divided into two parts. Part I reproduces the paper "A Discrimination Algorithm For UXO Using Time Domain Electromagnetics" (Pasion and Oldenburg, 2001) which describes the UXO discrimination algorithm and contains an application of the algorithm to one of the data sets collected at the ERDC UXO test site. Part II contains descriptions of the different Geonics EM63 TEM data sets acquired during the study. The section outlines the tests verifying the applicability of the two-dipole model and concludes with the discrimination algorithm being applied to a number of UXO targets.

Part I

A Discrimination Algorithm For UXO Using Time Domain Electromagnetics

1 Abstract

An assumption is made that the Time Domain Electromagnetic (TEM) response of a buried axisymmetric metallic object can be modelled as the sum of two dipoles centered at the midpoint of the body. The strength of the dipoles depends upon the relative orientation between the object and the source field, and also upon the shape and physical properties of the body. Upon termination of the source field, each dipole is assumed to decay as $k\,(t+\alpha)^{-\beta}\,e^{-t/\gamma}$. The parameters k, α, β and γ depend upon the conductivity, permeability, size and shape of the object, and these can be extracted from the measurements by using a nonlinear parametric inversion algorithm. Investigations carried out using an analytic solution for a sphere and laboratory measurements of steel and aluminum rectangular prisms, suggest the following two-step methodology: (1) The value of β is first used as a diagnostic to assess whether the metallic object is non-magnetic or magnetic, (2) the ratios of k_1/k_2 and β_1/β_2 are then diagnostic indicators as to whether the geometry is plate-like (uninteresting) or rod-like (a high candidate for being a UXO). Results from the application of this algorithm to a TEM field data set acquired at the United States Army Corps of Engineers Research and Development Centre (ERDC) UXO Test Site have successfully identified a UXO to be magnetic and rod-like.

2 Introduction

An explosive ordnance is a munition that is either launched or fired with the intent of detonation at a specified target. An unexploded ordnance (UXO) is an explosive ordnance that, due to some malfunction, remains undetonated. As a result, the ordnance can be found at the ground surface, partially buried, or buried at a depth of up to 8 m beneath the surface. The remediation of UXO-contaminated land has been made a high priority by the United States Department of Defense in order to either maintain safe usage for continuing military operations or to permit land transfer to the private sector. Practical and cost-effective strategies for remediation require both detection of possible targets and the ability to discriminate between UXO and contaminating scrap metal.

The detection of buried metallic objects can be accomplished with a variety of geophysical sensing techniques. Time domain electromagnetic induction (TEM) surveys have been successful in detecting both ferrous and non-ferrous metallic objects near the soil surface, and are a mainstay amongst technologies currently utilized in UXO clearance projects. In the TEM method a time varying magnetic field is used to illuminate a conducting target. This primary field induces surface currents on the target which then generate a secondary magnetic field that can be sensed above ground. With time, the surface currents diffuse inwards, and the observed secondary field consequently decays. The rate of decay, and the spatial behavior of the secondary field, is determined by the target's conductivity, magnetic permeability, shape, and size.

Identification of a UXO from electromagnetic sensor data remains a major hurdle in reducing the high costs of remediation projects. It has been reported that approximately 70% of remediation costs are currently being used to excavate non-ordnance items (Butler *et al.*, 1998). The development of discrimination algorithms can be roughly categorized as either model-based or data-based. Data-based algorithms are pattern recognition procedures that compare a library of catalogued responses from various UXO items to measured responses (for example Damarla and Ressler, 2000). Model-based algorithms use either an exact or approximate forward modeling algorithm to determine a set of model parameters needed to replicate the measured responses, and subsequently relating the model parameters to physical parameters (Khadr *et al.*, 1998). One such model-based technique that has been the focus of much recent research is the determination of the time constants of the TEM response, or equivalently the poles of the frequency domain signal, to identify the buried target (Snyder *et al.*, 1999; Baum, 1997; Collins *et al.*, 1999). A method that represents a hybrid of the model-based and data-based algorithm is under development at Blackhawk Geometrics (Grimm, 2000). In that approach, a spheroid modeller, working jointly with a model-based inversion algorithm, generates a library of model parameters which can then be operated upon by a neural network classifier for comparison with parameters derived from the raw sensor signal.

In this paper we present a model-based TEM data interpretation algorithm which estimates the basic shape (rod-like or plate-like) and magnetic character (ferrous or non-ferrous) of a buried metallic object. We first present an approximate forward model that represents the time domain response of a metallic object as a pair of perpendicular dipoles located at the center of the buried target. This form of model was suggested to us in a personal communication from J.D. McNeill. The strengths of these dipoles decay with time, and the parameters that govern the time decay behavior are related to the conductivity,

permeability, shape, and size of the buried target. The parameterization is simple, and thus convenient to use in data fitting procedures. We next describe an inversion scheme to recover the model parameters from TEM data. Since these parameters encapsulate information about the physical attributes of the target, we can attempt to use them to determine if the target is ferrous and if the geometry is rod-like (most likely a UXO) or plate-like (most likely a non-ordnance item). Empirical relationships are developed that link the model parameters to the physical parameters of the target and these relationships form the basis of our algorithm. We conclude with the application of the algorithm to a synthetic data set contaminated with noise, and field data sets taken over a buried UXO and buried metallic scrap.

3 Development of Approximate Forward Modelling

In order to invert measured TEM data for the physical parameters of the target, it is necessary to have a forward model to describe the TEM response for a buried metallic object. We can restrict our search for response solutions to axi-symmetric metallic targets, since this geometric subset adequately describes all UXO and the majority of buried metallic scrap encountered in a remediation survey. Unfortunately analytic expressions for the time domain response are restricted to a metallic sphere, and even an expression for a permeable and conducting non-spherical axi-symmetric body is not available. Numerical solutions of Maxwell's equations, under continual development, are promising (e.g. Haber, 2000; Carin, 2000; Hiptmair, 1998), however, the computational time requirements for obtaining a solution still make them impractical for use as part of a rigorous inversion procedure. Our approach, therefore, is to use an approximate forward modelling that can adequately reproduce the measured electromagnetic anomaly in a minimal amount of time. The validity of this reduced modelling still needs further testing but the empirical tests carried out here suggest that it can be useful in practice.

The development of the approximate forward modelling is presented in four steps. We begin with the response of a sphere, so that the magnetic polarization dyadic $\bar{\bar{\mathbf{M}}}$ is introduced. This dyadic is then altered so that it is applicable to an axi-symmetric body. This generates the "two-dipole" model mathematically. Next we introduce a parameterization for the time decays of each of the two dipoles and finally, we combine everything to generate our approximate forward modelling.

Response for a Spherical Body

Consider a permeable and conducting sphere of radius a illuminated by a uniform primary field $\mathbf{B}^P$ (Fig. 1(a)). At a time $t = 0$ the primary field is terminated, and eddy currents are induced in the sphere; they subsequently decay due to the finite conductivity of the sphere. The secondary field $\mathbf{B}^S$ generated by the decaying currents is dipolar:

$$\mathbf{B}^S(t) = \frac{\mu_o}{4\pi r^3}\,\mathbf{m}(t)\cdot\left(3\hat{\mathbf{r}}\hat{\mathbf{r}} - \bar{\bar{\mathbf{I}}}\right) \tag{1}$$

where $\mathbf{m}(t)$ is the dipole moment induced at the center of the sphere at time t, r is the distance between the observation point and the sphere center, $\hat{\mathbf{r}}$ is the unit vector pointing from the sphere center to the observation point P, and $\bar{\bar{\mathbf{I}}}$ is the identity dyadic. The dipole moment is

$$\mathbf{m}(t) = \frac{2\pi}{\mu_o}\,\mathbf{B^P}\,L^{\mathbf{B}}(t) \tag{2}$$

where

$$L^{\mathbf{B}}(t) = 6a^3\mu_r \sum_{s=1}^{\infty} \frac{e^{\frac{-q_s t}{\tau}}}{q_s + (\mu_r - 1)(\mu_r + 2)} \tag{3}$$

where $\tau = \sigma\mu a^2$, and $\mu_r = \mu/\mu_o$ is the relative permeability (Kaufmann and Keller, 1985). In general the magnetic permeability of highly permeable materials is a function of many parameters, including the

strength of the incident magnetic field, temperature, and magnetic history. However, calculated TEM responses assuming a constant permeability of $\mu_r = 150$ for steel and $\mu_r = 1$ for aluminum compared well with laboratory TEM measurements of steel and aluminum targets (Pasion, 1999). Therefore we feel that Eqs. (1) to (3) are suitable for the analysis that follows here. The values q_s are roots to the transcendental equation

$$\tan q_s = \frac{(\mu_r - 1)\, q_s}{q_s^2 + (\mu_r - 1)}. \tag{4}$$

Equations (1) to (4) reveal that the secondary **B**-field of a sphere in a uniform primary field is equivalent to the **B**-field of a single magnetic dipole located at the center of the sphere and oriented parallel to the primary field. For convenience we write the relationship between the induced dipole and the primary field as $\mathbf{m} = \bar{\bar{\mathbf{M}}} \cdot \mathbf{B^P}$, where $\bar{\bar{\mathbf{M}}}$ is the magnetic polarizability dyadic. For a sphere,

$$\bar{\bar{\mathbf{M}}} = \frac{2\pi}{\mu_o} L^{\mathbf{B}}(t)\, \bar{\bar{\mathbf{I}}} = \frac{2\pi}{\mu_o} \begin{bmatrix} L^{\mathbf{B}}(t) & 0 & 0 \\ 0 & L^{\mathbf{B}}(t) & 0 \\ 0 & 0 & L^{\mathbf{B}}(t) \end{bmatrix}. \tag{5}$$

Baum (1999) details the characteristics of the magnetic polarizability dyadic, and notes that the triple degeneracy of the magnetic polarizability dyadic reflects the symmetry of the sphere.

The sphere solution possesses several characteristics that we retain in the formulation of our approximate solution for an axi-symmetric target. Firstly, the secondary field due to the induced currents generated in a sphere, illuminated by a uniform, step-off primary field, is dipolar at all points outside the sphere. We will also represent the secondary field for more general shapes as a dipolar field (Eq. (1)). A dipolar field approximation is reasonable for any observation point far enough away from any localized current distribution (Jackson, 1975), and it has been reported that for observation points greater than 1 to 2 times the target length, a dipolar field assumption is adequate (Casey and Baertlein, 1999 or Grimm et al., 1997). Indeed, higher order multipoles induced in a target will decay at early times (Grimm et al., 1997).

Secondly, the induced dipole moment in the center of a sphere is given by the dyadic product $\bar{\bar{\mathbf{M}}} \cdot \mathbf{B}^P$. This form indicates that the induced dipole is proportional to the projection of the primary field along the direction of the induced dipole. The components of $\bar{\bar{\mathbf{M}}}$ scale the strengths of the dipoles. The magnetic polarizability dyadic, in the case of the sphere, contains the function $L^{\mathbf{B}}(t)$ that contains all the information about the time decay of the sphere and it depends upon the material properties, shape, and size of the target. Our hypothesis is that more general metallic shapes can also be approximately modelled with an induced dipole equal to the dyadic product $\bar{\bar{\mathbf{M}}} \cdot \mathbf{B}^P$. However, choosing the right functional form of $\bar{\bar{\mathbf{M}}}$ will be crucial.

Approximating the Magnetic Polarizability Dyadic for an Axi-Symmetric Body

Analytic expressions for $\bar{\bar{\mathbf{M}}}$ for the time domain response of a permeable and conducting non-spherical axi-symmetric body are not available. Therefore we base our form of $\bar{\bar{\mathbf{M}}}$ on the magnetostatic polarizability for a spheroid. Recall that for the time domain response of a sphere the structure of $\bar{\bar{\mathbf{M}}}$ is identical to the structure of the magnetostatic polarizability dyadic of a sphere. The analytic solution for the

magnetostatic response of a magnetic prolate spheroid is equivalent to the field of a magnetic dipole induced at the spheroid center (Das *et al.*, 1990):

$$\begin{aligned}\mathbf{m}^{spheroid} &= \mathbf{m}_1 + \mathbf{m}_2 \\ &= k_1\left[\left(\hat{\mathbf{z}}' \cdot \mathbf{B}^p\right)\hat{\mathbf{z}}'\right] + k_2\left[\left(\hat{\mathbf{y}}' \cdot \mathbf{B}^p\right)\hat{\mathbf{y}}' + \left(\hat{\mathbf{x}}' \cdot \mathbf{B}^p\right)\hat{\mathbf{x}}'\right] = \begin{bmatrix} k_2 & 0 & 0 \\ 0 & k_2 & 0 \\ 0 & 0 & k_1 \end{bmatrix} \cdot \mathbf{B}^p\end{aligned} \tag{6}$$

where k_1 and k_2 are the polarizability constants, which are functions of the conductivity, permeability, shape, and size. Equation (6) reveals that the total induced dipole can be written as the sum of two orthogonal dipoles $\mathbf{m}_1$ and $\mathbf{m}_2$. The first dipole moment $\mathbf{m}_1$ is parallel to the major axis ($\hat{\mathbf{z}}'$ in fig. 1(b)) of the spheroid, and its strength is proportional to the product of the primary field along that direction and the polarizability k_1. The second dipole moment is perpendicular to the major axis, and its magnitude is proportional to the component of the primary field along that direction and the polarizability k_2. A consequence of k_1 and k_2 being functions of the spheroid's shape and size is that the orientation of the effective dipole will not be solely determined by the direction of the primary field, as is the case for a sphere. In addition, the orientation of $\mathbf{m}^{spheroid}$ will be influenced by the aspect ratio of the spheroid.

The polarization dyadic in Eq. (6) suggests a magnetic polarization dyadic for the TEM problem of the form

$$\bar{\bar{\mathbf{M}}} = \begin{bmatrix} L_2(t) & 0 & 0 \\ 0 & L_2(t) & 0 \\ 0 & 0 & L_1(t) \end{bmatrix} \tag{7}$$

where we have simply replaced k_1 and k_2 in Eq. (6) with the dipole decay functions $L_1(t)$ and $L_2(t)$. The resultant induced dipole moment for this definition of the magnetic polarization dyadic is then

$$\begin{aligned}\mathbf{m}(t) &= \mathbf{m}_1(t) + \mathbf{m}_2(t) \\ &= L_1(t)\left[\left(\hat{\mathbf{z}}' \cdot \mathbf{B}^p\right)\hat{\mathbf{z}}'\right] + L_2(t)\left[\left(\hat{\mathbf{y}}' \cdot \mathbf{B}^p\right)\hat{\mathbf{y}}' + \left(\hat{\mathbf{x}}' \cdot \mathbf{B}^p\right)\hat{\mathbf{x}}'\right]\end{aligned} \tag{8}$$

Therefore, our approximate forward model represents the TEM response of two orthogonal dipoles. The first dipole is parallel to the symmetry axis of the target, and the second dipole is perpendicular to the symmetry axis. These dipoles decay independently according to the decay laws $L_1(t)$ and $L_2(t)$, respectively.

By choosing the appropriate parameters, this 'two-dipole' model produces TEM responses that are consistent with those observed field measurements of UXO. It has been noted that the shape anomaly of the measured response for UXO changes with time (Grimm et al., 1997). The physical phenomenon that gave rise to the temporal changes in shape anomaly was explained in terms of the nature of the induced eddy currents. Eddy currents that circulate end-to-end in the UXO dominate at early time but decay away quickly, while eddy currents that circulate about the long axis extend later into time. This observed field behavior can be duplicated by letting the two orthogonal dipoles $\mathbf{m}_1(t)$ and $\mathbf{m}_2(t)$ decay independently of each other. The dipole $\mathbf{m}_1(t)$ is parallel to the long axis and it simulates the magnetic fields that arise from currents circulating about the axis. The dipole $\mathbf{m}_2(t)$ is perpendicular to the long axis and it simulates the magnetic fields that arise from currents circulating end-to-end. By assigning a different decay characteristic (governed by its decay parameters) to each dipole, the relative contribution by each dipole to the secondary field can vary with time.

Time Decay Functions $L_1(t)$ and $L_2(t)$

The time decay for a sphere is determined by the sum of exponentials. This result generalizes to the case of a conductive body of arbitrary size and shape in an insulating medium illuminated by a step-off primary field (Kaufman, 1994). Thus the form for $L(t)$ should, at least, be able to duplicate the time decay features observed for the sphere. Plots of the **B**-field and $\partial \mathbf{B}/\partial t$ response for both a magnetically permeable (e.g. steel) and non-permeable (e.g. aluminum) sphere are shown in Fig. 2.

An appropriate form of the decay law for the **B**-field is

$$L(t) = k\,(t+\alpha)^{-\beta}\, e^{\frac{-t}{\gamma}}. \tag{9}$$

The parameter k controls the magnitude of the modelled response. The three parameters α, β, and γ, control the duration and characteristics of the three different stages of the time decay curve. The duration of the relatively flat early time stage is proportional to the parameter α. The linear decrease of response observed during the intermediate time stage is determined by $t^{-\beta}$. The exponential decay characterizing the late time stage is controlled by the parameter γ. Figure 2(a) demonstrates the ability to reproduce the secondary **B**-field. This form of the decay law, with the α parameter absent, was suggested to us in a personal communication from J.D. McNeill.

The time derivative $\partial \mathbf{B}/\partial t$, which is measured directly with most TEM receivers can also be modelled with Eq. (9). Figure 2(a) includes plots of the $\partial \mathbf{B}/\partial t$ curves for a steel and an aluminum sphere. The early time behaviour for the non-permeable sphere follows a $t^{-1/2}$ decay and so these curves are different from those of **B** in Fig. 2(b). Nevertheless the curves are still represented by early time turn-overs, and linear and exponential decays that can be accommodated by Eq. (9). The suitability is demonstrated by the fit between the laboratory measured response and a predicted response obtained by evaluating Eq. (9).

In the following section we generically denote the TEM response as $\boldsymbol{\xi}(\mathbf{r}, t)$ where $\boldsymbol{\xi}$ can be the magnetic field or its time derivative. The time dependent decay of $\boldsymbol{\xi}$ is given by Eq. (9).

The Approximate Forward Model

With the above background, we can write an approximate expression for the secondary field response of an axi-symmetric target. First, let us switch from the body-fixed (primed) coordinate system to a space-fixed coordinate system, which is more amenable to the definitions of target and sensor location of a typical field survey (Fig. 3). A vector $\mathbf{v}'$ in the body-fixed system co-ordinate system is related to a vector $\mathbf{v}$ in the space-fixed co-ordinate system via the Euler rotation tensor $\mathbf{A}(\psi, \theta, \phi)$ by (Arfken, 1985)

$$\mathbf{v}' = \mathbf{A}\,\mathbf{v}. \tag{10}$$

Due to the axial symmetry of the problem $\psi = 0$, and the Euler rotation tensor can be written

$$\mathbf{A} = \begin{bmatrix} \cos\theta\cos\phi & \cos\theta\sin\phi & -\sin\theta \\ -\sin\phi & \cos\phi & 0 \\ \sin\theta\cos\phi & \sin\theta\sin\phi & \cos\theta \end{bmatrix}, \tag{11}$$

where θ is the angle between the symmetry axis of the target ($\hat{\mathbf{z}}'$ in Fig. 1(b)) and the vertical axis in the space-fixed coordinate system ($\hat{\mathbf{z}}$ in Fig. 3), and ϕ is the angle between the projection of $\hat{\mathbf{z}}'$ onto the horizontal plane and $\hat{\mathbf{x}}$.

The approximate forward modelling is written by substituting the definition of the induced dipole of Eq. (8) into the expression for a dipole field (1), and carrying out the dyadic product. Let us consider a target whose center is located at $\mathbf{R}$ in the space-fixed co-ordinate system. The secondary response $\boldsymbol{\xi}(\mathbf{r}, t)$ measured at a receiver/transmitter location $\mathbf{r}$ and at a time t after the termination of the primary field, is then the sum of the responses of the two orthogonal dipoles:

$$\boldsymbol{\xi}(\mathbf{r}, t) = \boldsymbol{\xi}_1(\mathbf{r}, t) + \boldsymbol{\xi}_2(\mathbf{r}, t) \tag{12}$$

where

$$\boldsymbol{\xi}_i(\mathbf{r}, t) = \frac{\mu_o}{4\pi}\left(3\left[\mathbf{m}_i(t)\cdot(\mathbf{r}-\mathbf{R})\right]\frac{(\mathbf{r}-\mathbf{R})}{|\mathbf{r}-\mathbf{R}|^5} - \frac{\mathbf{m}_i(t)}{|\mathbf{r}-\mathbf{R}|^3}\right) \tag{13}$$

and

$$\mathbf{m}_1(t) = L_1(t)\left(\hat{\mathbf{z}}'\cdot\mathbf{B}^p\right)\hat{\mathbf{z}}' \tag{14}$$

$$\mathbf{m}_2(t) = L_2(t)\left[\left(\hat{\mathbf{x}}'\cdot\mathbf{B}^{\mathbf{P}}\right)\hat{\mathbf{x}}' + \left(\hat{\mathbf{y}}'\cdot\mathbf{B}^{\mathbf{P}}\right)\hat{\mathbf{y}}'\right] \tag{15}$$

are the dipole parallel and perpendicular to the axis of symmetry. The unit vectors are given by Eq. (11).

In summary, the approximate response of a buried metallic object given by Eq. (12) can be generated from 13 parameters that describe the object. These model parameters are elements of the model vector

$$\mathsf{m} = [X,\, Y,\, Z,\, \phi,\, \theta,\, k_1,\, \alpha_1,\, \beta_1,\, \gamma_1, k_2,\, \alpha_2,\, \beta_2,\, \gamma_2]\,. \tag{16}$$

X and Y denote the surface projection of the centroid of the body, and Z is the depth of the object below the surface. The orientation of the target is described by the two angles θ and ϕ. The remaining parameters describe the decay characteristics of the two dipoles: k_1, α_1, β_1, and γ_1 describe the dipole parallel to the axis of symmetry ($\mathbf{m}_1$), and k_2, α_2, β_2, and γ_2 describe the dipole perpendicular to the axis of symmetry ($\mathbf{m}_2$). Thus the inversion for the model m will immediately give estimates of target location and orientation. Information on the shape, size, and material parameters of the target may later be inferred from the remaining parameters.

4 Non-Linear Parameter Estimation Procedure

In this paper it is first assumed that the response measured in a survey is due to a single body, and second, that the response of this single body can be accurately modelled with Eq. (12). With these hypotheses, an inversion procedure is developed that utilizes the approximate forward model.

The forward model can be expressed as

$$d_j = F_j[\mathsf{m}], \qquad j = 1, 2, 3, ...N \tag{17}$$

This equation expresses the mapping of the model vector m to a datum d_j by a functional F_j. The forward mapping F_j is defined by Eq. (12) and is a nonlinear functional of the 13 model parameters given in Eq. (16). In the inverse problem, these parameters are retrieved from a vector of observed data d^{obs} by minimizing a least-squares objective function. Before proceeding to the details of the inversion there are two important practical aspects to be introduced: (1) Selected parameters must remain positive and (2) Parameters should be scaled to enhance stability in the iterative process.

In the approximate forward model the time decay parameters k_i, α_i, β_i, and γ_i $(i = 1, 2)$ are defined as positive. In the inverse problem the positivity of these parameters can be maintained by solving the associated square-variable unconstrained problem (Gill et al., 1981). Following this formulation, each time decay parameter m_i is replaced by the squared variable w_i such that $m_i = w_i^2$. A second transformation is a linear scaling that ensures that each component of m is of order unity. This is done by dividing each parameter m_i by its typical value. In the following presentation of the inversion algorithm, the letter m continues to denote the parameter vector to be inverted for, but now includes the positivity and scaling transformations.

Defining the Objective Function

If there are L time channels and K locations where TEM data are collected, then there will be $N = KL$ data points contained in the data vector d^{obs}. Because data will be collected on several lines, with a number of stations per line, there will generally be far more data than model parameters ($N >> 13$). Therefore the inversion for m involves solving an overdetermined system of non-linear equations, with the goal of finding the model that produces the data that best fit the observed data. This is a non-linear least squares problem and is solved by minimizing

$$\Phi(\mathsf{m}) = \frac{1}{2}\|\mathsf{W}_d\left(F[\mathsf{m}] - \mathsf{d}^{obs}\right)\|^2 \tag{18}$$

where $F[\mathsf{m}]$ are the forward modelled data, d^{obs} are the observed data, and Φ is the least squares objective function that measures how closely our predicted data match the observed data. W_d is the data weighting matrix. If the data are contaminated with unbiased Gaussian random noise, then W_d is ideally a diagonal matrix whose elements are the reciprocals of the standard deviation of each datum. The noise arises from many sources, including sensor location errors, instrument noise, and inaccuracy of the forward modelling. It is likely that the Gaussian independent assumption is not valid, but it is essential to

estimate a quantity that reflects the uncertainty in each datum. We assume that the errors can be characterized by a percentage of the datum value plus a threshold, that is

$$(\mathsf{W}_d)_{ii} = \frac{1}{\rho d_i + \epsilon} \tag{19}$$

where ρ is typically a percentage and ϵ is a constant that characterizes ambient noise. The positive ϵ ensures that small data points would have reasonable errors assigned to them, and thus prevents them from having undue influence on the solution.

Minimizing the Objective Function

For ease of notation the least squares problem is rewritten as

$$\text{minimize} \quad \Phi(\mathsf{m}) = \frac{1}{2}\mathsf{r}(\mathsf{m})^T \mathsf{r}(\mathsf{m}) = \frac{1}{2}\sum_{i=1}^{N} r_i(\mathsf{m})^2 \tag{20}$$

where r is the residual function

$$\mathsf{r}(\mathsf{m}) = \mathsf{W}_d\left(F[\mathsf{m}] - \mathsf{d}^{obs}\right)$$

and $r_i(\mathsf{m})$ is the i^{th} component of $\mathsf{r}(\mathsf{m})$. We adopt a modified Newton's method to minimize the objective function. The approach taken here is to first make an initial guess of the model parameters m_o. Techniques for making this initial guess are outlined in Pasion (1999). The starting model m_o is iteratively improved to find the minimum of Eq. (20). At each iteration a Newton's search direction is chosen that minimizes the local quadratic model about the current iterate m_k. The Newton step $\delta\mathbf{m}$ for the non-linear least squares problem is then given by

$$\mathsf{H}(\mathsf{m}_k)\,\delta\mathbf{m} = -\mathsf{J}(\mathsf{m}_k)^T \mathsf{r}(\mathsf{m}_k) \tag{21}$$

where the Jacobian matrix J and the Hessian matrix H are defined as

$$\mathsf{J}_{ij}(\mathsf{m}) = \frac{\partial r_i}{\partial \mathsf{m}_j} \qquad \text{and} \qquad \mathsf{H} = \mathsf{J}(\mathsf{m})^T \mathsf{J}(\mathsf{m}) + \mathsf{S}(\mathsf{m}),$$

where $\mathsf{S}(\mathsf{m})$ is

$$\mathsf{S}(\mathsf{m}) = \sum_{i=1}^{N} r_i(\mathsf{m})\,\nabla^2 r_i(\mathsf{m})$$

A new model $\mathsf{m}_{k+1} = \mathsf{m}_k + \lambda\delta\mathbf{m}$ is then defined, where the positive scalar λ is chosen such that $\Phi(\mathsf{m}_k + \lambda\delta\mathbf{m}) < \Phi(\mathsf{m}_k)$. The sequence of iterations is terminated once the relative gradient measure is less than a tolerance level , or once there is insignificant change in the models obtained at successive iterations (Dennis and Schnabel, 1983).

Error Bounds of the Parameter Estimates

Once the model parameters m_* which minimize the objective function $\Phi(\mathsf{m})$ have been obtained, we can examine the reliability and precision of the estimated parameters via the model covariance matrix. Let

m_+ be the best estimate of the model in the absence of noise, and $\delta\mathsf{m}_* = \mathsf{m}_+ - \mathsf{m}_*$. The model covariance matrix V_m is defined as the expectation value of $\delta\mathsf{m}_*\ \delta\mathsf{m}_*{}^T$(Bard, 1974)

$$\mathsf{V}_m \equiv E\left(\delta\mathsf{m}_*\ \delta\mathsf{m}_*{}^T\right) \approx E\left(\mathsf{H}_*{}^{-1}\,\mathsf{J}_*{}^T\ \delta\mathsf{d}^{obs}\ \delta\mathsf{d}^{obs\,T}\,\mathsf{J}_*\mathsf{H}_*{}^{-1}\right)$$

The Hessian and Jacobian in the above expression are evaluated at $\mathsf{m} = \mathsf{m}*$, and are therefore constants. As a result they can be taken outside of the expectation value expression:

$$\mathsf{V}_m = \mathsf{H}_*{}^{-1}\,\mathsf{J}_*{}^T\,\mathsf{V}_d\,\mathsf{J}_*\mathsf{H}_*{}^{-1} \tag{22}$$

where V_d is the covariance matrix of the data. In the case when the observations have uncorrelated errors, the data covariance matrix reduces to a diagonal matrix, and an estimate of the standard deviation of the i^{th} model parameter m_i is then

$$\sigma_i^{\mathsf{m}} = (\mathsf{V}_m)_{ii} = \sigma^2\left(\mathsf{H}_*{}^{-1}\,\mathsf{J}_*{}^T\mathsf{J}_*\mathsf{H}_*{}^{-1}\right)_{ii} \tag{23}$$

Model variance estimates applied to non-linear problems are not as reliable as when implemented in linear least squares problems, and they should only be used as a very rough estimate (Bard, 1974; Dennis and Schnabel, 1983). Nevertheless, Eq. (23) at least provides a minimum estimate to the uncertainties of the parameters.

5 Relating Model Parameters to Material and Geometric Properties

The above inversion generates the parameters that characterize a target's TEM anomaly. The next step is to interpret these parameters. Recall that UXO are typically rod-like rather than plate-like, and are magnetically permeable. In order to extract these potentially UXO identifying features from the recovered model m^*, we use the inversion procedure to fit a series of decay curves from a range of axi-symmetric targets of different shape, geometry, and material properties. We then generate empirical relationships between the parameters and target characteristics. The data curves used for this analysis were either TEM measurements made in the Geonics Ltd. laboratory, or they were synthetically generated decay curves for a sphere using Eq. (12).

Lab Setup and Measurements

A series of TEM measurements of metallic targets was made by Geonics Ltd. A 40 m $\times$ 40 m square transmitter loop was used to provide a relatively uniform field at the center of the loop. A 1 m diameter receiver coil was placed coaxial and coplanar to the transmitter loop, and each target was located at the center of the receiver loop. The Geonics PROTEM 47 time domain equipment was used for producing the transmitting field and for recording the time domain measurement due to a step-off current. Measurements of the time decay response of these targets were recorded as plots of $\log(\partial \mathbf{B}/\partial t)$ vs. $\log(t)$. Since values were not recorded by a data logger, the plots were subsequently digitized. Plots of the steel target responses were digitized by hand by J.D. McNeill at Geonics Ltd., and the aluminum target responses were digitized at UBC after scanning the plots into a computer. Analyses were performed on both the impulse $(\partial \mathbf{B}/\partial t)$ response measured as an induced voltage in the receiver, and also on the $\mathbf{B}$-field response. The $\mathbf{B}$-field response was obtained by integrating the induced voltage.

Two sets of targets were measured. The first set of measurements involved recording the TEM response for a series of steel and aluminum rectangular prisms of different dimensions. Each prism had at least one dimension of 20.3 cm, and the targets ranged from a thin rod (20.3 $\times$ 0.6 $\times$ 0.6 cm) to a cube (20.3 $\times$ 20.3 $\times$ 20.3 cm) to a thin plate (20.3 $\times$ 20.3 $\times$ 0.6 cm). A second set of measurements was made on 24 sample UXO. These targets included various ordnance items used by NATO since World War II. The ordnance range in length from 18 to 85 cm, and in diameter from 6.1 to 15.9 cm. A diagram of all the ordnance, along with a table listing the dimensions of each ordnance, is included in Pasion (1999).

The axi-symmetric targets were placed in two orientations at the center of the receiver loop in two orientations. Each target was measured with the axis of symmetry perpendicular and parallel to the primary field. Since the strength of each induced dipole is proportional to the projection of the primary field onto the dipole direction, the two measurement orientations isolate the decay behaviour of each of the two dipoles. For example, consider a plate. When the primary field is perpendicular to the plane of the plate, the projection of the primary field onto dipole 2 is zero, thus the approximate forward model assumes the response can be modelled as a single dipole perpendicular to the plate. The decay

parameters of dipole 1 (k_1, α_1, β_1, and γ_1) can then be estimated by fitting this curve to the decay law (Eq. (9)). When the primary field is parallel to the plane of the plate, the response is due to dipole 2 and parameters k_2, α_2, β_2, and γ_2 can be recovered.

Relationships between the target characteristics and the model parameters were established in the following manner. A scaled-down version of the non-linear least squares techniques outlined in the previous section was used to obtain the decay parameters k, α, β, and γ for each of the target's two dipoles. Secondly, we observed how recovered values of model parameters, or combinations of parameters, changed with the dimensions and magnetic properties of the measured prism. The patterns in the behaviour of the parameters then led to the shape and permeability discrimination diagnostics that are proposed in the following sections.

A Relationship Between β and Magnetic Permeability

UXO are generally made of steel, which is a ferrous material. Therefore, the magnetic permeability is likely to be an identifying characteristic of UXO. To generate a link between magnetic permeability and model parameters, forward modelled responses were calculated for a series of spheres varying in size and permeability. Both **B**-field and $\partial\mathbf{B}/\partial t$ data were then inverted to generate decay parameters, and in particular, to produce estimates of the parameter β. The plots of β as a function of sphere radii and magnetic permeability, are provided in Fig. 4.

Figure 4 suggests that the value of β obtained for a sphere may be diagnostic in determining whether the sphere is permeable or non-permeable. Figure 4(a) exhibits the relationship for the $\partial\mathbf{B}/\partial t$ responses. For a sphere with $\mu_r = 150$ (typical for steel), we see, for spheres with radii between 5 to 15 cm, that β falls between 1.11 and 1.35; while for a sphere with $\mu_r = 1$, β has a value of approximately 0.5, which corresponds to the early time $t^{-1/2}$ behavior that Kaufman (1994) predicted for a non-permeable sphere. Therefore, when applying our inversion to the time derivative of the field, a value of $\beta^{\partial\mathbf{B}/\partial t}$ greater than about 0.8 indicates that the target is most likely permeable. This analysis is repeated on the forward modelled **B**-field responses, and the results are plotted in Fig. 4(b). A threshold value of $\beta^{\mathbf{B}} = 0.3$ could be used such that targets with a **B**-field response characterized by a $\beta > 0.3$ indicates a permeable target.

The use of β as a diagnostic to determine permeability can be extended to non-spherical targets by looking at the recovered β values for the aluminum and steel prisms. The inversion produces two values of β, one for each of the excited dipoles, to describe a buried target. We suggest taking the average of the two recovered β values, which we label as $\bar{\beta}$. When analyzing the $\partial\mathbf{B}/\partial t$ responses of the axi-symmetric aluminum targets, $\bar{\beta}^{\partial\mathbf{B}/\partial t} = 0.52$ with a standard deviation of 0.07. For the steel targets $\bar{\beta}^{\partial\mathbf{B}/\partial t} = 1.11$ with a standard deviation of 0.08. These averages fall on either side of the 0.8 threshold obtained by fitting sphere $\partial\mathbf{B}/\partial t$ responses.

When analyzing the **B**-field responses of the axi-symmetric aluminum targets, $\bar{\beta}^{\mathbf{B}} = 0.17$ with a standard deviation of 0.03. For the steel targets $\bar{\beta}^{\mathbf{B}} = 0.5$ with a standard deviation of 0.2. These averages fall on either side of the 0.3 threshold obtained by fitting sphere **B**-field responses, and so again, a consistent criterion can be used.

Relationships Between Model Parameter Ratios and Target Shape

Empirical relationships were also established between the target shape and the ratios k_1/k_2 and β_1/β_2. For space reasons, we present only the analysis of the $\partial\mathbf{B}/\partial t$ response of the targets, and refer the reader to Pasion (1999) for the analysis of the **B**-field data. There we show that the same target shape diagnostics, developed here for $\partial\mathbf{B}/\partial t$ data, also apply to **B**-field data.

The Ratio k_1/k_2

The recovered k values for targets ranging from a steel plate to a steel rod are shown in Fig. 5(a), and the calculated k-ratios are shown in Fig. 5(b). For a steel plate, the k-ratio $k_1/k_2 < 1$. For a steel bar the k-ratio $k_1/k_2 > 1$. The recovered k values for aluminum targets are shown in Fig. 5(c). The opposite orientation effect was observed for an aluminum rod, that is $k_1/k_2 < 1$ (Fig. 5(d)).

The Ratio β_1/β_2

In addition to the relative strength of the dipoles being shape dependent, the slope of the time decay response (either $\partial\mathbf{B}/\partial t$ or **B**-field) during the intermediate time stage is dependent upon the target shape. This effect was seen in steel targets only. The steepness of the response during the intermediate time stage is reflected in the parameter β. The recovered β values for targets ranging from a steel plate to a steel rod are shown in Fig. 6(a), and β values for aluminum targets are shown in Fig. 6(c). A dipole that decays at a greater rate will have a larger β. The rate of decay of the $\partial\mathbf{B}/\partial t$ response is greater when the plane of a steel plate is perpendicular to the primary field (dipole 1), than when the plane of a steel plate is parallel to the primary field (dipole 2). Thus, for a steel plate the β-ratio $\beta_1/\beta_2 > 1$. In the case of a rod, the $\partial\mathbf{B}/\partial t$ response decays faster (and thus β is larger) when the main axis of the rod is perpendicular to the primary field (dipole 2). In the case of a steel rod the β-ratio $\beta_1/\beta_2 < 1$ (Fig. 6(b)).

For aluminum targets the response shape looks essentially the same for each of the targets. The $\partial\mathbf{B}/\partial t$ response exhibits a power law decay of $t^{-1/2}$ and is exponential at later times. The decay curves for aluminum targets are essentially the same regardless of target shape, and therefore there is no relationship between the β-ratio and the aspect ratio (Fig. 6(d)).

The Discrimination Algorithm Using $\partial\mathbf{B}/\partial t$ Data

The results from the previous section suggest the following algorithm for using $\partial\mathbf{B}/\partial t$ data to help identify possible UXO targets:

1. Perform the non-linear inversion outlined in the previous section to recover model parameters for the two-dipole model.
2. Compute $\bar{\beta} = \frac{1}{2}(\beta_1 + \beta_2)$. If $\bar{\beta} > 0.80$ then the target is most likely permeable.
3. Compute ratios β_1/β_2 and k_1/k_2. There are two options:
   - $\bar{\beta} > 0.8 \Rightarrow$ *Ferrous Target*: If $k_1/k_2 > 1$ and $\beta_1/\beta_2 < 1$ then a permeable *rod-like* target was measured. If $k_1/k_2 < 1$ and $\beta_1/\beta_2 > 1$ then a permeable *plate-like* target was measured.

- $\bar{\beta} < 0.8 \Rightarrow$ *Non-Ferrous Target*: If $k_1/k_2 > 1$ then non-permeable *plate-like* target was measured. If $k_1/k_2 < 1$ then the target is *rod-like*. β_1/β_2 does not give supporting, or extra, information.

The above algorithm can be extended to the analysis of **B**-field data simply by changing the β threshold to 0.3.

The parameters α and γ, which respectively are representative of a target's early and late time characteristics, are not used in the discrimination algorithm. The α parameter is very sensitive to how early the measurement of the TEM sensor extends in time and we have found that it is not as robustly estimated as k, β, and γ. The late time constant for conductors is related to a target's shape, size and conductivity (Kaufman, 1994 and Nabighian and Macnae, 1991). However, as noted by Nabighian and Macnae (1991), using the time constant for discrimination is difficult without prior knowledge of the shape and either a length scale or conductivity. Our tests thus far have been unable to generate a consistent relationship between the time constant recovered from lab TEM measurements and target characteristics.

6 Synthetic Data Set

The parameter estimation procedure is now tested on a synthetically generated field data set. The object of interest is a 75 mm anti-tank mortar. The primary decay curves for the axial and perpendicular orientations were obtained from measurements made by Geonics using the setup described in the previous section. These were inverted to recover the decay parameters for each dipole. For this simulation, the target is assumed to be buried at a depth of 57 cm (Z=1 m), and located at (2m N,2m E) on the survey grid. The mortar is oriented such that $\phi = 30\,^\circ$ and $\theta = 65\,^\circ$. Equation (12) was used to generate the "observed" data for this example.

The survey consists of a 2 m $\times$ 2 m grid, containing 5 lines of data separated at 50 cm line spacing, with stations located at 20 cm intervals along each line. At each station the vertical component of the voltage is generated for 26 logarithmically spaced time channels. The time channels range from 0.01 ms to 100 ms. In order to make this example closer to a real TEM data set, 5% random Gaussian noise was added to the data and, since a real TEM instrument will have a finite measurement sensitivity to the secondary field, a data threshold of 0.001 is set. There are 1278 total data points exceeding the minimum threshold.

The inversion is carried out with a data weighting matrix in Eq. (19) with $\rho = 0.05$ and $\epsilon = 0.001$ mV. The observed data, and data predicted by the recovered model, are compared in Figs. 7 and 8. Figure 8 shows a plan view comparison for three of the 26 time channels. The difference maps exhibit a random distribution over the data, indicating the reluctance of the inversion to fit the noisy portion of the data. A comparison of the true model m_{true}, recovered model m_{rec} and the estimated model standard deviations σ^m are found in Table 1. The discrimination algorithm, when applied to the recovered decay parameters, yields the following. The value of $\bar{\beta} = 1.07(> 0.8)$ indicates that the target is likely permeable. The ratios $k_1/k_2 = 3.71(> 1)$ and $\beta_1/\beta_2 = 0.71(< 1)$ indicate, for a magnetically permeable target, that the TEM response is likely from a rod-like target.

7 Field Data Set

We now apply our algorithm to a TEM field data set acquired at the ERDC UXO test site in Vicksburg, Mississippi. The Geonics EM63 instrument used for the survey is a multi-time channel time domain unit consisting of a 1 m $\times$ 1 m square transmitter coil and a coaxial horizontal circular receiver loop mounted on a two-wheel trailer. Measured voltages are averaged over 26 geometrically spaced time gates, spanning the range 0.18 ms to 25.14 ms.

A 105 mm projectile is placed in the ground with its center at 2.0 m East, 1.83 m North and at a depth of 0.44 m from the surface. The projectile was placed horizontal ($\theta = 90\,°$), with its tip pointing to the North ($\phi = 0\,°$). Once the target was placed in the ground, it was not covered in soil. The survey consisted of a 2 m $\times$ 2 m grid centered on the target, containing 5 lines running North-South separated at 50 cm line spacing, with stations located at 5 cm intervals along each line. A measured signal of less than 1 mV is assumed to be indistinguishable from the noise. The resulting data set contains 1882 total data points.

The inversion is carried out with a data weighting matrix in Eq. (19) with $\rho = 0.05$ and $\epsilon = 1$ mV. The first stage of the time decay evident in Fig. 2 is not observed in the time window recorded by the EM63. Therefore, we invert these data by setting α to be a small constant that does not affect the predicted data within the EM63 time range. So only parameters k, β, and γ for each dipole are recovered. The observed and predicted data are compared in Figs. 9 and 10. Figure 10 shows a plan view comparison for five of the 26 time channels. At early times the anomaly has a single peak located approximately above the UXO center. This peak splits into two distinct peaks at late time. The recovered model predicts data that reflects this behavior. Figure 9 compares the decay curve measured at four stations on the survey.

The recovered location and orientation parameters are listed in Table 2(a). The recovered easting of 2.04 m differs from the true value of 2.00 m by 4 cm. The recovered northing of 1.77 m differs from the true value of 1.83 cm by 6 cm, placing the inducing dipole closer to the projectile tail. These errors are of the same magnitude as can be expected in spotting the station location in the field survey. In addition, the buried 105 mm projectile has a copper rotating band near the tail of the projectile. It has been suggested that the presence of the rotating band will shift the location of the induced dipole from the target center towards the tail (Miller, 2000). The recovered burial depth of 0.47 m is 3 cm deeper than the expected depths of 0.44 m. The orientation parameters θ and ϕ are well recovered. The recovered decay parameters are listed in Table 2(b) and the diagnostics applied to these parameters are listed in Table 2(c). The value of $\bar{\beta} = 0.91(> 0.8)$ indicates that the target is likely to be magnetically permeable. The ratios $k_1/k_2 = 2.63(> 1)$ and $\beta_1/\beta_2 = 0.69(< 1)$ indicate, for a magnetically permeable target, that the TEM response is likely to be from a rod-like target.

8 Discussion and Conclusion

Efficient remediation of areas containing UXO first requires that purely conductive metal targets be distinguished from steel targets that are conductive and permeable. The second stage then focuses upon determining if the steel target is rod-like (and likely to be a UXO) or plate-like (and not be of interest). To attack this problem we propose a modified parametric model from which TEM responses can be estimated. The TEM response of a buried axisymmetric metallic object is modelled as the sum of two dipoles located at the midpoint of the body. Non-linear inversion methods are used to extract the parameters from the field data and these parameters are subsequently used in a discrimination procedure which has two parts. First, the decision about whether the object is ferrous might be made by examining the size of the recovered β values. Second, if the object is considered to be ferrous, then the ratios of k_1/k_2 and β_1/β_2 are diagnostic indicators of whether the geometry is plate-like or rod-like. These diagnostics were developed for both **B**-field and $\partial\mathbf{B}/\partial t$ TEM data.

This algorithm was applied to a synthetic data set as well as to a field data set collected by the Geonics EM63 time domain electromagnetic sensor over a 105 mm projectile. In both cases the diagnostics, applied to the recovered model parameters, correctly predicted that the TEM anomaly was produced by a magnetically permeable and rod-like metallic target. Although further testing will be required to fully evaluate our proposed technique, the results presented here are promising and may have a positive impact on the interpretation of UXO detection data.

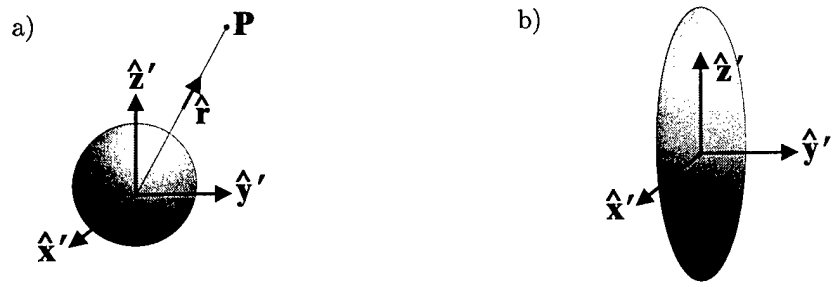

Figure 1: The body-fixed (primed) coordinate system for a sphere and a spheroid.

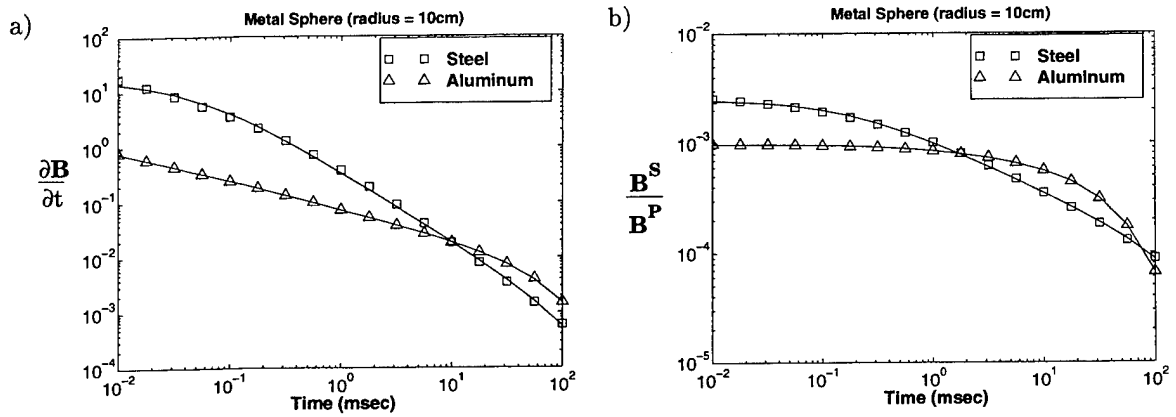

Figure 2: (a) The time decay behaviour of the time derivative of the magnetic field $\partial \mathbf{B}/\partial t$. (b) The time decay behaviour of the magnetic flux density $\mathbf{B}$. The $\mathbf{B}$-field response is normalized by the strength of the primary field. The solid lines are responses evaluated from eq. (9). The agreement supports the validity of this parametric representation of the time domain responses.

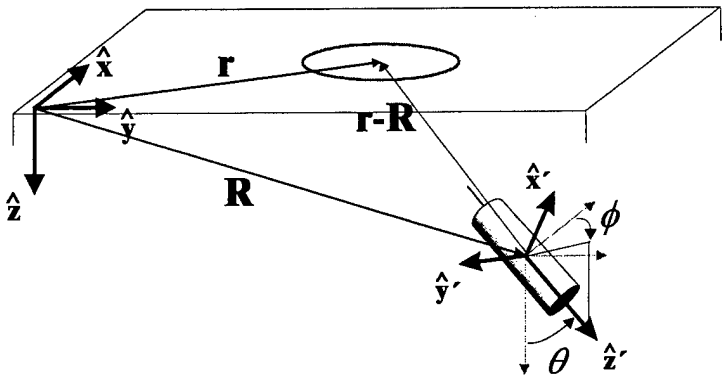

Figure 3: The field (unprimed) co-ordinate system for a buried target. The unit vectors $\hat{\mathbf{x}}$, $\hat{\mathbf{y}}$, and $\hat{\mathbf{z}}$ define the field co-ordinate system, and $\hat{\mathbf{x}}'$, $\hat{\mathbf{y}}'$, and $\hat{\mathbf{z}}'$ define the body-fixed co-ordinate system.

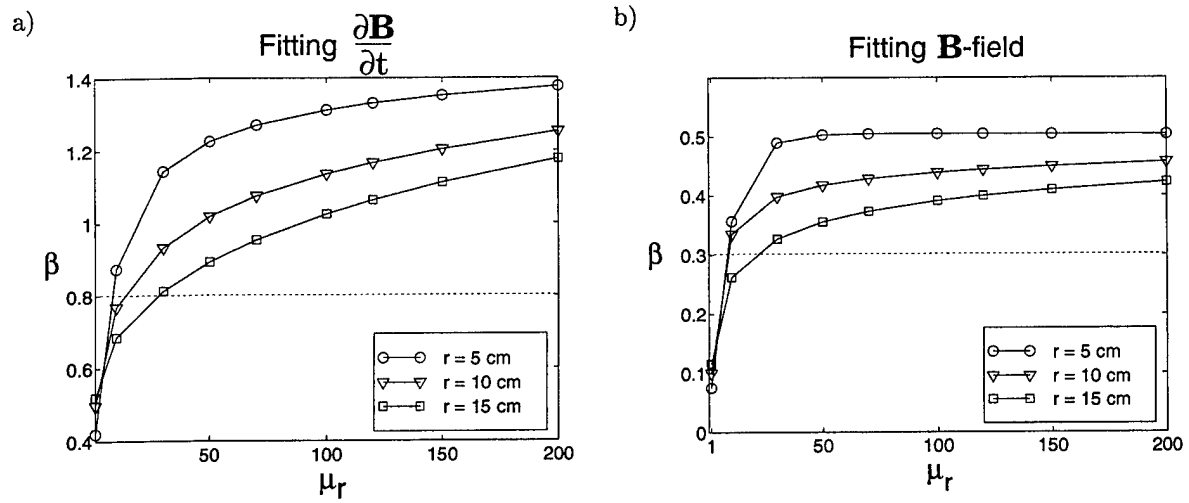

Figure 4: The behaviour of parameter β for various size spheres with varying permeability μ. Panel (a) contains results of recovering β by fitting the $\partial\mathbf{B}/\partial t$ data. Panel (b) contains results of recovering β by fitting the $\mathbf{B}$-field.

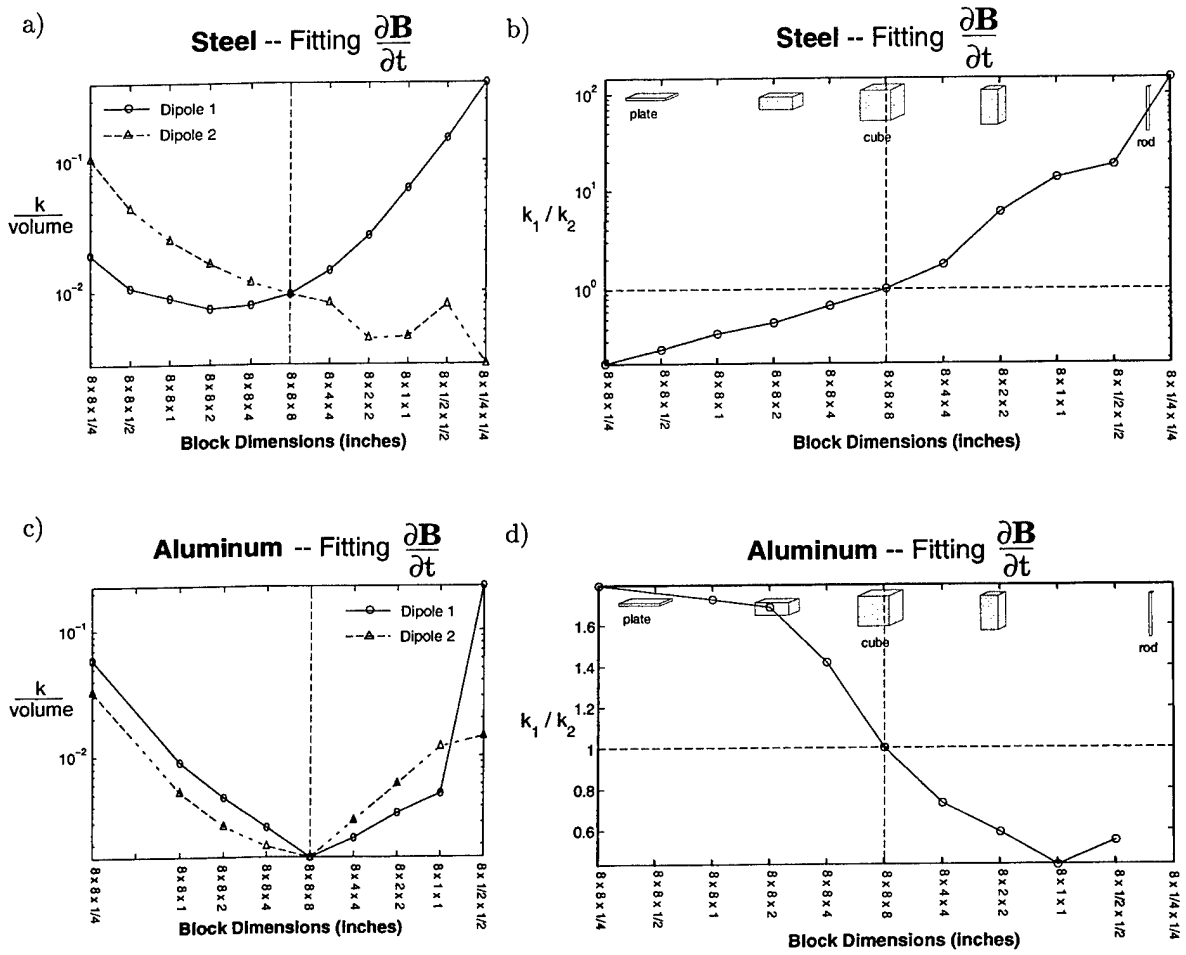

Figure 5: Relating the aspect ratio of a steel target with the ratio k_1/k_2. Plot (a) contains the recovered k parameter from fitting the measured $\partial \mathbf{B}/\partial t$ response of steel axi-symmetric targets. Plot (b) illustrates the relationship between the k_1/k_2 ratio derived from $\partial \mathbf{B}/\partial t$ data and the shape of a steel target. Plot (c) contains the recovered k parameter from fitting the measured $\partial \mathbf{B}/\partial t$ response of aluminum axi-symmetric targets. Plot (d) illustrates the relationship between the k_1/k_2 ratio and the shape of an aluminum target.

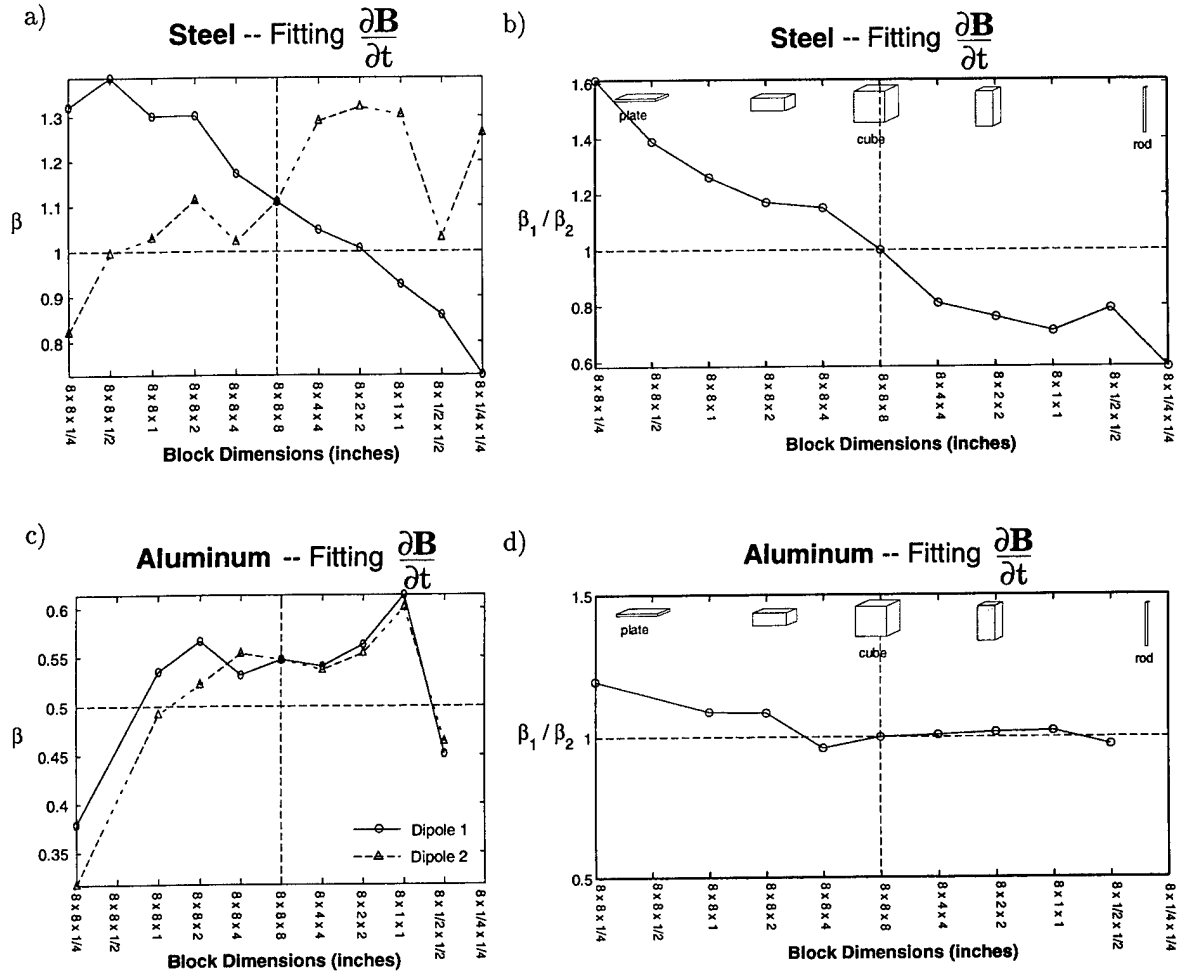

Figure 6: Relating the aspect ratio of a steel target with the ratio β_1/β_2. Plot (a) contains the recovered β parameter from fitting the measured $\partial\mathbf{B}/\partial t$ response of steel axi-symmetric targets. Plot (b) illustrates the relationship between the β_1/β_2 ratio derived from $\partial\mathbf{B}/\partial t$ data and the shape of a steel target. Plot (c) contains the recovered β parameter from fitting the measured $\partial\mathbf{B}/\partial t$ response of aluminum axi-symmetric targets. Plot (d) illustrates the relationship between the β_1/β_2 ratio and the shape of an aluminum target.

(a) Location and Orientation

m_i	m_o	m_{true}	m_{rec}	σ^{m}
Northing (m)	1.90	2.00	2.00060	0.00254
Easting (m)	2.15	2.00	2.00105	0.00169
Depth from loop (m)	1.20	1.00	1.00051	0.00764
ϕ (degrees)	45	30	30.07	0.18
θ (degrees)	45	65	65.04	0.11

(b) Decay Parameters

m_i	m_o	m_{true}	m_{rec}	σ^{m}
k_1	7.07	12.02	12.064	0.18
α_1	0.01	0.0076	0.00759	0.0030
β_1	1.00	0.89	0.890	0.0070
γ_1	3.16	17.65	17.635	0.16
k_2	7.07	3.30	3.252	0.071
α_2	0.01	0.0077	0.0076	0.0027
β_2	1.00	1.25	1.252	0.014
γ_2	3.16	11.54	11.68	0.33

Table 1: Recovered parameters from the inversion of the synthetic data set. m_o is the starting model. The true model m_{true} and the recovered model m_{rec} are close. The difference between the true and recovered model falls within the estimated standard deviation.

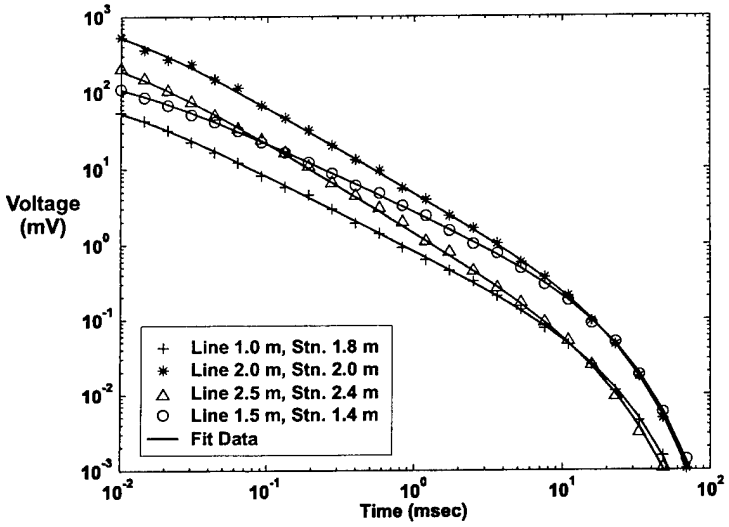

Figure 7: The observed and predicted decay curves for four stations in the synthetic data set inversion. The predicted vertical component of the response, represented by the solid lines, are a good match to the artificially generated noisy data set.

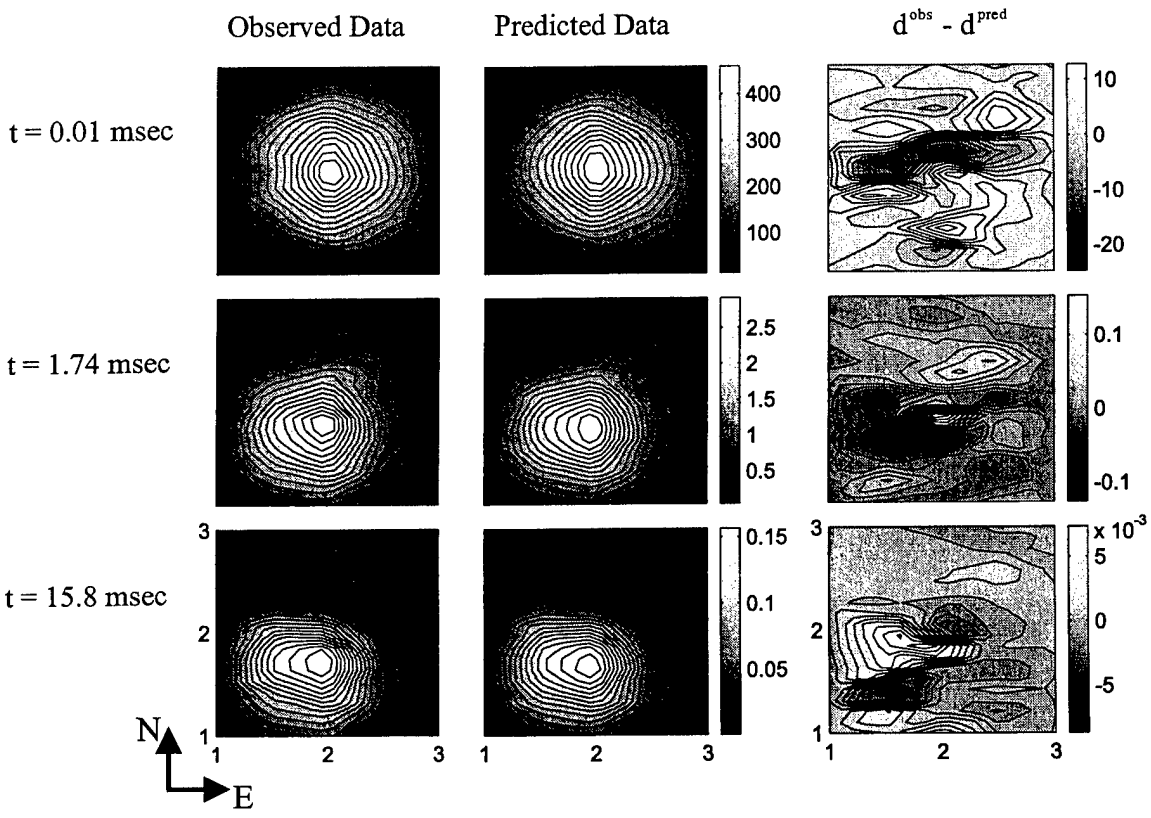

Figure 8: Plan view plots of the observed and predicted data for 3 of the 26 time channels in the synthetic data set inversion.

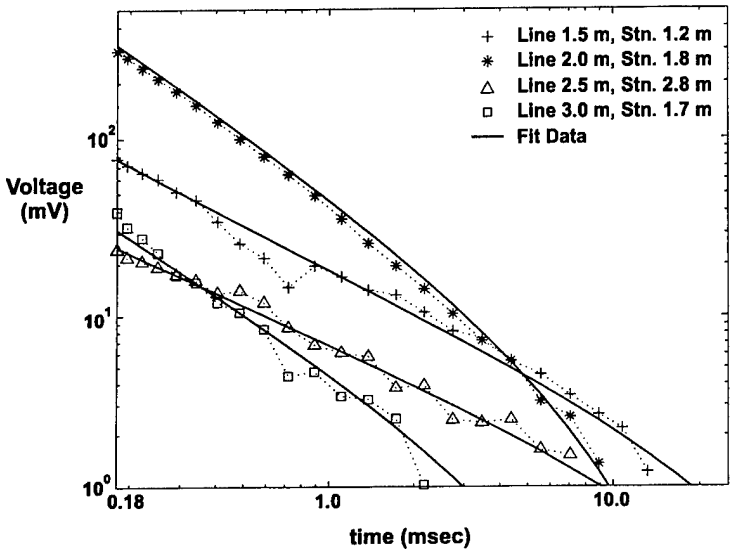

Figure 9: The observed and predicted decay curves for four stations in the 105 mm projectile UXO field data set inversion. The predicted decay of the vertical component of the measured voltages are represented by the solid lines, and the symbols represent the Geonics EM63 field measurements.

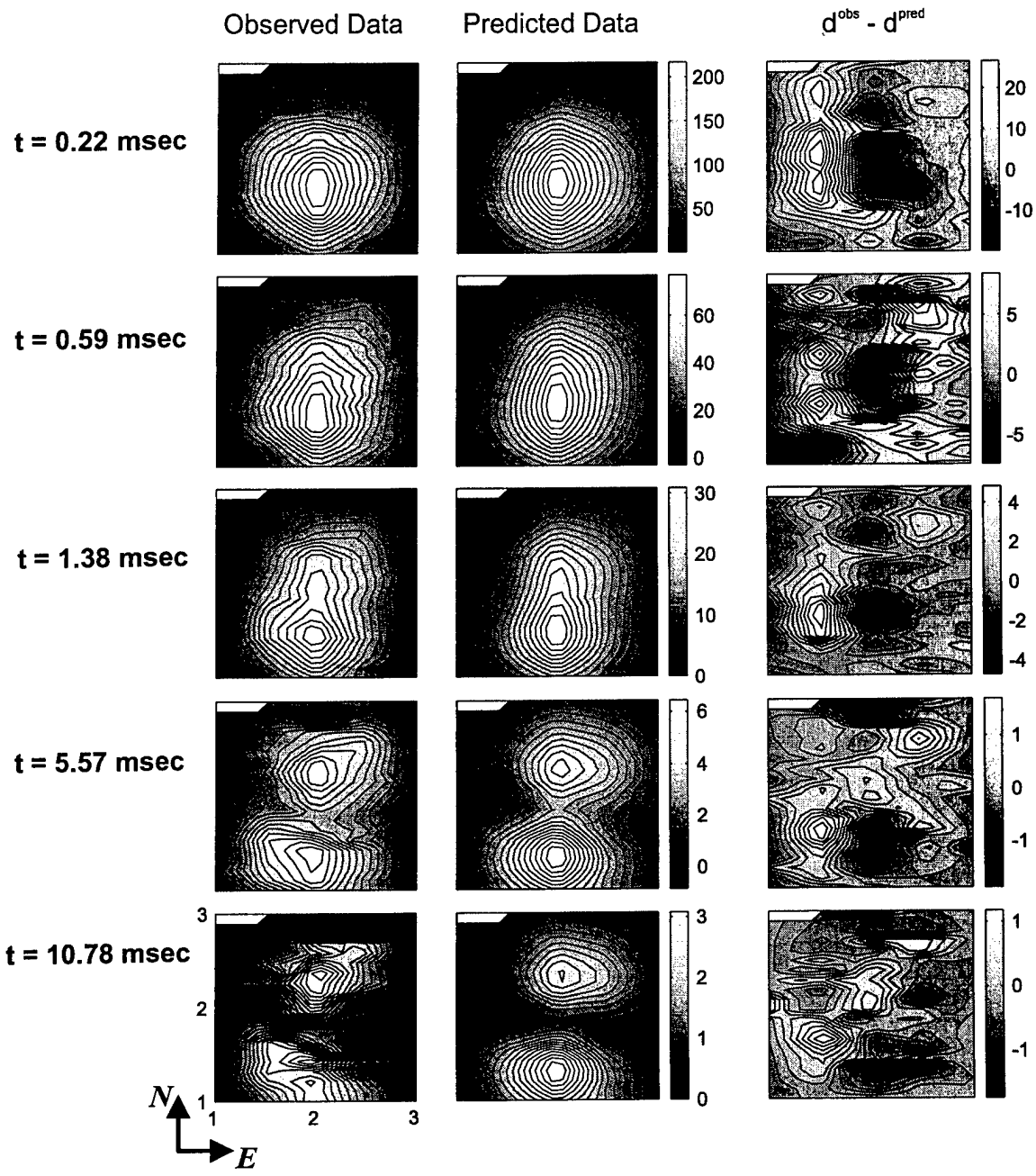

Figure 10: Plan view plots of the observed and predicted data for 5 of the 26 time channels in the 105 mm projectile UXO field data set inversion. The predicted data provide a reasonable match to the TEM response measured by the Geonics EM63.

(a) Location and Orientation

	m_o	m_{rec}	Expected Parameters	σ^{m}
Northing (m)	1.9	1.77	1.83	0.008
Easting (m)	2.15	2.04	2.00	0.005
Burial Depth (m)	0.6	0.47	0.44	0.01
ϕ (degrees)	45	10.1	~ 0	0.9
θ (degrees)	45	84.7	~ 90	0.13

(b) Decay Parameters

m_i	m_o	m_{rec}	σ^{m}
k_1	7.07	76.8	2.5
β_1	1.00	0.74	0.04
γ_1	3.16	31.8	8.3
k_2	7.07	29.2	3.7
β_2	1.00	1.08	0.07
γ_2	3.16	6.1	1.3

(c) Diagnostics

Diagnostic	Result	Conclusion
$\bar{\beta}$	0.91	permeable
k_1/k_2	2.63	rod-like
β_1/β_2	0.69	rod-like

Table 2: Recovered parameters for the field data inversion. Table (a) demonstrates that the inversion was successful in obtaining the approximate location and orientation of the target. Table (b) lists the recovered decay parameters of the two dipoles. Table (c) lists the results of applying the identification diagnostics to the recovered decay parameters. Application of the diagnostics indicates that the buried target is permeable and rod-like and therefore a candidate for UXO.

Part II

Verification of the Two-Dipole Modelling and Inversion Algorithm

1 EM63 Data Collection at the ERDC UXO Test Site

A series of TEM measurements was carried out between April 5 and April 21, 2000 at the Engineering Research Development Centre in Vicksburg, Mississippi to evaluate the applicability and performance of the forward modelling and inversion algorithm outlined in Part I of this report. The Geonics EM63 TEM sensor was used for all the data collection in this investigation. The EM63 is a multi-time channel time domain unit consisting of a $1m \times 1m$ square transmitter coil and a co-axial, horizontal $50cm$ diameter receiver coil mounted on a two-wheel trailer. More information about the EM63 sensor can be found in "EM63 Full Time Domain Electromagnetic UXO Detector: Operating Instructions" (2000).

Plan Measurements

A series of surveys were conducted over single targets seeded at the WES UXO test site (Figure 11). A $4m \times 4m$ square centered at ($18m\,N$, $24m\,E$) was chosen for the surveys. Prior to seeding the individual targets, EM63 and EM61-HH surveys were carried out to ensure that the area was "quiet", i.e. to ensure the area did not contain metallic scrap. The borders of the $4m \times 4m$ square were marked with string to indicate the extent of the survey area. Lines for each survey were run in a $N - S$ direction with a line spacing of $50cm$. The location of the sensor was measured more accurately by marking survey lines at $1m$ spacing with string and by dropping a plumb line from the center of the receiver/transmitter loop pair. The EM63 was set to record a time decay curve at $10cm$ intervals triggered by the odometer in the EM63 trailer wheels.

Targets measured in this survey setup included several UXO (37 mm projectile, 60 mm mortar, 81 mm mortar, stokes mortar, 105 mm mortar projectile, 155 mm projectile) and a variety of scrap items excavated during a UXO remediation project at Camp Croft, Maryland. These targets were placed at approximately the center of the grid ($2mN, 2mE$), and at depths up to $75cm$. In all cases the strike of the target was parallel to the line direction. In order to save time, the soil, removed when digging a hole for the target, was not replaced over the target. A wooden plank was placed over the hole in which the object was laid. Targets were generally measured in three orientations: horizontal, vertical, and an intermediate angle.

Decay Measurements

A controlled set of experiments was carried out to carefully examine how the secondary field of a target decays as a function of depth and orientation. For these experiments we required measurements with the EM63 transmitter/receiver coil directly above the center of various targets positioned at several depths and orientations.

In order to accurately and quickly position each target, Jose Llopis at WES designed and built a target holder (Figure 12(a)). The jig was made of wood and glue, contained no metallic materials, and could orient each target at 15 degree increments from vertical to horizontal. The size of the jig made it difficult

to bury. Therefore the jig was only partially buried and 2×6 planks were used to adjust the height between the EM63 and the target (Figure 12(b)). The height of the planks was varied by changing the number of cinder blocks used to elevate the planks. The majority of measurements were taken at two sensor heights: $Z \sim 50cm$ and $Z \sim 100cm$ from the center of the receiver to the center of the target, where Z is the vertical distance from the center of the target to the center of the receiver loop. Additional measurements with $Z \sim 75cm$ were made on a subset of the targets. TEM soundings were recorded for several UXO items ranging from a 37mm projectile to a 105 mm, as well as several scrap items. Samples soundings are plotted in Figure 13.

Several of the smaller, non-UXO items did not produce a significant response when placed in the jig. Therefore, they were measured using the setup of Figure 14(a). Each target was placed in two orientations and at ground level. To facilitate the collection of cleaner data, a pair of 6×2 inch planks was placed on the ground to provide a level surface for the EM63 to be pulled along. The measured voltage curves for scrap targets 1 to 8 are plotted in Figures 14(b) and (c). The line profiles for the first time channel ($t = 180\mu s$) and the tenth time channel ($t = 0.72msec$) are plotted in Figure 15.

EM63 TEM Survey of the ERDC UXO Test Site

The ERDC UXO Test Site consists of a $30m \times 95m$ grassy field containing seeded UXO and scrap. On the eastern end of the site there are approximately 25 targets buried along 4 north-south oriented rows. An EM63 survey was carried out between $75mE$ and $93.5mE$. The survey was completed with $1m$ line spacing and $10cm$ station spacing. In order to maintain straight lines, string was laid at $2m$ intervals. Two data sets were obtained. The first data set was from $75mE$ to $86.5mE$, and the second data set was from $82mE$ to $93.5mE$. Figures 16(a) and 16(b) contain contour plots for the first ($0.18ms$) and tenth ($0.72ms$) time channels. The plots were obtained by stitching together the two data sets. This was achieved by averaging the data collected on duplicate stations. For presentation purposes, the data in each contour plot was thresholded from below at a $1mV$ level and truncated above at levels indicated in the plot titles.

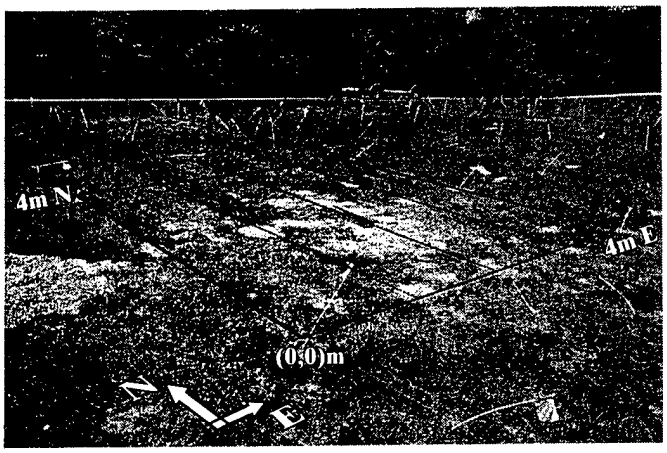

Figure 11: $4m \times 4m$ area on which a series of EM63 surveys were taken over different targets at several depths and orientations.

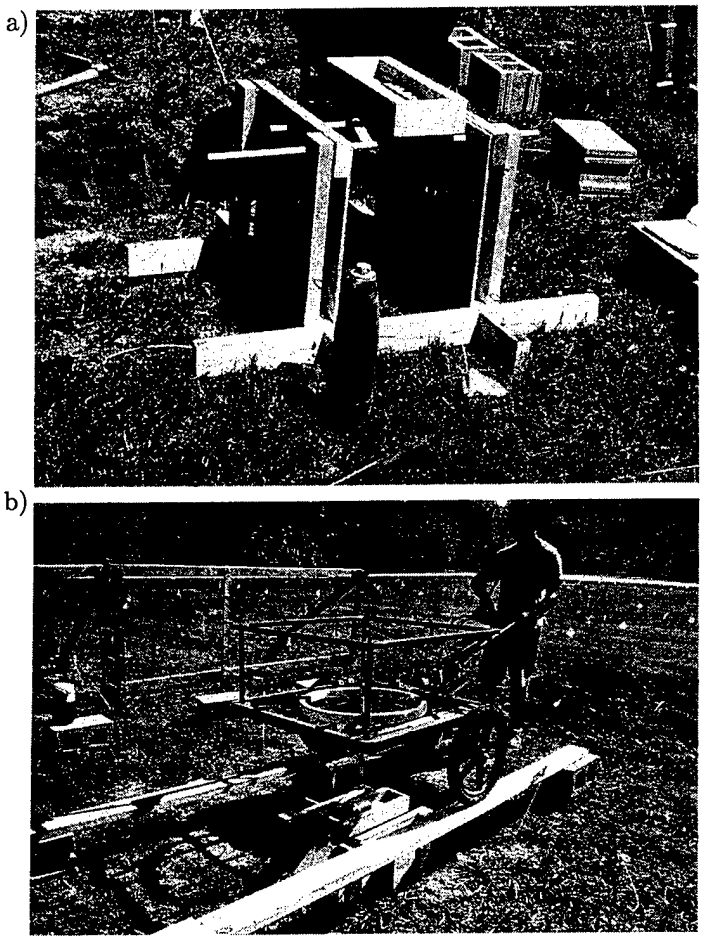

Figure 12: (a) Photograph of the wooden target holder for EM63 measurements. A 105mm projectile is standing beside the jig. (b) Measurement procedure when using the jig.

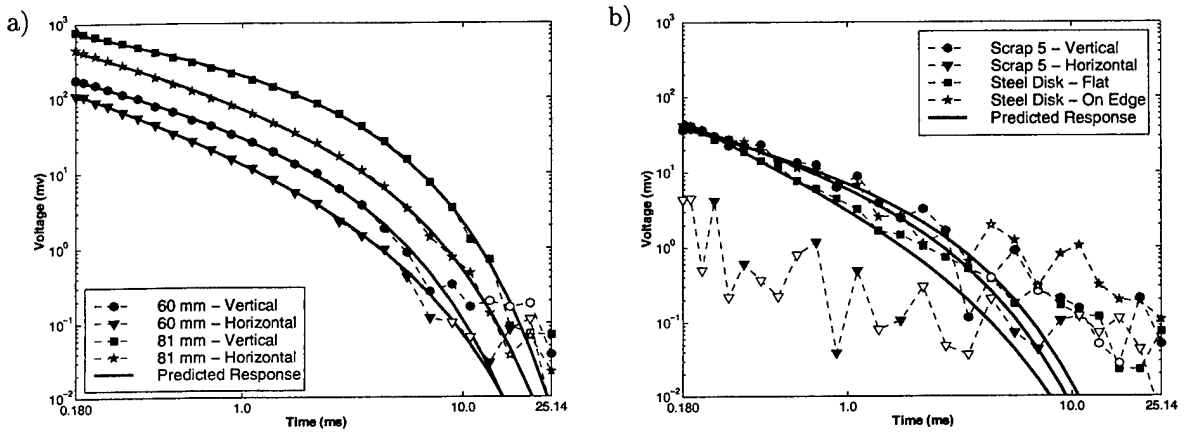

Figure 13: (a) Measurement of a 60 mm and 81 mm in jig. (b) Measurement of Scrap 5 and a Steel Disk. Unfilled symbols (e.g. 'o') indicate negative data that has its absolute value plotted. Predicted response is obtained by fitting the measurement with Equation 24.

a)

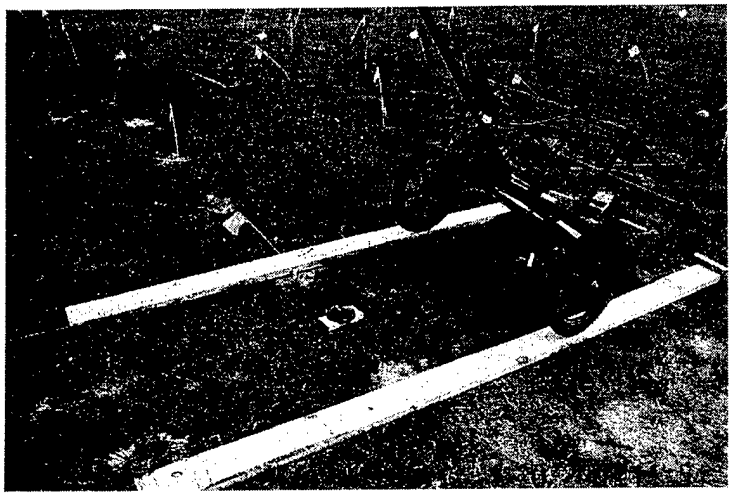

b)

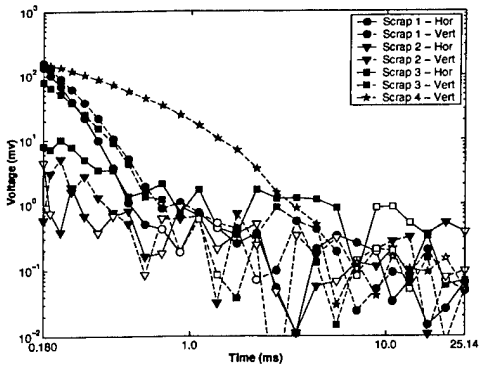

c)

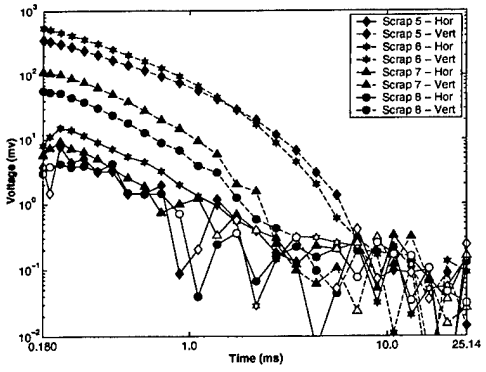

Figure 14: (a) Photograph of setup used to measure response of smaller scrap targets. (b) Voltage decay measurements for scrap targets 1 to 4. (c) Voltage decay measurements for scrap targets 5 to 8. Unfilled symbols (e.g. 'o') indicate negative data that has its absolute value plotted.

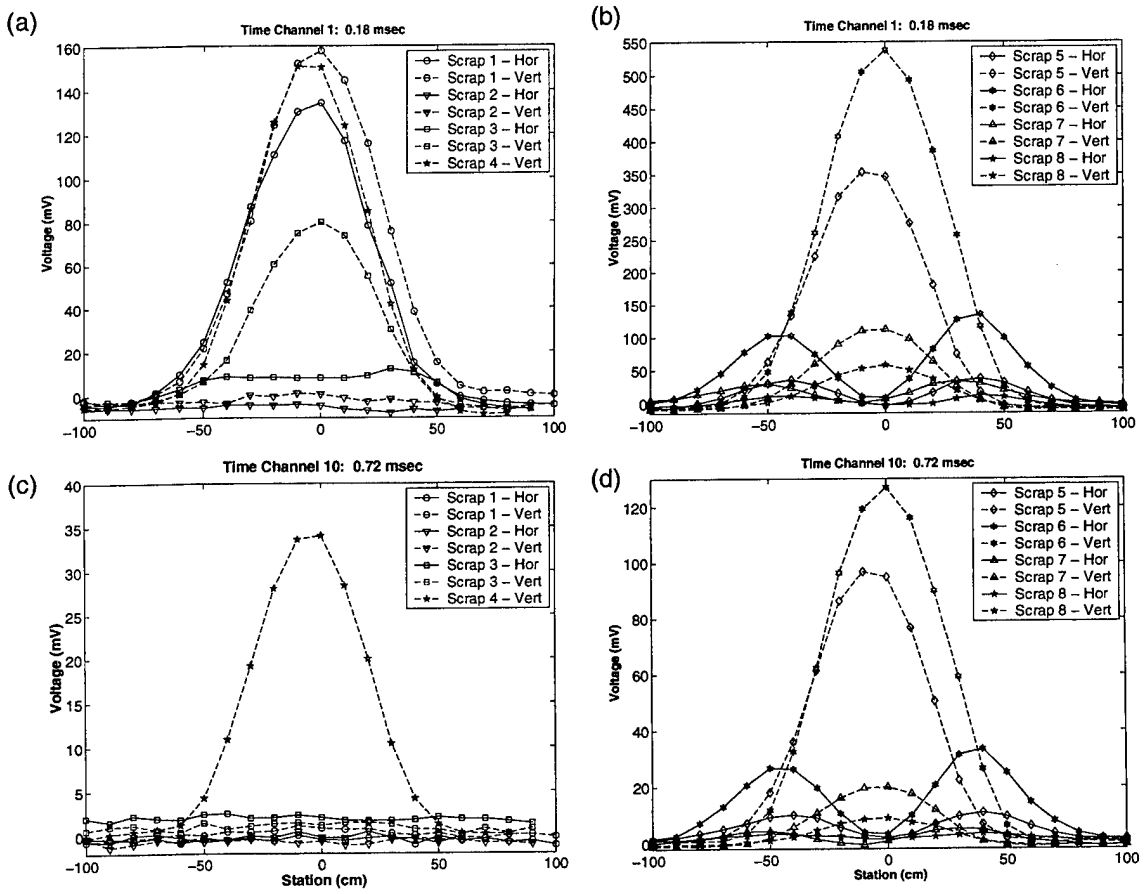

Figure 15: Measured response of scrap targets 1 to 8 along a line. Panel (a) and (b) plot the response along a line for the first time channel ($t = 0.18msec$). Panel(c) and (d) plot the response along a line for the tenth time channel ($t = 0.72msec$). Each target is located at station $0cm$.

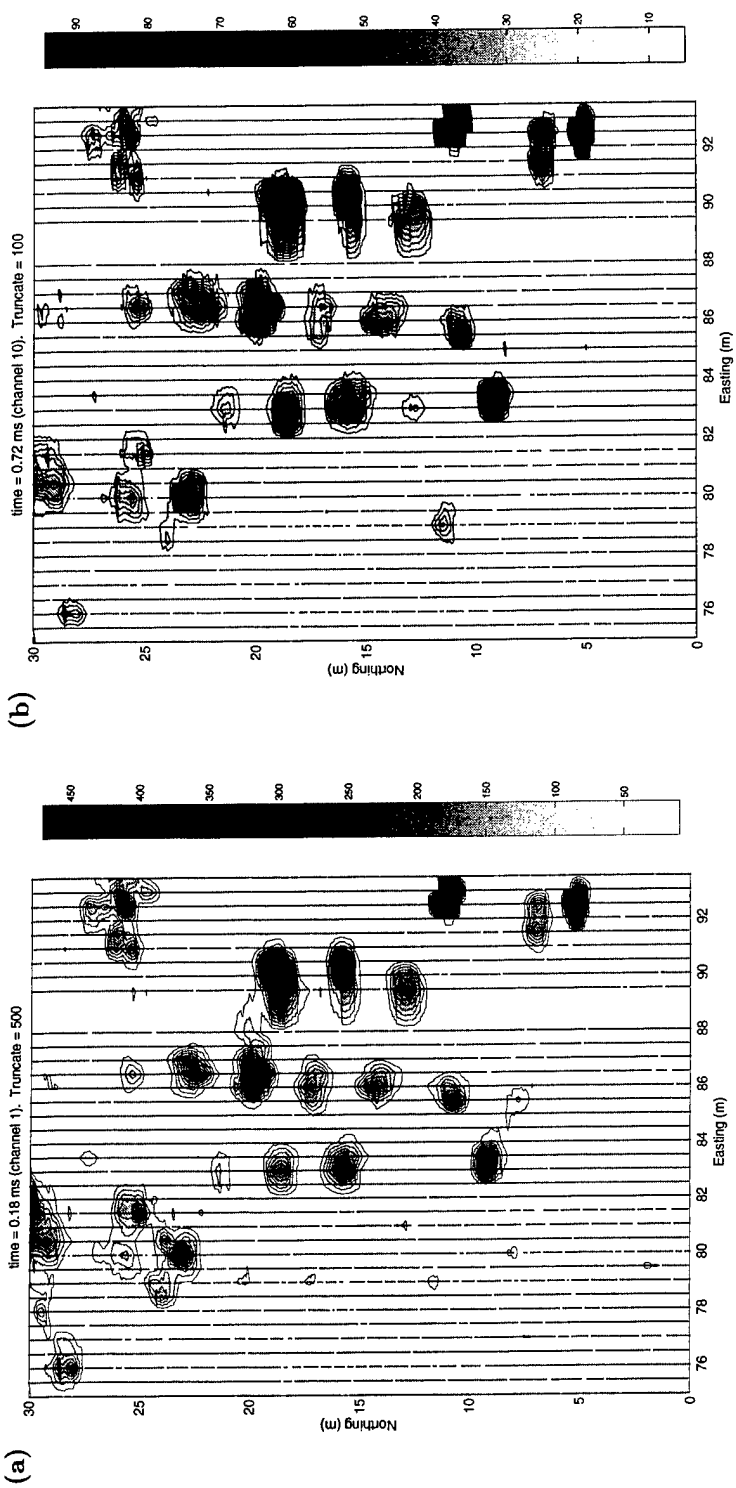

Figure 16: Survey of UXO test site at early time (time channel 1, $t = 0.18msec$). Survey of UXO test site at the tenth time channel (time channel 10, $t = 0.72msec$).

2 Verification of the Dipole Model

In Part I of this report an approximate forward model was proposed for the TEM response of a buried axi-symmetric metallic target. In this forward model the secondary field is approximated by a pair of orthogonal and independently decaying dipoles, whose strengths are proportional to the projection of the primary field onto their direction. The decay of each dipole moment is governed by the magnetic polarization tensor $\bar{\bar{\mathbf{M}}}$. The magnetic polarizability tensor is independent of transmitter/receiver/target geometry and is a function of the physical characteristics of the target alone. In our previous work we outlined a technique for exploiting $\bar{\bar{\mathbf{M}}}$ as a tool for characterizing the shape of target as either rod-like or plate-like, and if the target is ferrous or non-ferrous (Pasion (1999)). These results can only be applied with confidence for measurement configurations where the forward modelling is applicable.

This section contains a series of tests designed to verify that the magnetic polarization tensor is indeed independent of transmitter/receiver/target geometry. Each test follows the same procedure. First, the target is measured in two orientations: with the axis of symmetry parallel to the primary field and then perpendicular to the primary field. These measurements allow us to extract the target's two characteristic decay curves $L_1(t)$ and $L_2(t)$ that define the magnetic polarization tensor. Equipped with $\bar{\bar{\mathbf{M}}}$, we can then predict the TEM response for various locations and orientations and compare these results with measured data. In this section we evaluate the accuracy of these predictions.

Obtaining the Polarizability Tensor

Constructing the polarizability tensor $\bar{\bar{\mathbf{M}}}$ requires obtaining the dipole decay functions $L_1(t)$ and $L_2(t)$. The decay functions can be isolated by making two measurements: (1) with the primary field B^P parallel to the $\hat{\mathbf{z}}'$ axis of symmetry, and (2) with the primary field perpendicular to the $\hat{\mathbf{z}}'$ axis of symmetry.

Figure 17 illustrates the arrangement of the EM63 and target that we used to obtain the decay functions. In this geometry, the measured voltage is then

$$V(t) = \kappa \frac{B^P(Z)}{Z^3} 2\left[L_1(t)\cos^2\theta + L_2(t)\sin^2\theta\right] \tag{24}$$

where Z is the distance between the center of the receiver loop and the center of the target, and κ is a constant that depends on the size of the receiver and transmitter loops, the number of turns in each loop, and the transmitter current.

When the target's $\hat{\mathbf{z}}'$ axis of symmetry is parallel to the inducing field ($\theta = 0$ degrees, Figure 17(a)), only the $\mathbf{m}_1(t)$ dipole is excited, and the measured voltage is

$$V^{\parallel}(t) = \kappa \frac{B^P(Z)}{Z^3} 2L_1(t) = \left[2\kappa \frac{B^P(Z)}{Z^3}\right] k_1 (t+\alpha_1)^{-\beta_1} e^{-t/\gamma_1} \tag{25}$$

and when the target's $\hat{\mathbf{z}}'$ axis of symmetry is perpendicular to the inducing field ($\theta = 90$ degrees, Fig-

ure 17(b)), then only the $\mathbf{m}_2(t)$ dipole is excited and the observed voltage is

$$V^{\perp}(t) = \kappa \frac{B^P(Z)}{Z^3} 2L_2(t) = \left[2\kappa \frac{B^P(Z)}{Z^3}\right] k_2 (t+\alpha_2)^{-\beta_2} e^{-t/\gamma_2} \tag{26}$$

The voltage curves recorded by the EM63 for the parallel and perpendicular responses can be obtained by using a scaled down version of the inversion algorithm to recover the decay parameters (Pasion, 1999). Figure 17(c) and (d) give the result of this procedure applied to a 105 mm projectile and scrap 14. As expected for a rod-like target the L_1 component of the polarization tensor has a greater magnitude than the L_2 component. Figure 18 has the recovered $L_1(t)$ and $L_2(t)$ for the targets placed in the jig. Several of the curves have been extended by a "dash-dot" line that indicates an extrapolated portion of $L_1(t)$ and $L_2(t)$.

The accuracy of this procedure to obtain $L_1(t)$ and $L_2(t)$ will depend on experimental error and model error. Possible experimental errors include: (1) inaccurate measurement of Z; (2) inaccurate placement of the target beneath the receiver loop, i.e. the center of the target must be placed along the vertical axis passing through the center of the loop; (3) tilting of the EM63 trailer such that the primary field isn't vertical. Modelling errors describe instances where assumptions of the forward model are violated, such as: (1) uniformity of the primary field in the volume of the target; (2) representing the response as a point dipole; and (3) absence of fore-aft symmetry.

Test 1: Reproducing the time sounding at intermediate orientation

Once we determine the parameters of the magnetic polarization tensor, we can forward model the parameters to obtain the TEM response for any location, depth, and orientation. In this test we investigate how accurately we could predict the decay of the secondary field at an arbitrary orientation for a recovered magnetic polarization tensor.

Equation 24 describes the measured voltage in a receiver coil directly above a target illuminated by a purely vertical primary field. Using Equation 24 and the decay functions $L_1(t)$ and $L_2(t)$ obtained in the analysis of the previous section, we predict the voltage response and compare it to measurements using the EM63. The set of measurements we use for comparison were those obtained using the target holder. Figures 19 and 20 compare the measured responses at different angles and the response predicted by the forward model for an 81mm mortar without fins. Figure 19 has the measured voltage curves at different heights from the sensor. $L_1(t)$ and $L_2(t)$, obtained by fitting these curves with equations 25 and 26, are then forward modelled and plotted in Figure 20. The top two panels of Figure 20 demonstrate the procedure on an 81mm mortar (without fins) located approximately $55cm$ beneath the receiver loop. At this distance (equivalent to approximately 10 cm below the surface) we see that the representation is only moderately good at reproducing the data at the different angles. When we repeat the procedure for data collected approximately $100cm$ beneath the receiver, we see that the model does a better job of predicting the data. This is not surprising, since we would expect the modelling of a compact metallic object as a dipole to become more applicable as we move further from the source/receiver loop.

Test 2: Reproducing the spatial behavior

In our second test we focus on how accurately we could predict the spatial response of a target using the dipole model. For this investigation we first use a target's magnetic polarization tensor, obtained in the manner described in the previous section, to predict the secondary field over a survey line that passes directly over the target. In each case the survey line is co-aligned with the target. This predicted response is then compared with the measured response.

In Figures 22 to 30, the predicted and measured responses along a line are plotted for several targets in three orientations: vertical, horizontal, and at an intermediate dip angle. At intermediate angles the target dips towards the end of the line (i.e. dips downwards to the right in Figures 22 to 30). Figures 22 to 30 indicate the model is successful in predicting the response along each survey line.

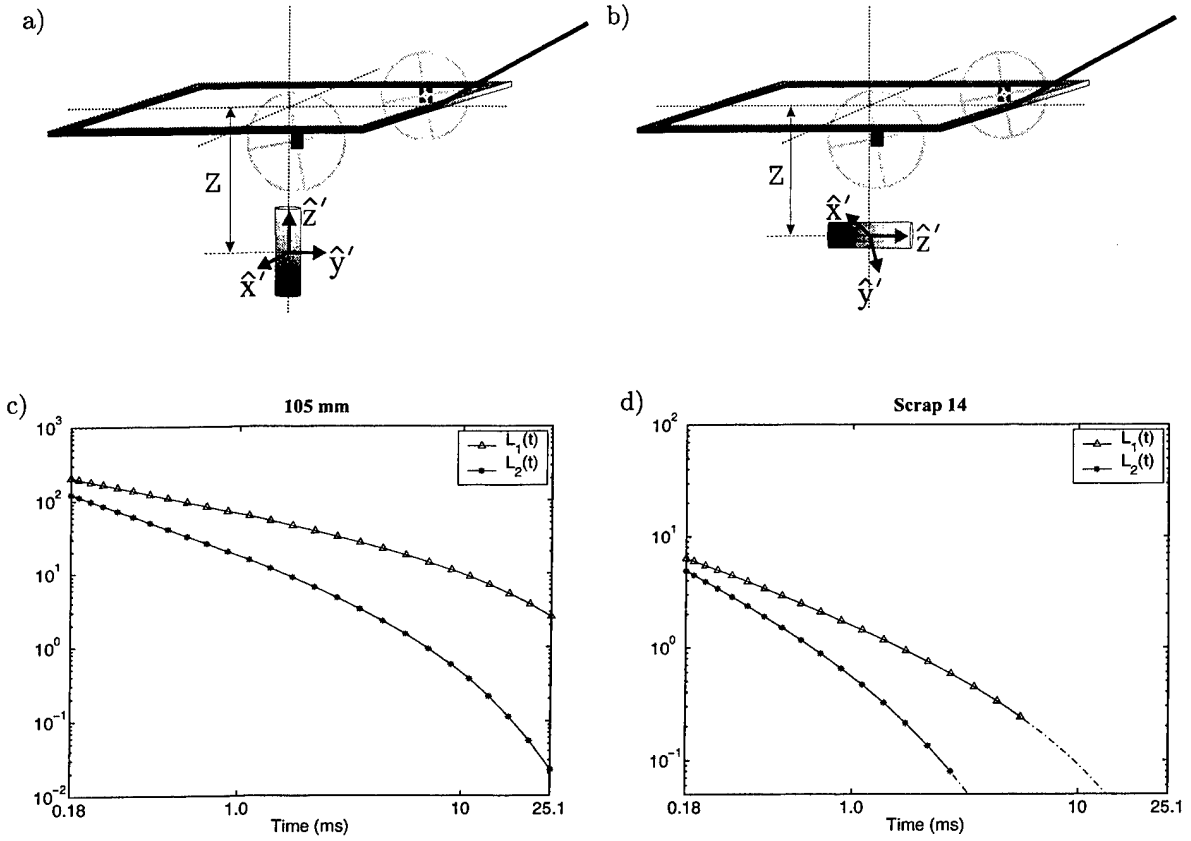

Figure 17: (a) EM63 and target geometry used to obtain $L_1(t)$. (b) EM63 and target geometry used to obtain $L_2(t)$. (c) $L_1(t)$ and $L_2(t)$ curves for a 105mm projectile. (d) $L_1(t)$ and $L_2(t)$ curves for Scrap 14 (See Appendix A for a photo, size, and weight of Scrap 14).

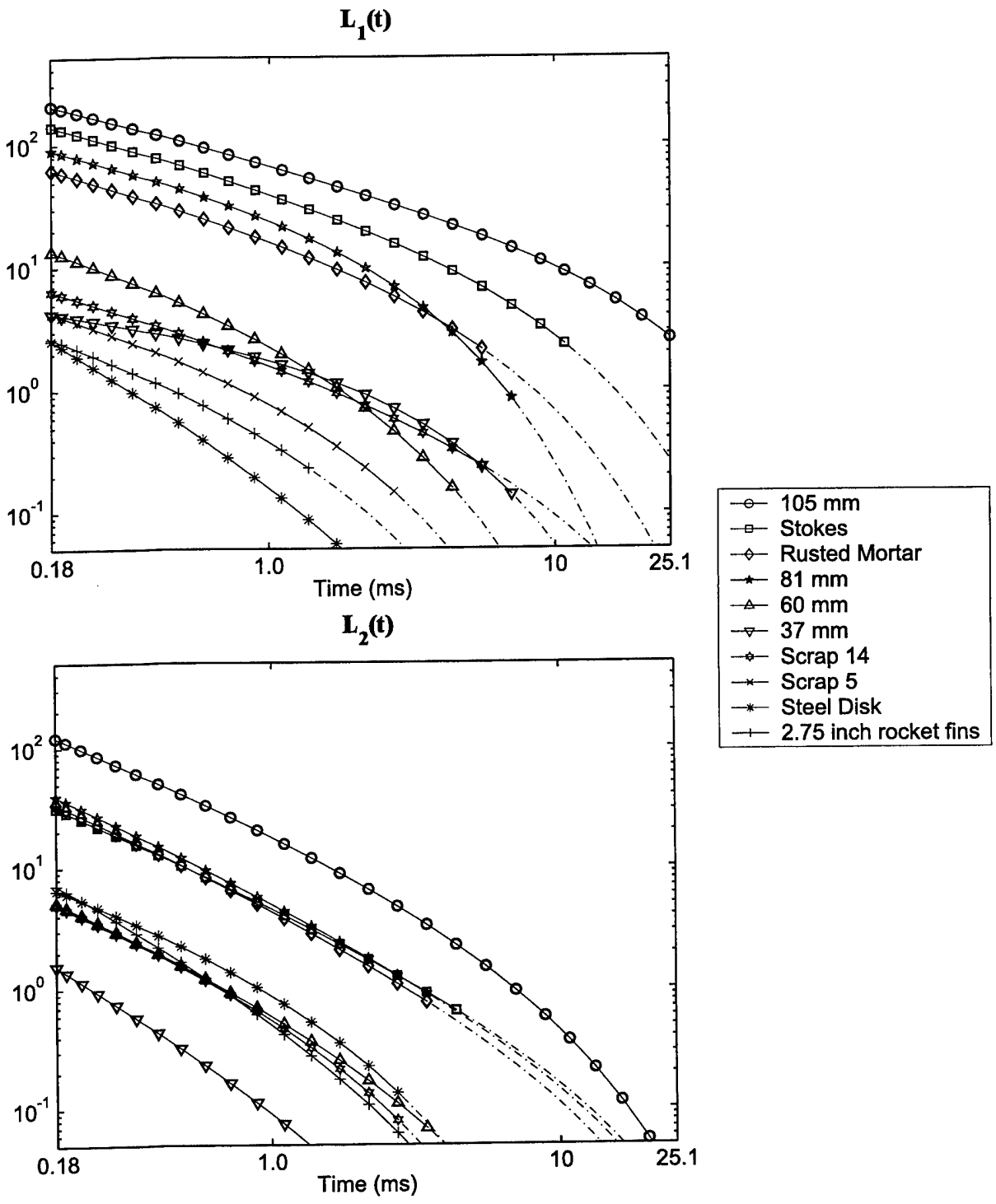

Figure 18: $L_1(t)$ and $L_2(t)$ decay functions for different targets. Photographs and target descriptions can be found in Appendix A

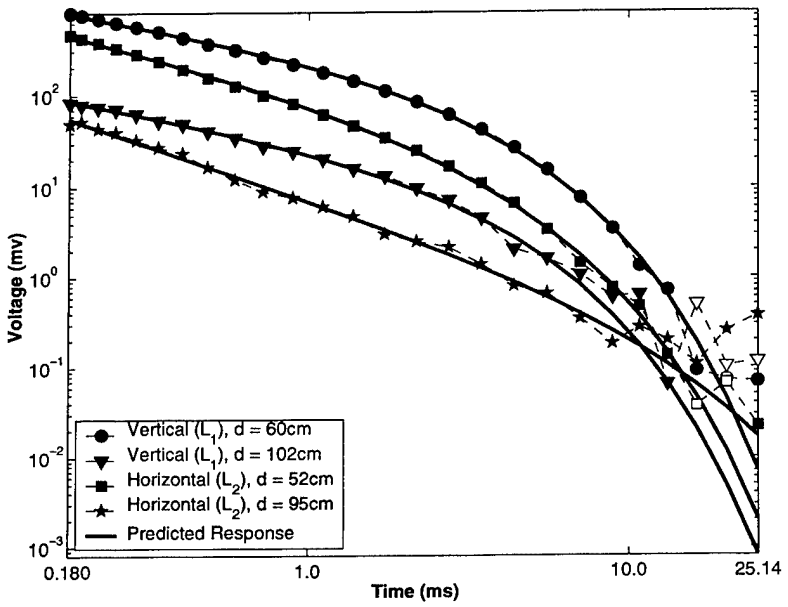

Figure 19: Measured voltage curves for a 81 mm Mortar without fins at different heights from the sensor. Unfilled symbols (e.g. '□') indicate negative data that has its absolute value plotted. These curves were inverted to obtain $L_1(t)$ and $L_2(t)$. Clearly, the decay nature of the signal changes when the mortar is brought close to the sensor. The resulting $L_1(t)$ and $L_2(t)$ curves are used to predict the decay at intermediate angles in Figure 20.

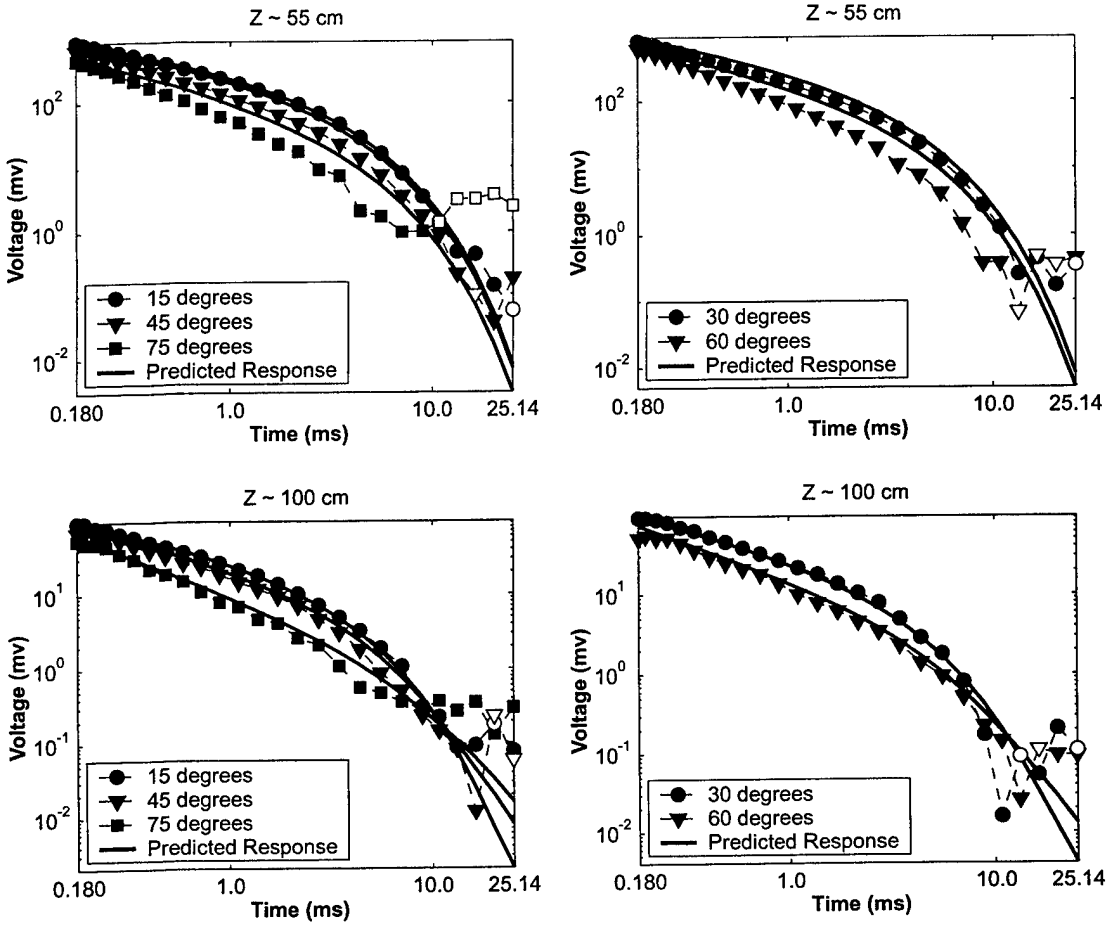

Figure 20: Predicting the measured voltage decay curves for an 81 mm mortar without fins at different orientations θ. Unfilled symbols (e.g. '□') indicate negative data that has its absolute value plotted. The $L_1(t)$ and $L_2(t)$ decay curves recovered from measurements with $Z = 60cm$ and $Z = 52cm$ (see figure 19, respectively, are used to predict the voltage curves in the top two panels. The $L_1(t)$ and $L_2(t)$ decay curves recovered from measurements with $Z = 102cm$ and $Z = 95cm$, respectively, are used to predict the voltage curves in the bottom two panels. The prediction of the measured curves is more successful when the target is farther away from the sensors.

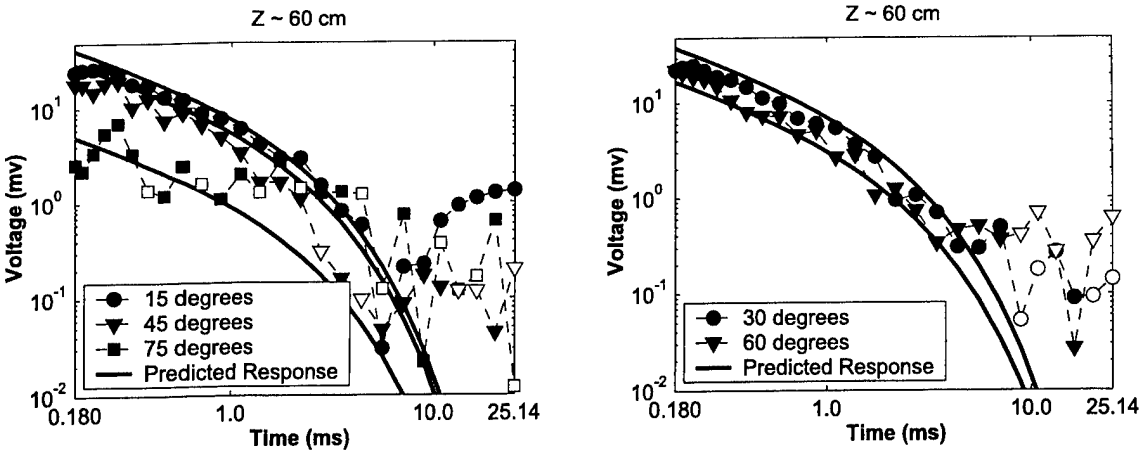

Figure 21: Predicting the measured voltage decay curve for Scrap 5 using the dipole model.

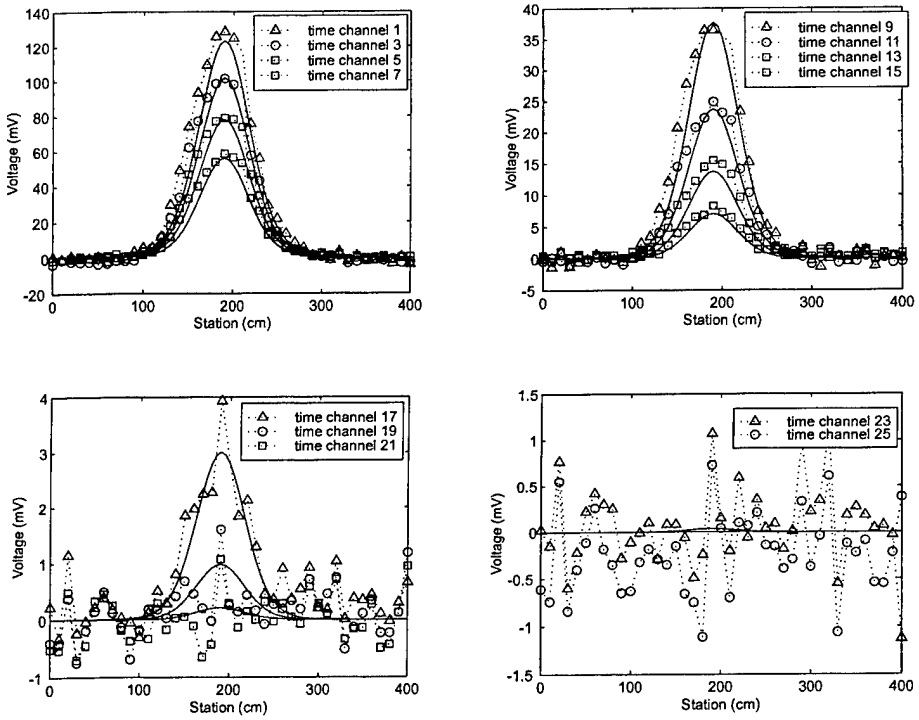

Figure 22: **60mm Mortar**: θ =0 degrees (vertical), $Z = 73cm$.

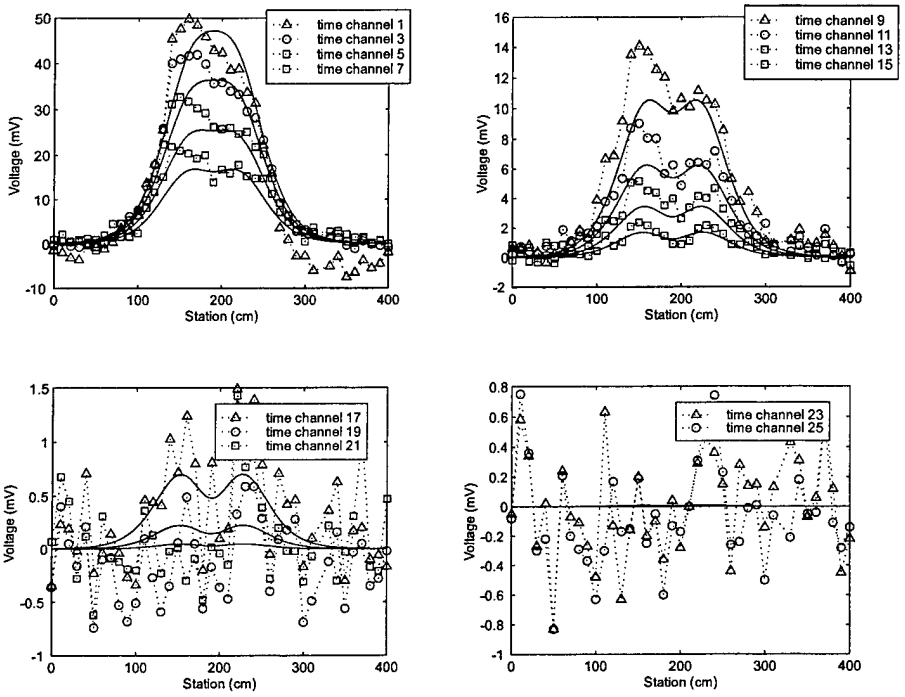

Figure 23: **60mm Mortar**: θ =90 degrees (horizontal), $Z = 73cm$.

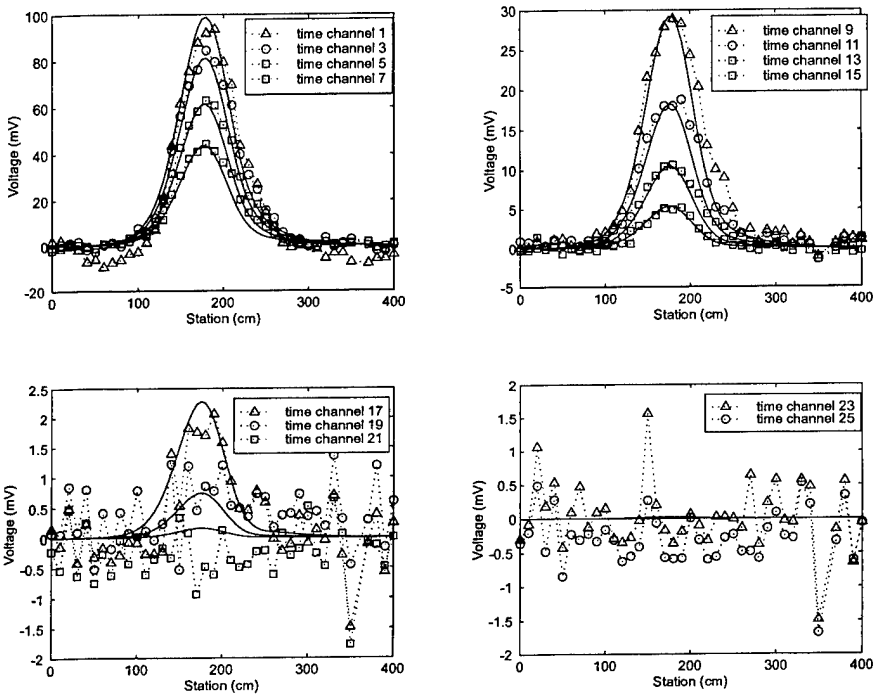

Figure 24: **60mm Mortar**: θ =40 degrees, $Z = 75cm$.

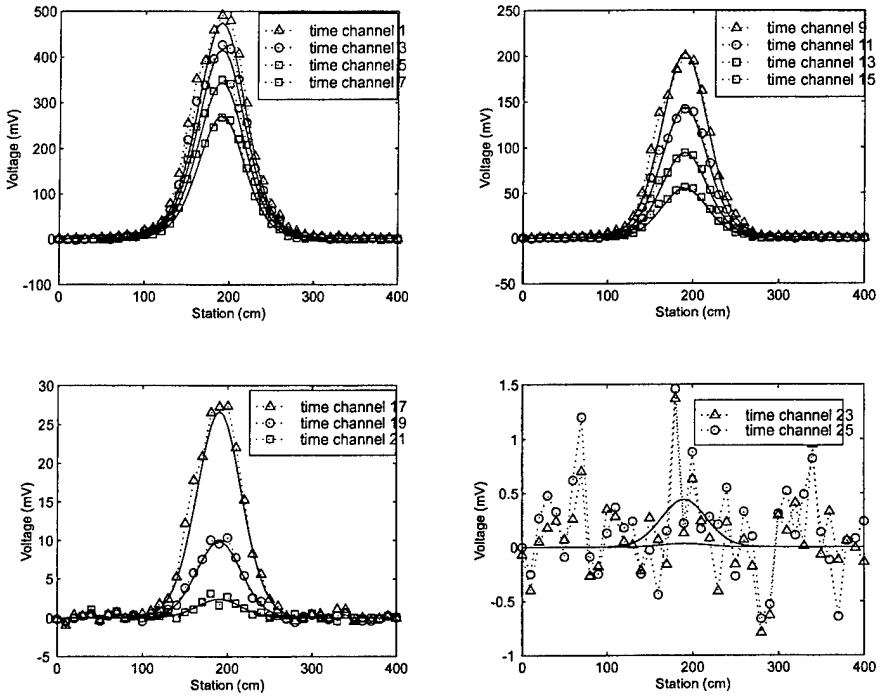

Figure 25: **81mm Mortar**: θ =0 degrees (vertical), $Z = 73cm$.

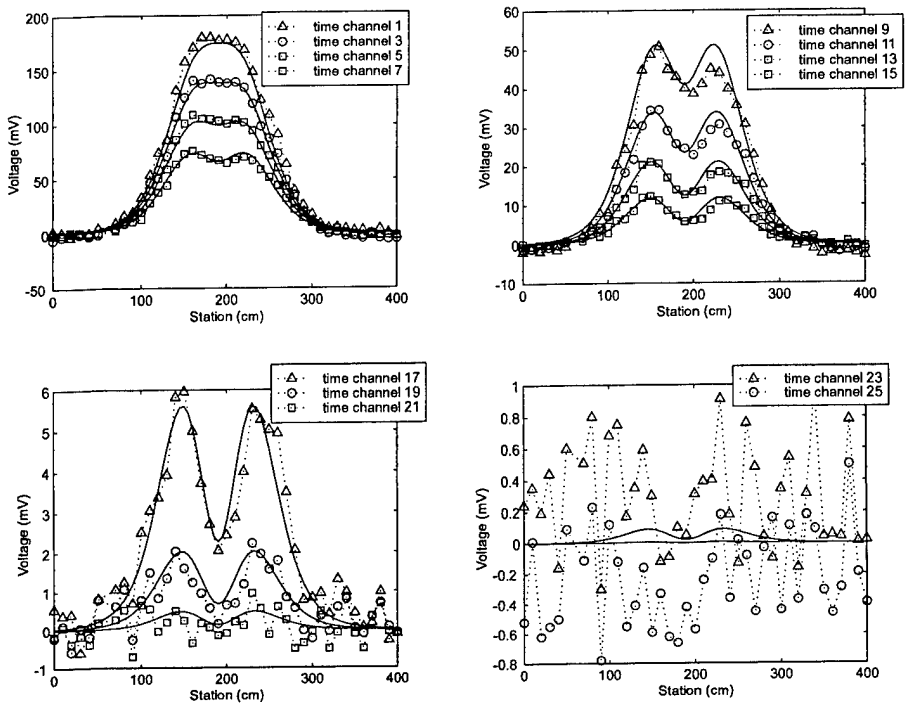

Figure 26: **81mm Mortar**: θ =90 degrees (horizontal), $Z = 73cm$.

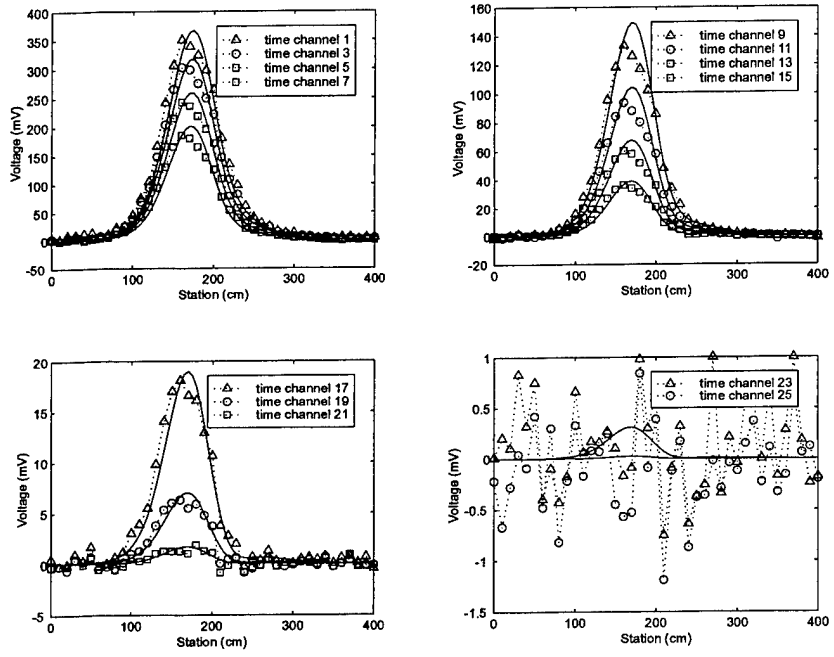

Figure 27: **81mm Mortar**: θ =43 degrees, $Z = 74cm$.

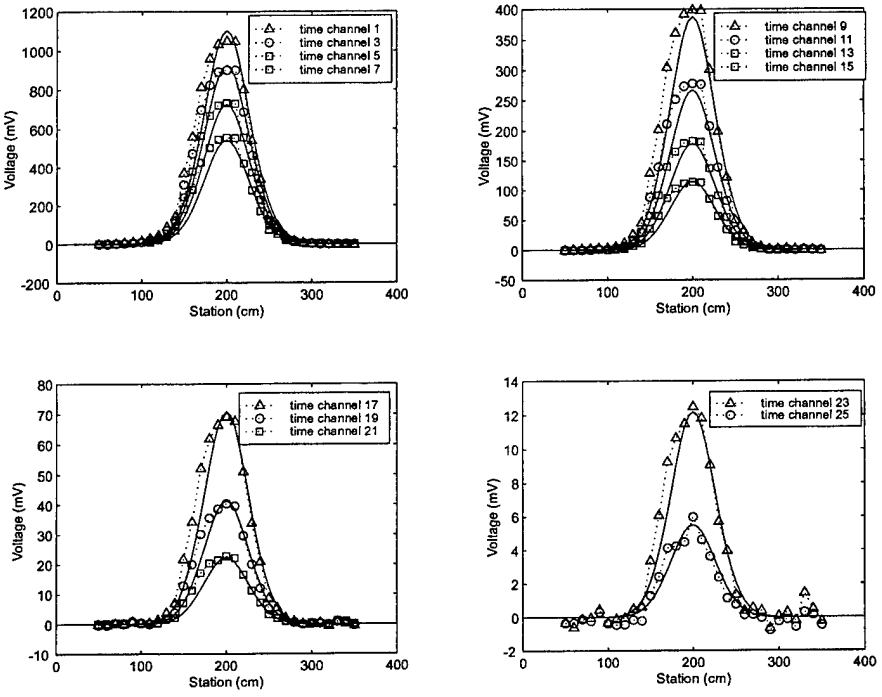

Figure 28: **Stokes Mortar**: θ =90 degrees (vertical), $Z = 73cm$.

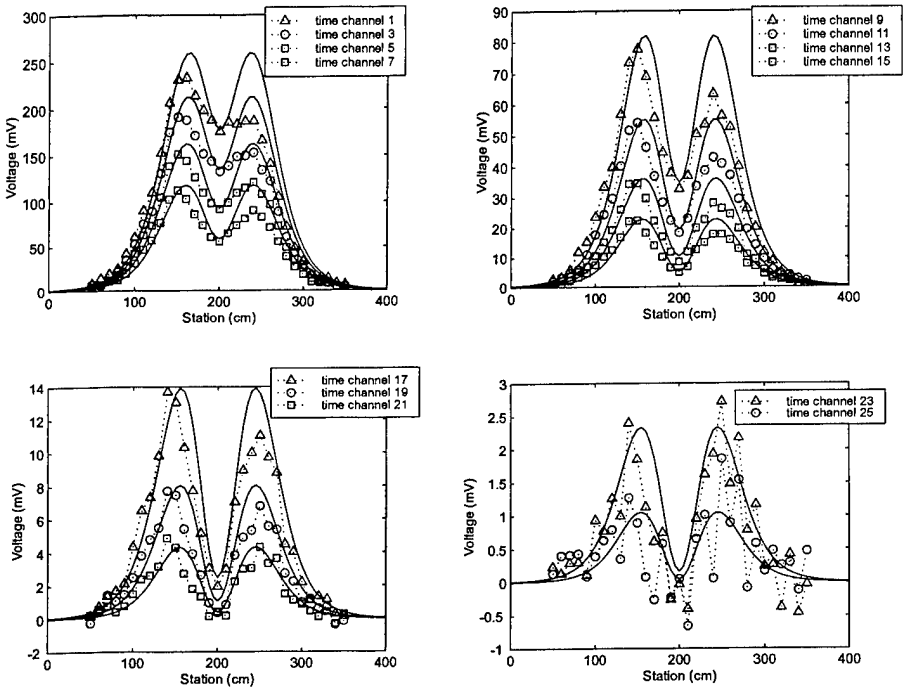

Figure 29: **Stokes Mortar**: θ =90 degrees (horizontal), $Z = 73cm$.

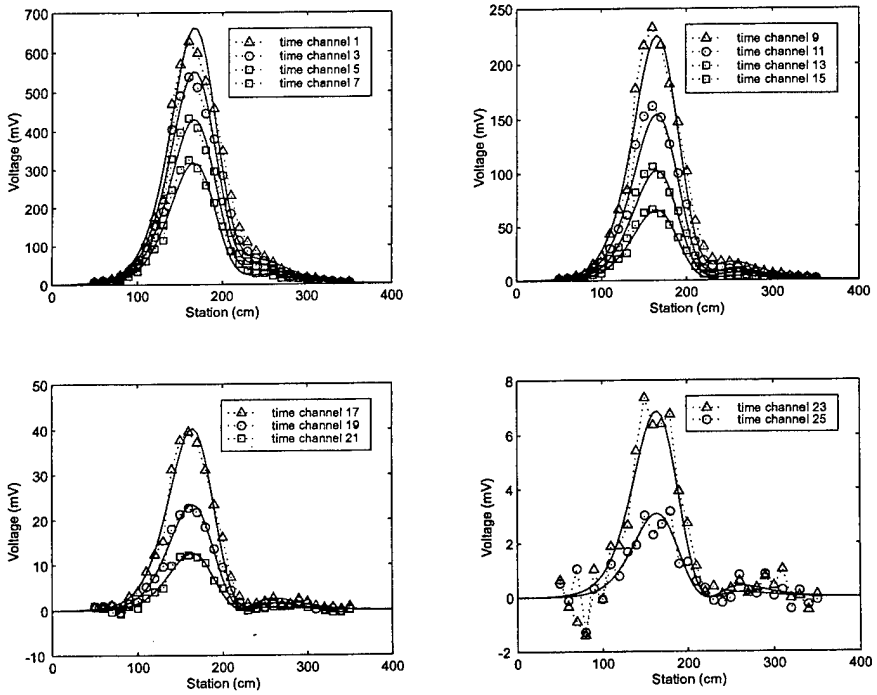

Figure 30: **Stokes Mortar:** θ =54 degrees, $Z = 73cm$.

3 Inversion of TEM Data Collected at the ERDC Test Site

In Part I of this report we described a method of inverting TEM data for the 13 parameters of the Two-Dipole model. We formulated a non-linear least squares problem that involved minimizing

$$\Phi(\mathsf{m}) = \frac{1}{2}\|\mathsf{W}_d\left(F[\mathsf{m}] - \mathsf{d}^{obs}\right)\|^2 \tag{27}$$

where $F[\mathsf{m}]$ is the forward modelled data, d^{obs} is the observed data, and Φ is the least squares objective function that measures how closely our predicted data matches the observed data. W_d is the data weighting matrix

$$(\mathsf{W}_d)_{ii} = \frac{1}{\rho d_i + \epsilon} \tag{28}$$

where ρ is typically a percentage and ϵ is a constant that characterizes ambient noise.

In Part I we performed two transformations to the model: (1) a simple linear scaling to the model m to ensure that each component of m is approximately unity, and (2) replacing each of the time decay parameters m_i by a squared variable w_i such that $m_i = x_i^2$ to ensure positivity of the decay parameters. For the inversions in Part II of this report we retain the linear scaling of the model, but we no longer solve the square-variable unconstrained problem. Instead we reformulate the inversion so that it can be solved by a constrained optimization procedure. We use a Projected BFGS algorithm, described in "Iterative Methods for Optimization" (Kelley, 1999), to minimize the objective function. In this algorithm we are required to supply a starting model as well as upper and lower constraints for each variable.

Selection of Starting Parameters

The first step of this inversion procedure is to make a starting guess for the 13 model parameters:

$$\mathsf{m} = [X, Y, Z, \phi, \theta, k_1, \alpha_1, \beta_1, \gamma_1, k_2, \alpha_2, \beta_2, \gamma_2] \tag{29}$$

The success of a local inversion procedure, as well as the rate of convergence towards a solution is dependent on the quality of the initial guess (Bard, 1974). The following section will discuss a number of simple data preprocessing strategies that enables us to make a reasonable initial guess of the above parameters.

Location on Survey (X, Y)

A natural idea for determining the location for a target would be to find the location at which the maximum signal occurs. This technique would produce the exact location for a spherical target, where the plot of the vertical ($\hat{\mathbf{z}}$) secondary field produces a circular "bulls-eye" anomaly with a maximum

located directly over the target (Figure 31(a)). However rod-like and plate-like targets can produce non-symmetric anomalies with multiple local maxima (Figure 31(b)). In these cases, search for the maximum signal will give an inaccurate estimation of target location. To account for these possible anomaly types, we use an approximation of the first spatial moment of the data to estimate the location (X^{est}, Y^{est}) on the survey:

$$X^{est} = \frac{\sum_{i=1}^{N} V_i(t_1)\, x_i}{\sum_{i=1}^{N} V_i(t_1)}, \quad \text{and} \quad Y^{est} = \frac{\sum_{i=1}^{N} V_i(t_1)\, y_i}{\sum_{i=1}^{N} V_i(t_1)} \tag{30}$$

where there are N total stations in the survey and $V_i(t_1)$ is the voltage measured at the i^{th} station at location (x_i, y_i), and at the first time channel. Figure 31 compares this technique to simply using the maximum value.

Depth of target (Z)

The full width at half maximum (FWHM) is a standard technique for estimating a target's depth. In general, the plotted anomaly of non-spherical targets will not be circularly symmetric. In these cases, it is not clear which profile to use for calculating the FWHM. Therefore we modify the FWHM technique by plotting points of the secondary field anomaly at an early time channel that are greater than one-half of the maximum signal. The estimate for the depth of the target is then

$$\text{Estimated Depth} = Z^{est} = 2\sqrt{\frac{A}{\pi}} \tag{31}$$

where A is the area of the portion of the secondary field anomaly greater than one-half of the maximum signal.

Orientation (ϕ, θ)

The orientation angles ϕ and θ are not estimated prior to the inversion. The starting values for ϕ and θ set to 45 degrees.

Decay Parameters $(k_i, \alpha_i, \beta_i, \gamma_i)$

The decay parameters contained within the decay functions $L_1(t)$ and $L_2(t)$ are estimated in the same manner described in Pasion (1999). The decay parameters are estimated by taking the estimate of the target location and extracting the decay curve at that location. The decay curve is then fit with the function

$$\xi(t) = \kappa \frac{B^P(Z^{est})}{(Z^{est})^3} 2\tilde{k}\,(\tilde{\alpha} + t)^{\tilde{\beta}}\, e^{t/\tilde{\gamma}} \tag{32}$$

where Z^{est} is the estimated depth. The starting decay parameters for both dipoles 1 and 2 are then $(\tilde{k}, \tilde{\alpha}, \tilde{\beta}, \tilde{\gamma})$. Equation 32 is obtained by setting $L_1 = L_2$ in equation 24.

Selection of Upper and Lower Limits

The non-linear least squares objective function (equation 27) is minimized using an optimization algorithm that incorporates box constraints. Box constraints are the lower and upper limits that we place on the model parameters that represent the minimum and maximum possible values of the model parameters. The upper and lower limits used for the model parameters are summarized in Table 3.

Location (X, Y) and Depth (Z)

For the inversion results presented here conservative constraints were applied. The location was constrained to a $1m$ square box centered at $(X, Y) = (2m, 2m)$, and the depth was constrained between $Z_{low} = 0.43m$ which is the level of the ground, and $Z_{high} = 1.5m$.

Orientation (ϕ, θ)

Since we do not estimate the orientation of the target based on the plotted anomaly, the upper and lower limits of ϕ and θ are determined to be the limits that allow for all possible orientations of the target. Therefore, $-90 < \phi < 90$ and $0 < \theta < 180$.

Decay Parameters $(k_i, \alpha_i, \beta_i, \gamma_i)$

In verifying the applicability of the approximate forward model (Section 2), the decay parameters were recovered for different scrap and UXO targets. From this analysis, and the analysis reported in Pasion (1999), upper and lower limits for the decay parameters were chosen. The limits are listed in Table 3(b).

Application to Field Data Sets

In this section we present the results of applying the inversion algorithm to five targets: 155 mm, 105 mm, 81 mm, 60 mm, and Stokes mortar. A list of inversion results presented in this report can be found in Table 4, where the target type, depth, and orientation for each data set inverted in this section are given. Each inverted data set consisted of soundings collected on a 2 m × 2 m grid centered on the target, containing 5 lines running North-South separated at 50 cm line spacing, with stations located at 5 cm intervals along each line. Inversion results can be found in Figures 32 to 48. In Panel (a) of each figure is a plan view comparison of the observed and predicted data for time channels 1, 8, 15, and 23. Panel (b) compares the predicted and observed decay at three stations: Line 1 m, Station 1m; Line 2 m, Station 2 m; and Line 2.5 m, Station 2.5 m. The recovered location and orientation are listed in Panel (c), and the recovered decay parameters and diagnostics applied to those parameters are reported in Panel (d). The algorithm was successful in identifying each target as rod-like and permeable for all the cases presented here.

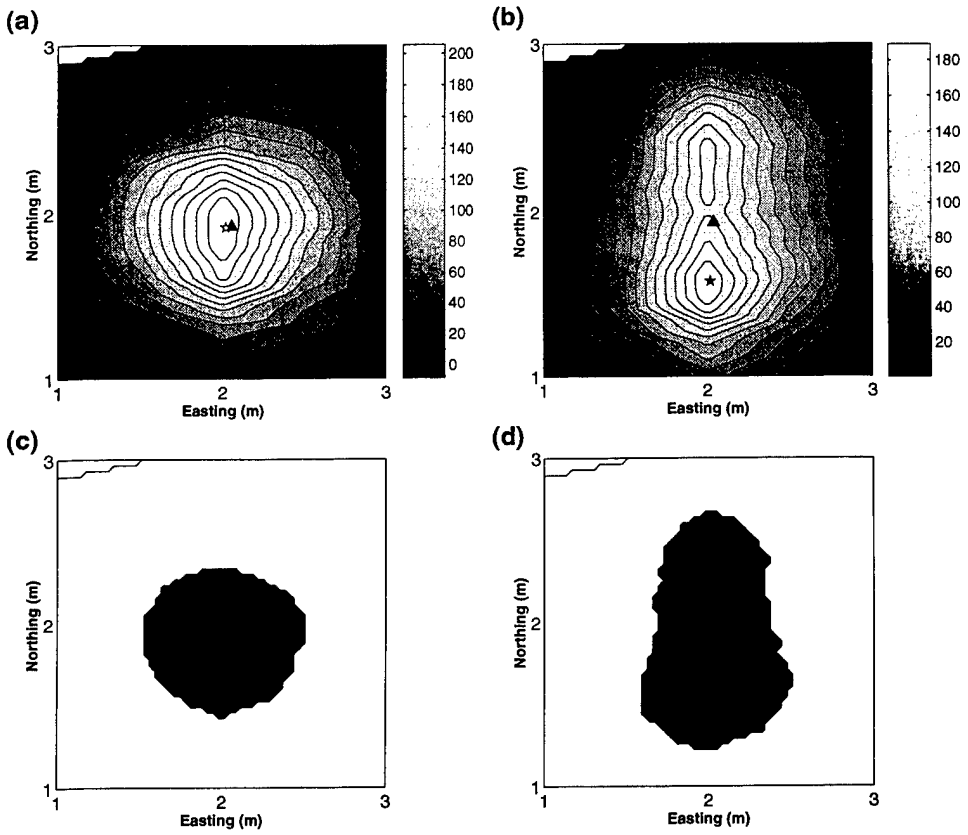

Figure 31: Finding the location of a (a) sphere and (b) horizontal stokes mortar. The location obtained by using the maximum of the signal is indicated by the star, and the location obtained by using the "center-of mass" is indicated by the triangle. The center-of-mass is much better at determining the location of the target when the plotted anomaly does not have the appearance of a "bulls-eye" (e.g. a sphere). Panels (c) and (d) plot those data points that are greater than half the maximum signal. Panel (d) indicates that the traditional "Full-Width-at-Half-Maximum" would be difficult to utilize for non-"bulls-eye" anomalies.

(a) Location and Orientation

m_i	m_i^{low}	m_i^{up}
X (m)	1.5	2.5
Y (m)	1.5	2.5
Z (m)	0.43	1.5
ϕ (degrees)	-90	90
θ (degrees)	0	180

(b) Decay Parameters

m_i	m_i^{low}	m_i^{up}
k_i	0.1	200
α_i	0.001	0.02
β_i	0.3	1.5
γ_i	2	30

Table 3: Upper and lower limits used in inversion examples in Part II of this report.

Target	Z (cm)	θ (degrees)	Figure No.
155 mm	98	0	32
155 mm	97	52	33
155 mm	91	90	34
105 mm	86	0	35
105 mm	87	90	36
105 mm	89	59	37
105 mm	89	40	38
Stokes Mortar	73	54	39
Stokes Mortar	73	0	40
Stokes Mortar	73	90	41
81 mm	73	0	42
81 mm	74	43	43
81 mm	73	90	44
60 mm	58	57	45
60 mm	58	90	46
60 mm	59	0 (nose up)	47
60 mm	59	0 (nose down)	48

Table 4: Targets

155 mm: $\theta = 0$ degrees (vertical), $Z = 98cm$

(a)

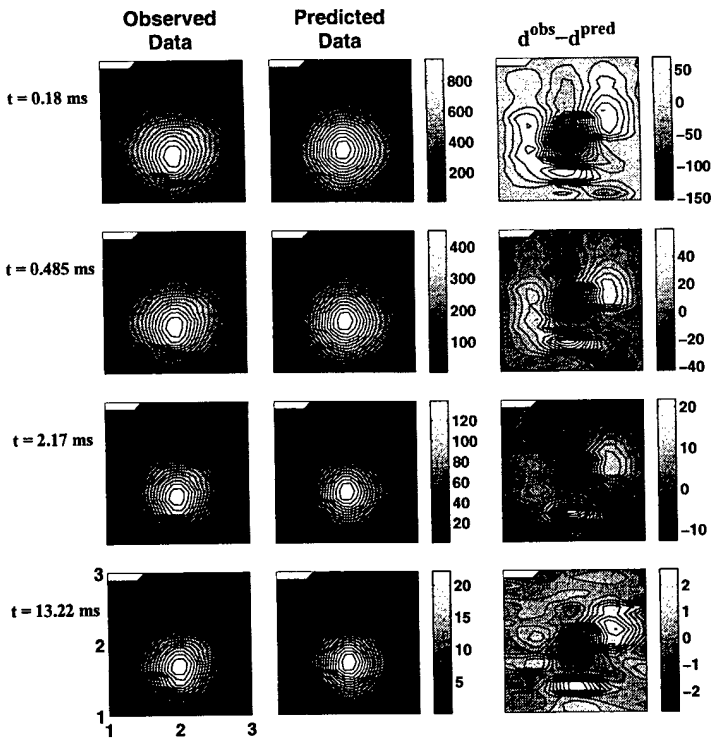

(b)

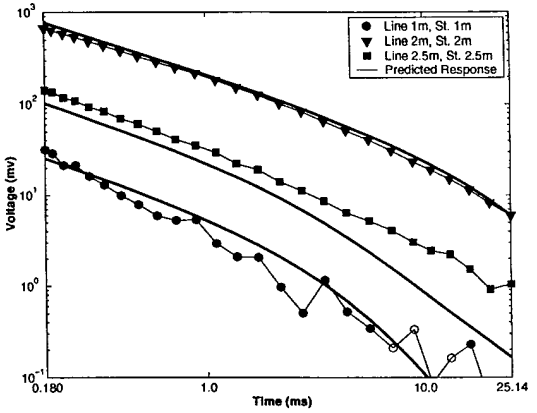

(c) Location and Orientation

	m_o	m_{rec}	m_{exp}
Northing (m)	1.79	1.73	1.81
Easting (m)	2.03	2.05	2.00
Z (m)	0.972	0.934	0.98
ϕ (degrees)	45	90.0	~ 0
θ (degrees)	45	7.2	~ 0

(d) Decay Parameters and Diagnostics

m_i	m_o	m_{rec}
k_1	222.34	199.17
α_1	0.020	0.004
β_1	0.74	0.73
γ_1	21.95	21.95
k_2	222.34	123.64
α_2	0.020	0.001
β_2	0.74	0.80
γ_2	21.95	3.56

	Result	Conclusion
$\bar{\beta}$	0.77	Permeable
k_1/k_2	1.61	Rod-like
β_1/β_2	0.92	Rod-like

Figure 32: Recovered parameters for the field data inversion of a 155mm projectile.

155 mm: $\theta = 52$ degrees, $Z = 97cm$

(a)

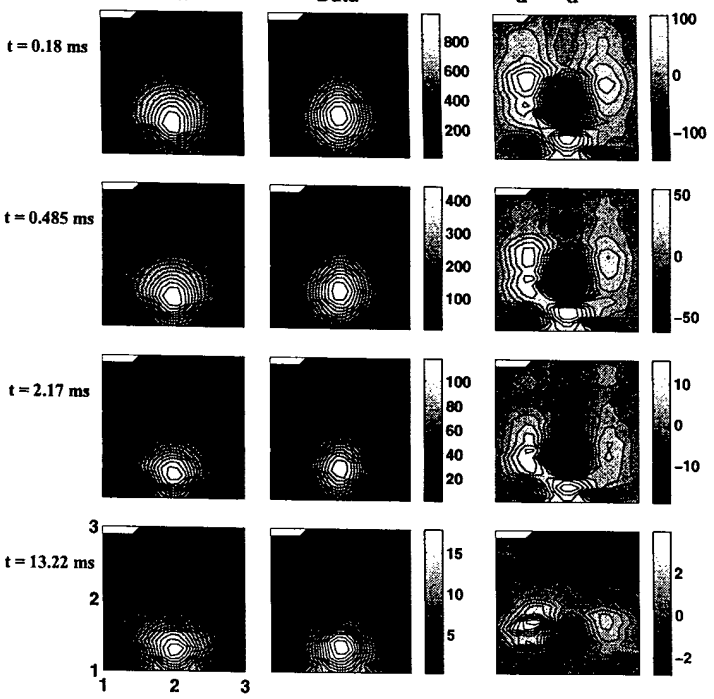

(b)

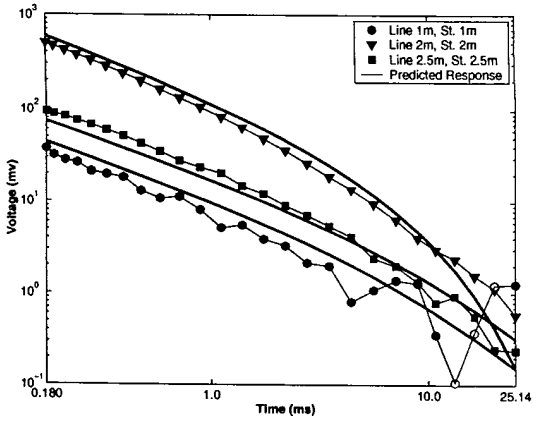

(c) Location and Orientation

	m_o	m_{rec}	m_{exp}
Northing (m)	1.69	1.61	1.74
Easting (m)	1.98	1.99	2.00
Z (m)	0.933	0.866	0.97
ϕ (degrees)	45	0.0	~ 0
θ (degrees)	45	55.6	~ 52

(d) Decay Parameters and Diagnostics

m_i	m_o	m_{rec}
k_1	120.09	166.02
α_1	0.020	0.020
β_1	1.00	0.74
γ_1	23.80	28.69
k_2	120.09	101.49
α_2	0.020	0.020
β_2	1.00	0.94
γ_2	23.80	7.26

	Result	Conclusion
$\bar{\beta}$	0.84	Permeable
k_1/k_2	1.64	Rod-like
β_1/β_2	0.79	Rod-like

Figure 33: Recovered parameters for the field data inversion of a 155mm projectile.

155 mm: $\theta = 90$ degrees, $Z = 91cm$

(a)

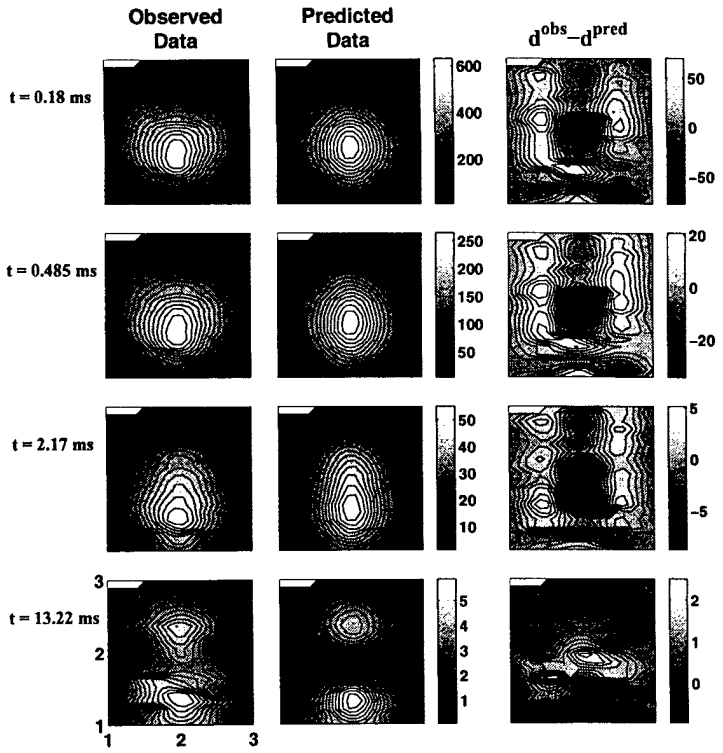

(b)

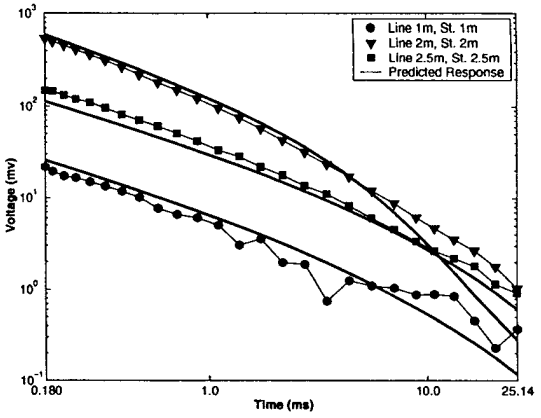

(c) Location and Orientation

	m_o	m_{rec}	m_{exp}
Northing (m)	1.84	1.79	1.92
Easting (m)	2.00	2.01	2.00
Z (m)	1.101	0.925	0.91
ϕ (degrees)	45	0.0	~ 0
θ (degrees)	45	83.9	~ 90

(d) Decay Parameters and Diagnostics

m_i	m_o	m_{rec}
k_1	199.48	181.12
α_1	0.020	0.020
β_1	1.05	0.66
γ_1	11.84	18.63
k_2	199.48	110.09
α_2	0.020	0.020
β_2	1.05	0.88
γ_2	11.84	4.55

	Result	Conclusion
$\bar{\beta}$	0.77	Permeable
k_1/k_2	1.65	Rod-like
β_1/β_2	0.76	Rod-like

Figure 34: Recovered parameters for the field data inversion of a 155mm projectile.

105 mm: $\theta = 0$ degrees (vertical), $Z = 86cm$

(a)

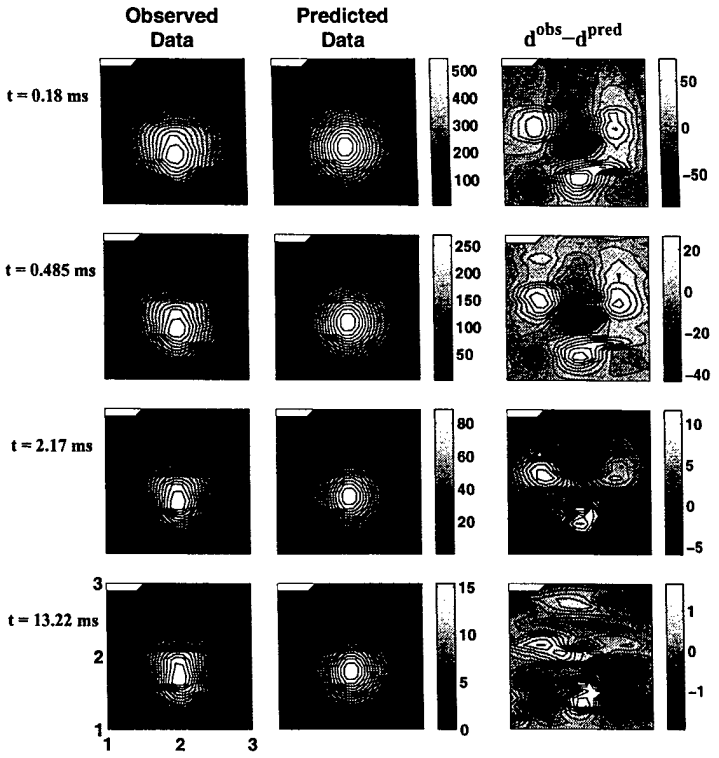

(b)

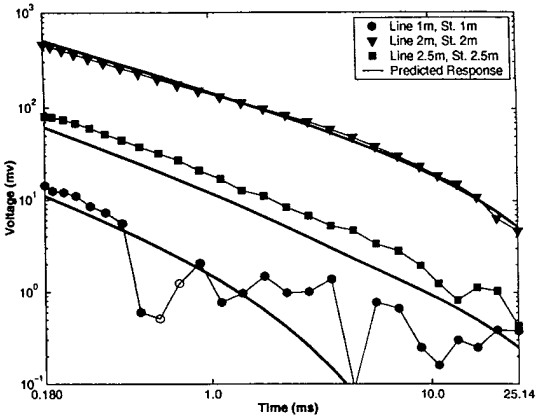

(c) Location and Orientation

	m_o	m_{rec}	m_{exp}
Northing (m)	1.82	1.80	1.88
Easting (m)	2.00	2.02	2.00
Z (m)	0.956	0.957	0.855
ϕ (degrees)	45	39.1	~ 0
θ (degrees)	45	0.0	~ 0

(d) Decay Parameters and Diagnostics

m_i	m_o	m_{rec}
k_1	130.34	138.52
α_1	0.001	0.001
β_1	0.61	0.69
γ_1	16.74	22.52
k_2	130.34	49.89
α_2	0.001	0.020
β_2	0.61	0.98
γ_2	16.74	2.00

	Result	Conclusion
$\bar{\beta}$	0.84	Permeable
k_1/k_2	2.78	Rod-like
β_1/β_2	0.71	Rod-like

Figure 35: Recovered parameters for the field data inversion of a 105mm projectile.

105 mm: $\theta = 90$ degrees (horizontal), $Z = 87cm$

(a)

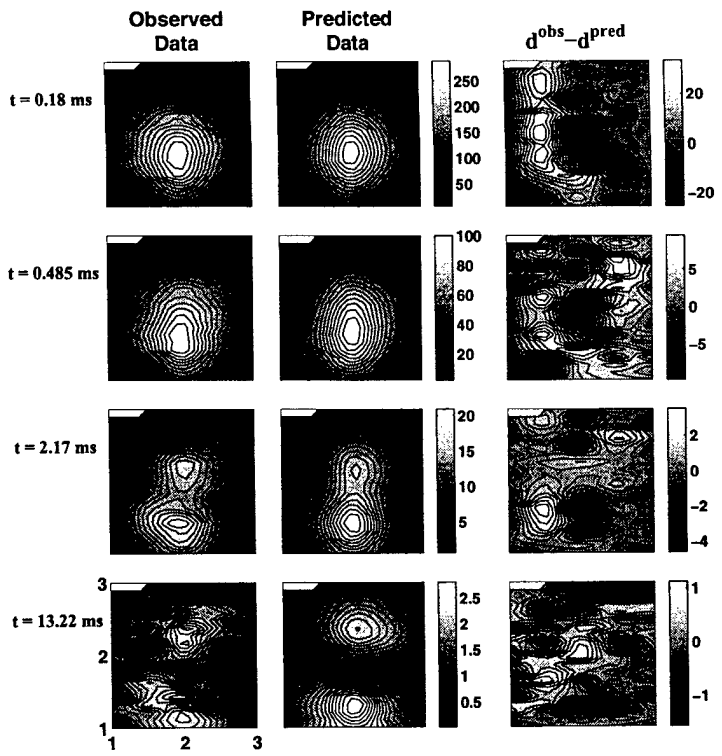

(b)

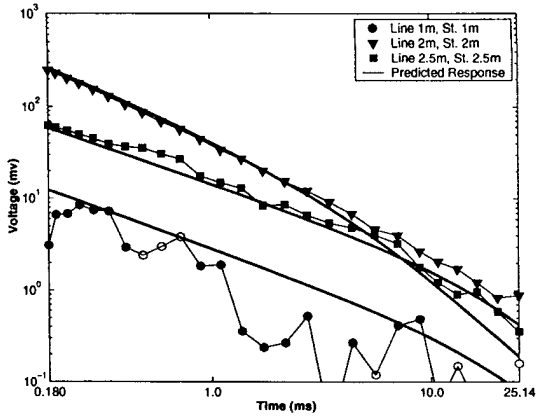

(c) Location and Orientation

	m_o	m_{rec}	m_{exp}
Northing (m)	1.83	1.77	1.83
Easting (m)	2.04	2.03	2.00
Z (m)	1.101	0.915	0.87
ϕ (degrees)	45	8.5	~ 0
θ (degrees)	45	84.5	~ 90

(d) Decay Parameters and Diagnostics

m_i	m_o	m_{rec}
k_1	72.01	82.94
α_1	0.020	0.001
β_1	1.18	0.70
γ_1	9.94	22.90
k_2	72.01	32.22
α_2	0.020	0.011
β_2	1.18	1.08
γ_2	9.94	5.71

	Result	Conclusion
$\bar{\beta}$	0.89	Permeable
k_1/k_2	2.57	Rod-like
β_1/β_2	0.65	Rod-like

Figure 36: Recovered parameters for the field data inversion of a 105mm projectile.

105 mm: $\theta = 59$ degrees, $Z = 89cm$

(a)

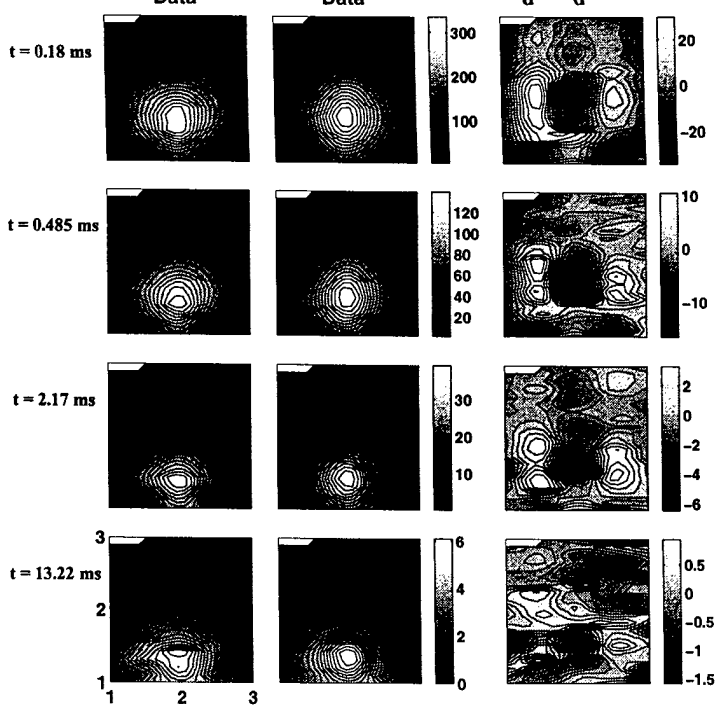

(b)

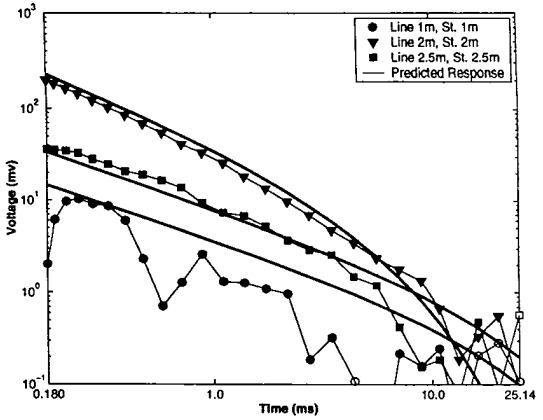

(c) Location and Orientation

	m_o	m_{rec}	m_{exp}
Northing (m)	1.71	1.65	1.81
Easting (m)	2.01	2.02	2.00
Z (m)	0.987	0.887	0.89
ϕ (degrees)	45	16.5	~ 0
θ (degrees)	45	60.6	~ 59

(d) Decay Parameters and Diagnostics

m_i	m_o	m_{rec}
k_1	55.31	71.19
α_1	0.014	0.004
β_1	1.04	0.64
γ_1	21.07	20.36
k_2	55.31	32.15
α_2	0.014	0.020
β_2	1.04	1.07
γ_2	21.07	5.81

	Result	Conclusion
$\bar{\beta}$	0.86	Permeable
k_1/k_2	2.21	Rod-like
β_1/β_2	0.60	Rod-like

Figure 37: Recovered parameters for the field data inversion of a 105mm projectile.

105 mm: $\theta = 40$ degrees, $Z = 89cm$

(a)

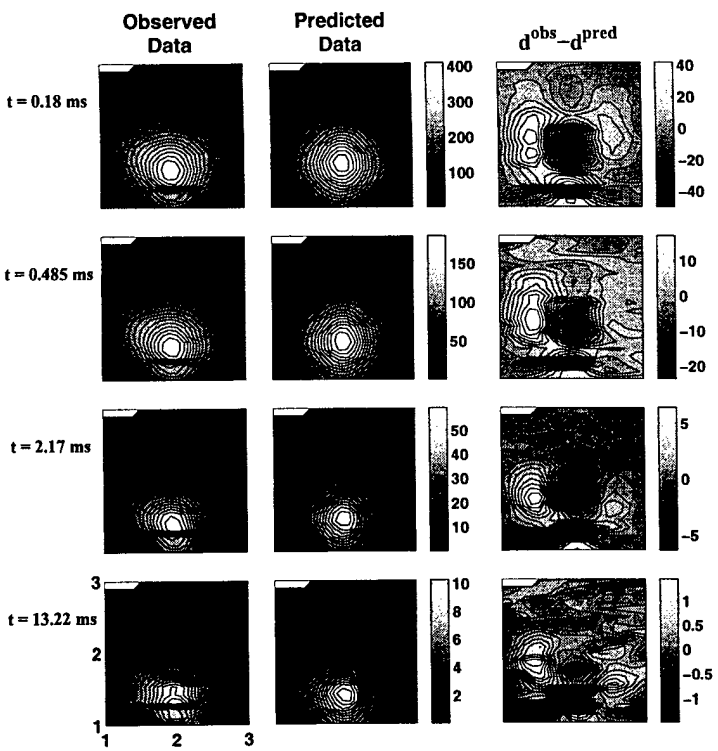

(b)

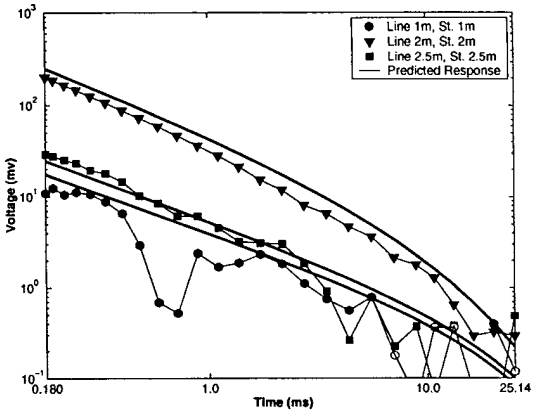

(c) Location and Orientation

	m_o	m_{rec}	m_{exp}
Northing (m)	1.68	1.58	1.81
Easting (m)	1.97	1.98	2.00
Z (m)	0.892	0.826	0.885
ϕ (degrees)	45	19.0	~ 0
θ (degrees)	45	43.9	~ 40

(d) Decay Parameters and Diagnostics

m_i	m_o	m_{rec}
k_1	46.98	53.63
α_1	0.001	0.001
β_1	0.84	0.59
γ_1	19.38	18.20
k_2	46.98	31.58
α_2	0.001	0.020
β_2	0.84	1.05
γ_2	19.38	10.32

	Result	Conclusion
$\bar{\beta}$	0.82	Permeable
k_1/k_2	1.70	Rod-like
β_1/β_2	0.55	Rod-like

Figure 38: Recovered parameters for the field data inversion of a 105mm projectile.

Stokes Mortar: $\theta = 54$ degrees, $Z = 73cm$

(a)

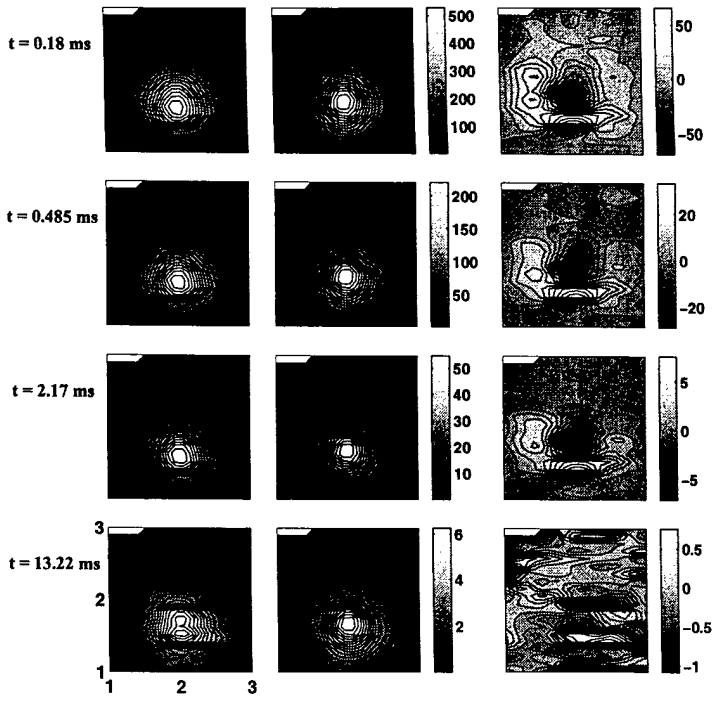

(b)

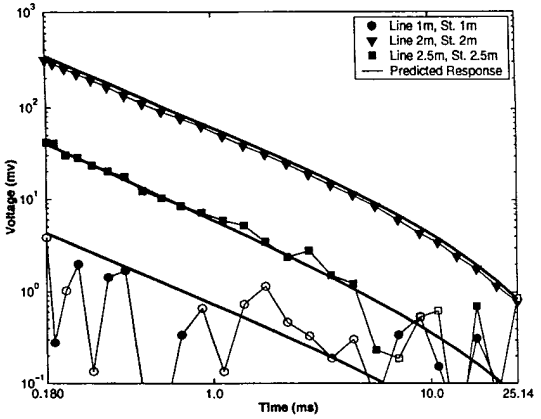

(c) Location and Orientation

	m_o	m_{rec}	m_{exp}
Northing (m)	1.77	1.88	1.99
Easting (m)	2.03	2.05	2.00
Z (m)	0.716	0.764	0.73
ϕ (degrees)	45	7.9	~ 0
θ (degrees)	45	50.3	~ 54

(d) Decay Parameters and Diagnostics

m_i	m_o	m_{rec}
k_1	18.15	51.78
α_1	0.020	0.020
β_1	0.95	0.88
γ_1	29.50	19.13
k_2	18.15	6.02
α_2	0.020	0.015
β_2	0.95	1.32
γ_2	29.50	28.78

	Result	Conclusion
$\bar{\beta}$	1.10	Permeable
k_1/k_2	8.60	Rod-like
β_1/β_2	0.66	Rod-like

Figure 39: Recovered parameters for the field data inversion of a stokes mortar.

Stokes Mortar: $\theta = 0$ degrees (vertical), $Z = 73cm$

(a)

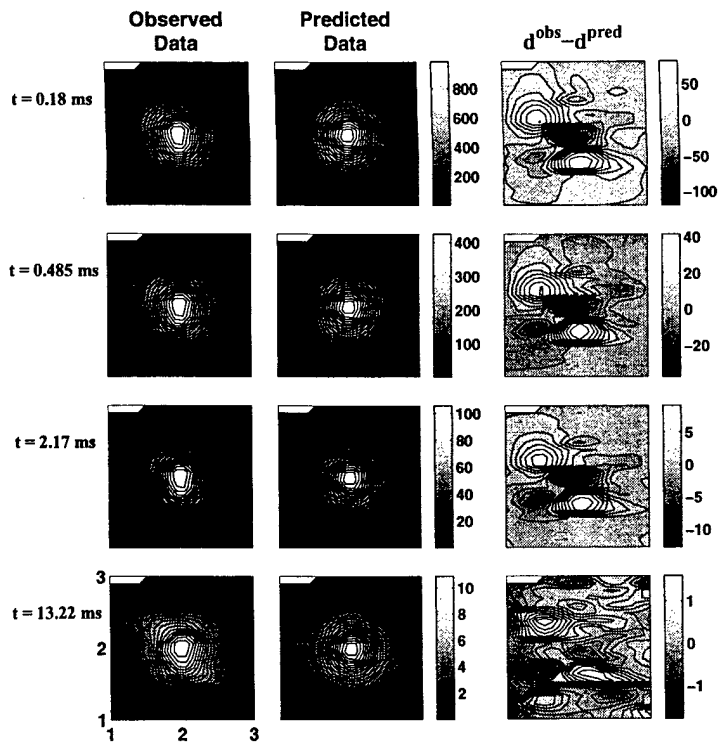

(b)

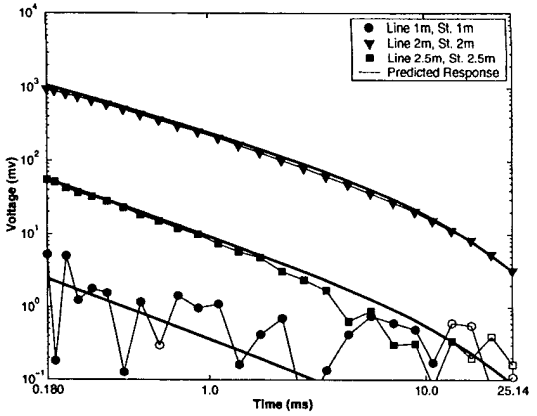

(c) Location and Orientation

	m_o	m_{rec}	m_{exp}
Northing (m)	1.97	1.97	1.97
Easting (m)	1.99	2.02	2.00
Z (m)	0.687	0.687	0.73
ϕ (degrees)	45	46.1	~ 0
θ (degrees)	45	0.0	~ 0

(d) Decay Parameters and Diagnostics

m_i	m_o	m_{rec}
k_1	33.89	38.08
α_1	0.020	0.016
β_1	0.89	0.87
γ_1	18.13	15.64
k_2	33.89	5.82
α_2	0.020	0.001
β_2	0.89	1.17
γ_2	18.13	14.60

	Result	Conclusion
$\bar{\beta}$	1.02	Permeable
k_1/k_2	6.54	Rod-like
β_1/β_2	0.74	Rod-like

Figure 40: Recovered parameters for the field data inversion of a stokes mortar.

Stokes Mortar: $\theta = 90$ degrees (horizontal), $Z = 73cm$

(a)

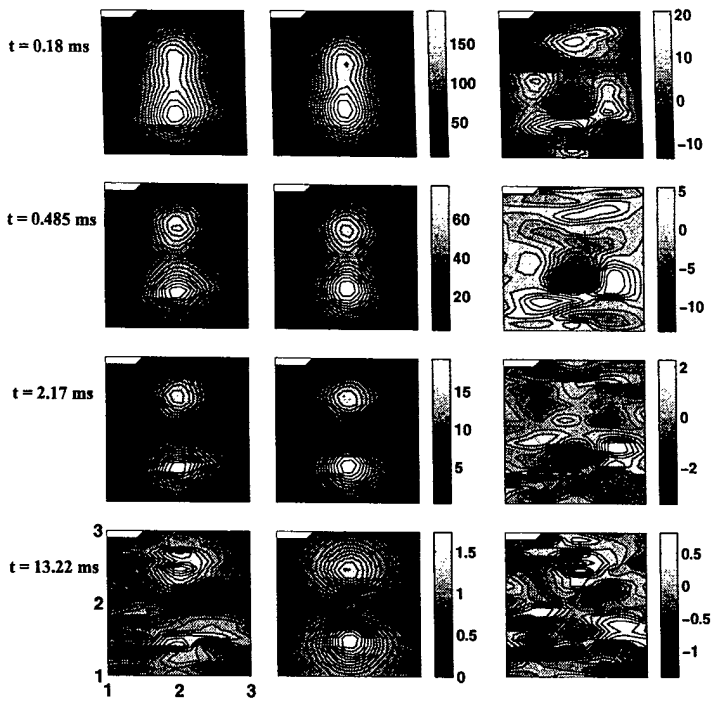

(b)

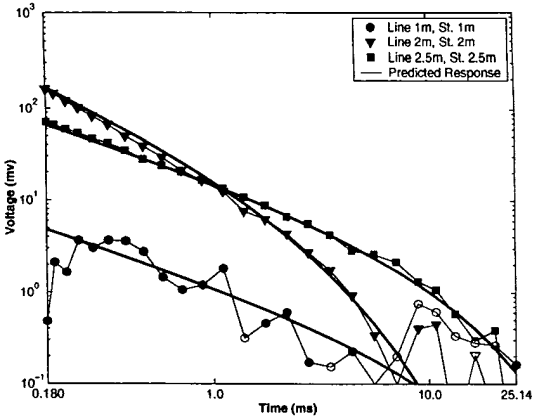

(c) Location and Orientation

	m_o	m_{rec}	m_{exp}
Northing (m)	1.93	1.95	2.00
Easting (m)	2.04	2.03	2.00
Z (m)	1.103	0.788	0.73
ϕ (degrees)	45	0.0	~ 0
θ (degrees)	45	86.3	~ 90

(d) Decay Parameters and Diagnostics

m_i	m_o	m_{rec}
k_1	29.70	56.80
α_1	0.001	0.020
β_1	1.29	0.77
γ_1	10.02	11.40
k_2	29.70	6.15
α_2	0.001	0.020
β_2	1.29	1.29
γ_2	10.02	3.39

	Result	Conclusion
$\bar{\beta}$	1.03	Permeable
k_1/k_2	9.24	Rod-like
β_1/β_2	0.59	Rod-like

Figure 41: Recovered parameters for the field data inversion of a stokes mortar.

81 mm: $\theta = 0$ degrees (vertical), $Z = 73cm$

(a)

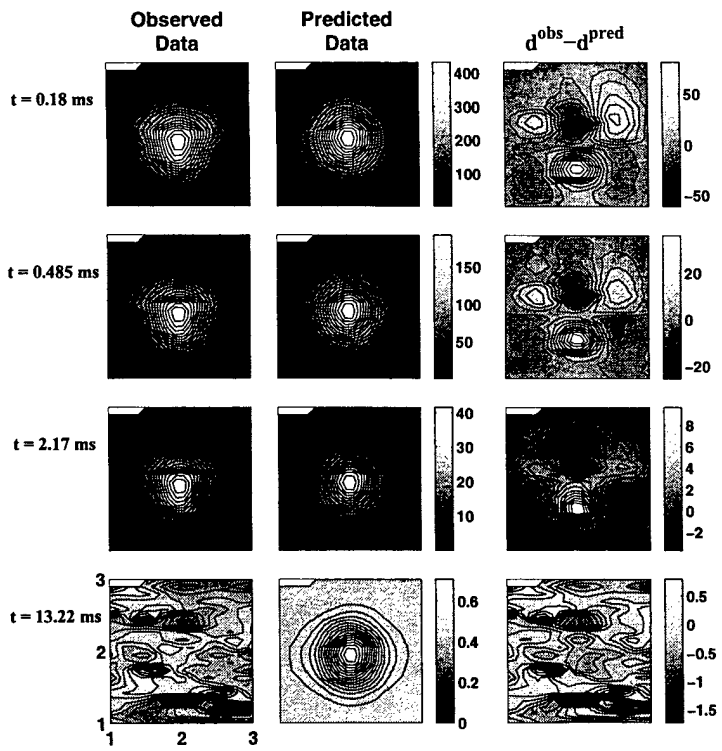

(b)

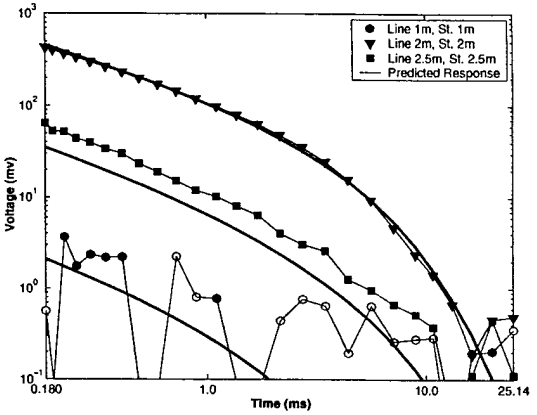

(c) Location and Orientation

	m_o	m_{rec}	m_{exp}
Northing (m)	1.93	1.94	2.00
Easting (m)	2.01	1.99	2.00
Z (m)	0.756	0.828	0.73
ϕ (degrees)	45	47.7	~ 0
θ (degrees)	45	0.0	~ 0

(d) Decay Parameters and Diagnostics

m_i	m_o	m_{rec}
k_1	38.14	49.56
α_1	0.001	0.001
β_1	0.58	0.74
γ_1	2.75	4.05
k_2	38.14	10.27
α_2	0.001	0.020
β_2	0.58	0.97
γ_2	2.75	2.00

	Result	Conclusion
$\bar{\beta}$	0.85	Permeable
k_1/k_2	4.83	Rod-like
β_1/β_2	0.77	Rod-like

Figure 42: Recovered parameters for the field data inversion of an 81 mm mortar without fins.

81 mm: $\theta = 43$ degrees, $Z = 74cm$

(a)

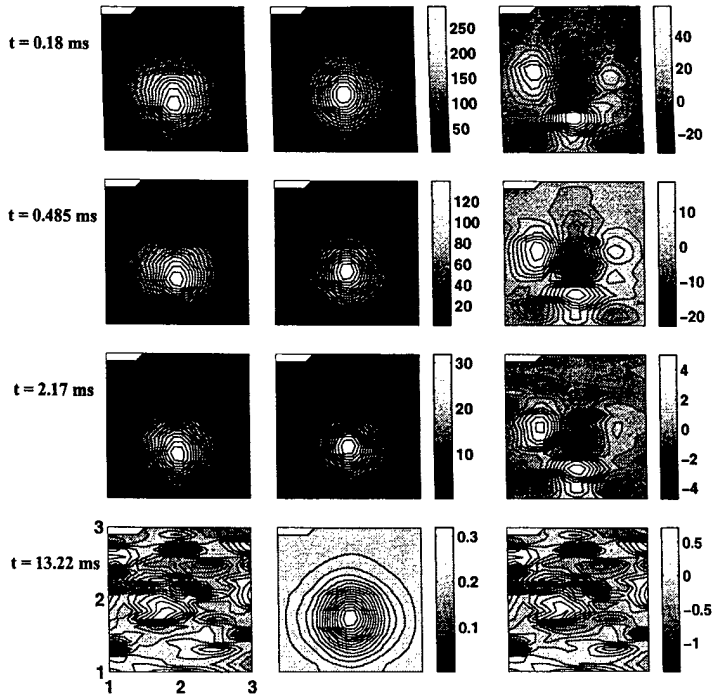

(b)

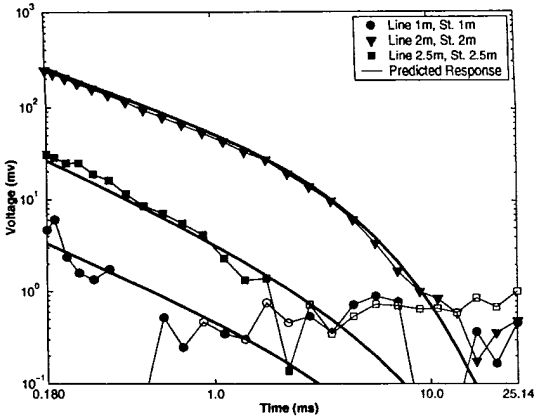

(c) Location and Orientation

	m_o	m_{rec}	m_{exp}
Northing (m)	1.83	1.86	1.86
Easting (m)	1.98	2.01	2.00
Z (m)	0.797	0.755	0.74
ϕ (degrees)	45	0.0	~ 0
θ (degrees)	45	38.2	~ 43

(d) Decay Parameters and Diagnostics

m_i	m_o	m_{rec}
k_1	25.38	32.50
α_1	0.001	0.006
β_1	0.75	0.60
γ_1	3.95	3.10
k_2	25.38	7.42
α_2	0.001	0.010
β_2	0.75	1.19
γ_2	3.95	5.94

	Result	Conclusion
$\bar{\beta}$	0.90	Permeable
k_1/k_2	4.38	Rod-like
β_1/β_2	0.50	Rod-like

Figure 43: Recovered parameters for the field data inversion of an 81 mm mortar without fins.

81 mm: $\theta = 90$ degrees (horizontal), $Z = 73cm$

(a)

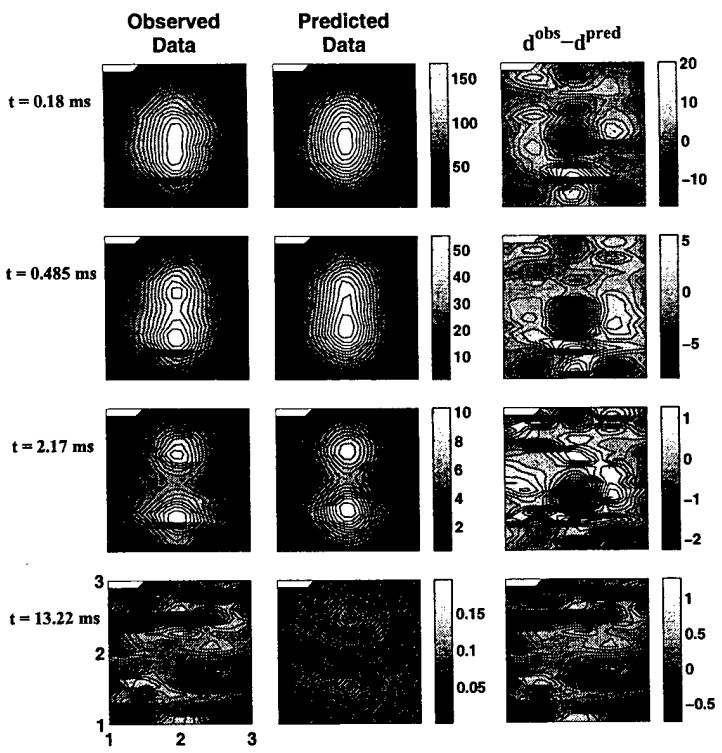

(b)

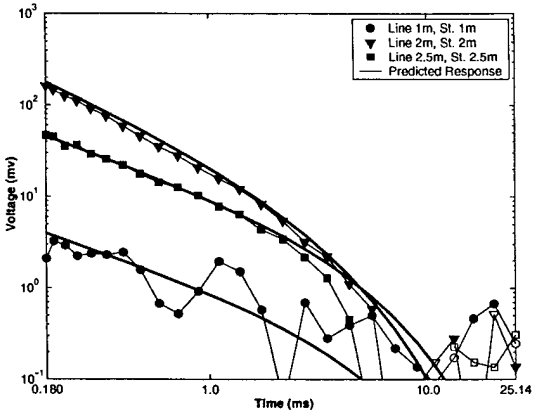

(c) Location and Orientation

	m_o	m_{rec}	m_{exp}
Northing (m)	1.97	1.97	2.00
Easting (m)	1.98	1.99	2.00
Z (m)	1.105	0.808	0.73
ϕ (degrees)	45	1.9	~ 0
θ (degrees)	45	86.8	~ 90

(d) Decay Parameters and Diagnostics

m_i	m_o	m_{rec}
k_1	39.63	39.71
α_1	0.001	0.001
β_1	1.13	0.68
γ_1	3.32	4.26
k_2	39.63	8.86
α_2	0.001	0.003
β_2	1.13	1.13
γ_2	3.32	3.27

	Result	Conclusion
$\bar{\beta}$	0.90	Permeable
k_1/k_2	4.48	Rod-like
β_1/β_2	0.60	Rod-like

Figure 44: Recovered parameters for the field data inversion of an 81 mm mortar without fins.

60 mm: $\theta = 57$ degrees (vertical), $Z = 58cm$

(a)

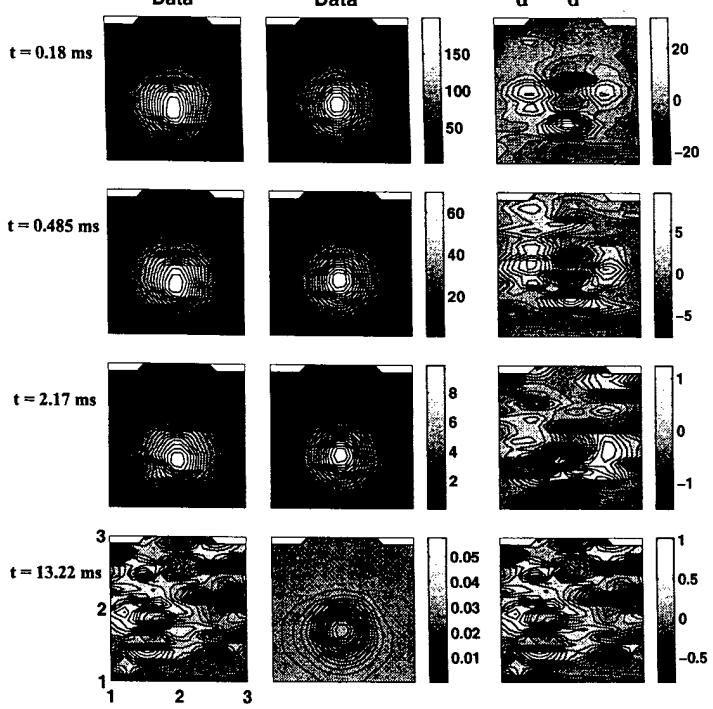

(b)

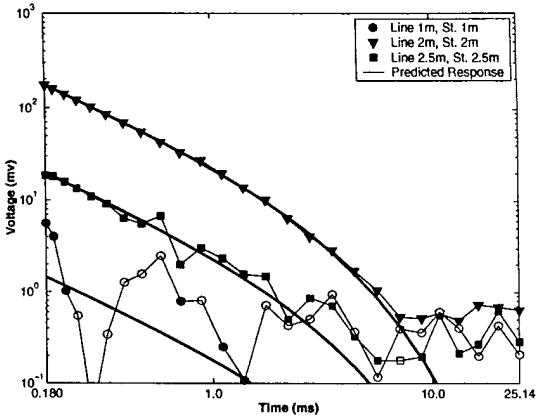

(c) Location and Orientation

	m_o	m_{rec}	m_{exp}
Northing (m)	1.85	1.92	2.00
Easting (m)	1.96	2.03	2.00
Z (m)	0.752	0.700	0.58
ϕ (degrees)	45	14.5	~ 0
θ (degrees)	45	51.7	~ 57

(d) Decay Parameters and Diagnostics

m_i	m_o	m_{rec}
k_1	7.82	10.89
α_1	0.020	0.014
β_1	1.09	0.94
γ_1	3.67	3.24
k_2	7.82	2.84
α_2	0.020	0.018
β_2	1.09	1.29
γ_2	3.67	2.96

	Result	Conclusion
$\bar{\beta}$	1.11	Permeable
k_1/k_2	3.84	Rod-like
β_1/β_2	0.73	Rod-like

Figure 45: Recovered parameters for the field data inversion of a 60mm mortar.

60 mm: $\theta = 90$ degrees (horizontal), $Z = 58cm$

(a)

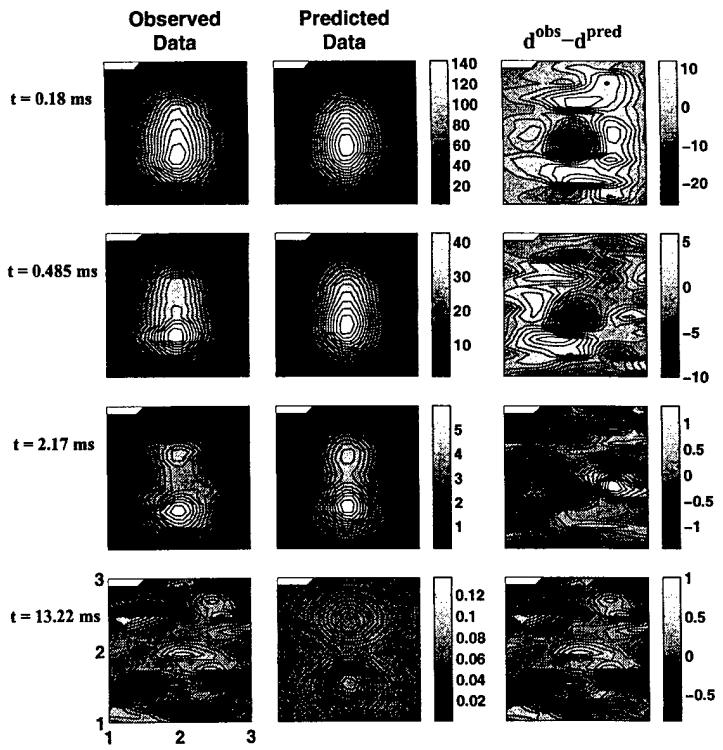

(b)

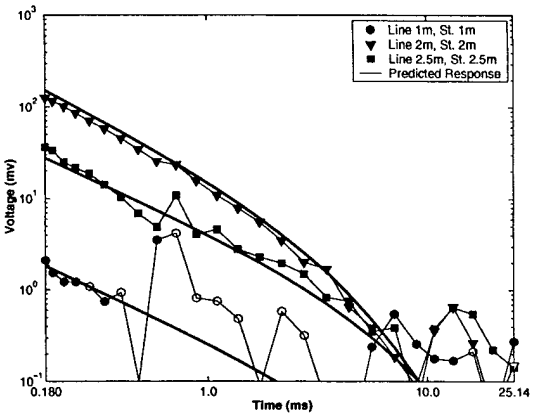

(c) Location and Orientation

	m_o	m_{rec}	m_{exp}
Northing (m)	1.92	1.92	2.00
Easting (m)	2.04	2.01	2.00
Z (m)	1.003	0.684	0.58
ϕ (degrees)	45	1.9	~ 0
θ (degrees)	45	84.0	~ 90

(d) Decay Parameters and Diagnostics

m_i	m_o	m_{rec}
k_1	16.51	9.81
α_1	0.015	0.001
β_1	1.25	0.97
γ_1	3.81	5.99
k_2	16.51	2.74
α_2	0.015	0.002
β_2	1.25	1.22
γ_2	3.81	3.03

	Result	Conclusion
$\bar{\beta}$	1.10	Permeable
k_1/k_2	3.58	Rod-like
β_1/β_2	0.79	Rod-like

Figure 46: Recovered parameters for the field data inversion of a 60mm mortar.

60 mm: $\theta = 0$ degrees (vertical, nose up), $Z = 59cm$

(a)

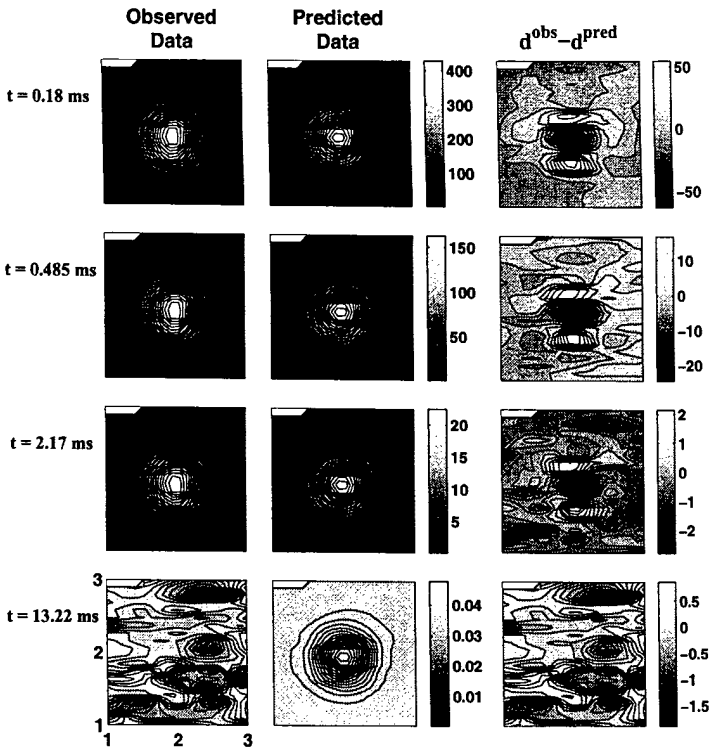

(b)

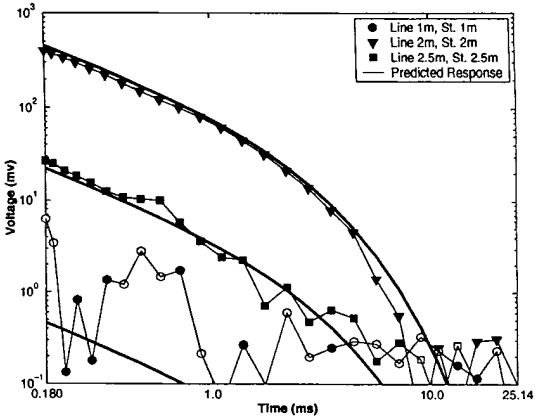

(c) Location and Orientation

	m_o	m_{rec}	m_{exp}
Northing (m)	1.94	1.98	2.00
Easting (m)	2.01	2.05	2.00
Z (m)	0.666	0.510	0.59
ϕ (degrees)	45	64.2	~ 0
θ (degrees)	45	44.6	~ 0

(d) Decay Parameters and Diagnostics

m_i	m_o	m_{rec}
k_1	13.61	5.96
α_1	0.001	0.001
β_1	0.79	0.83
γ_1	2.05	2.34
k_2	13.61	1.88
α_2	0.001	0.007
β_2	0.79	0.97
γ_2	2.05	2.69

	Result	Conclusion
$\bar{\beta}$	0.90	Permeable
k_1/k_2	3.17	Rod-like
β_1/β_2	0.86	Rod-like

Figure 47: Recovered parameters for the field data inversion of a 60mm mortar.

60 mm: $\theta = 0$ degrees (vertical, nose down), $Z = 59cm$

(a)

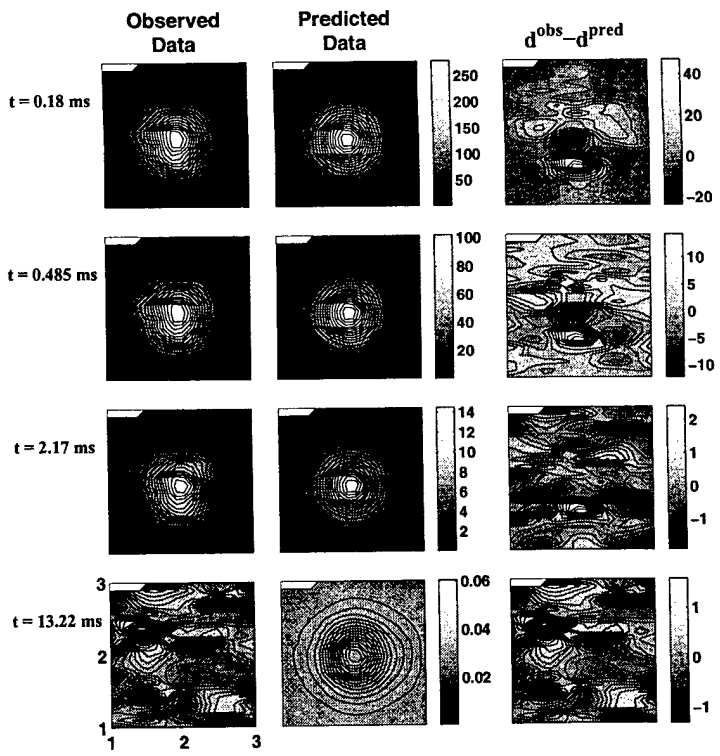

(b)

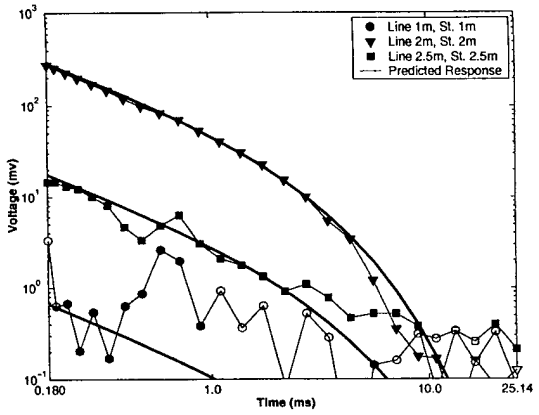

(c) Location and Orientation

	m_o	m_{rec}	m_{exp}
Northing (m)	1.93	1.96	2.00
Easting (m)	2.00	2.05	2.00
Z (m)	0.698	0.607	0.59
ϕ (degrees)	45	57.3	~ 0
θ (degrees)	45	35.9	~ 0

(d) Decay Parameters and Diagnostics

m_i	m_o	m_{rec}
k_1	9.78	6.69
α_1	0.001	0.001
β_1	0.88	0.90
γ_1	2.80	2.75
k_2	9.78	2.68
α_2	0.001	0.002
β_2	0.88	0.96
γ_2	2.80	3.52

	Result	Conclusion
$\bar{\beta}$	0.93	Permeable
k_1/k_2	2.49	Rod-like
β_1/β_2	0.94	Rod-like

Figure 48: Recovered parameters for the field data inversion of a 60mm mortar.

4 References

Arfken, G., 1985, Mathematical Methods for Physicists, 3rd Edition: Academic Press.

Bard, Y., 1974, Nonlinear Parameter Estimation: Academic Press.

Baum, C.E., 1997, Discrimination of Buried Targets Via the Singularity Expansion: Inverse Problems, **13**, 557-570.

Baum, C.E., 1999, The Magnetic Polarizability Dyadic and Point Symmetry: in Baum, C.E., Ed., Detection and Identification of Visually Obscured Targets, 219-242.

Butler, D., Cespedes, E., O'Neill, K., Arcone, S., Llopis, J., Curtis, J., Cullinane, J., and Meyer, C., 1998, Overview of Science and Technology Program For JPG Phase IV: Proceedings of UXO Forum '98.

Carin, L., 2000, FEM Modelling of the EMI Response of General UXO Targets: Proceedings of UXO/Countermine Forum 2000.

Casey, K.F, and Baertlein, B.A., 1999, An Overview of Electromagnetic Methods In Subsurface Detection: in Baum, C.E., Ed., Detection and Identification of Visually Obscured Targets, 9-46.

Collins, L., Gao, P., Geng, N., Carin, L., Keiswetter, D., and Won, I.J., 1999, Discrimination of UXO-Like Metal Targets Using WideBand Electromagnetic Induction: Proceedings of UXO Forum '99.

Damarla, T., Ressler, M., 2000, Issues in UXO Detection Using Template Matching: Proceedings of UXO/Countermine Forum 2000.

Das, Y., McFee, J.E., Toews, J. and Stuart, G.C., 1990, Analysis of an Electromagnetic Induction Detector For Real-Time Location of Buried Objects: IEEE Transactions on Geoscience and Remote Sensing, **28**, no.3, 278-287.

Dennis, J.E., and Schnabel, R.B., 1983, Numerical Methods for Unconstrained Optimization and Nonlinear Equations: Prentice-Hall.

Gill, P.E., Murray, W., Wright, M.H., 1981, Practical Optimization: Academic Press.

Grimm, R.E., Blohm, M.W., Lavely, E.M., 1997, UXO Characterization Using Multicomponent, Multichannel Time-Domain Electromagnetic Induction: Proceedings of UXO Forum '97.

Grimm, R.E., 2000, UXO Discrimination Using MTADS: Joint EM/Magnetic Ellipsoid Modelling and Neural-Network Analysis: Proceedings of UXO/Countermine Forum 2000.

Haber, E., Ascher, U. M., Oldenburg, D. W., 2000, Fast Simulation of 3D Electromagnetic Problems Using Potentials: Journal of Computational Physics, **163**, no. 1, 150-171.

Hiptmair, R., 1998, Multigrid Method For Maxwell's Equations: SIAM Journal of Numerical Analysis, **36**, 204-225.

Jackson, J.D., 1975, Classical Electrodynamics: John Wiley and Sons.

Kaufman, A.A., 1994, Geophysical Field Theory and Method: Academic Press, Inc.

Kaufman, A.A., and Keller, G.V., 1985, Inductive Mining Prospecting: Elsevier.

Kelley, C.T., 1999, Iterative Methods for Optimization: Society for Industrial and Applied Mathematics.

Khadr, N., Barrow, B.J., and Bell, T.H., 1998, Target Shape Classification Using Electromagnetic Induction Sensor Data: Proceedings of UXO Forum '98.

Miller, J.T., 2000, Detection of Copper Rotating Bands on Buried Ordnance Using Wide-Band Electromagnetic Induction: Proceedings of UXO/Countermine Forum 2000.

Pasion, L.R., 1999, Detecting Unexploded Ordnance with Time Domain Electromagnetic Induction, M.Sc. Thesis, University of British Columbia.

Snyder, D.D., MacInnes, S., Urquhart, S., Zonge, K.L., 1999, Possibilities for UXO Classification Using Characteristic Modes Of the Broad-band Electromagnetic Induction Response: Proceedings of A New Technology Applications Conference on the Science and Technology of Unexploded Ordnance Removal and Site Remediation.

A Target Descriptions

Target	Mass (kg)	Length (cm)	Width /Thickness (cm)
155 mm		60	15.5
105 mm	14.05	21	10.5
Stokes Mortar	3.55	36	16
81 mm (no fins)	3.3	26	8.1
Rusted Mortar	2.85	36	29
60 mm	1.352	26	6
37 mm	0.839	11.4	3.6
Disk	0.88	8 (diameter)	2.2 thick
Scrap 1	0.08	13 (diameter)	~2 thick
Scrap 2	0.026	6.4	6.3
Scrap 3	0.055	11	6.4
Scrap 4	0.091	19.4	2.5
Scrap 5	0.172	16.5	3
Scrap 6	0.256	21	4.8
Scrap 7	0.069	12.5	2
Scrap 8	0.075	7	3
Scrap 9		19	9
Scrap 10	0.032	5	3.5
Scrap 12	0.186	9.6	4.4
Rocket Fins (Scrap 13)	0.83	21.4	6.5
Blown Mortar (Scrap 14)	0.939	16	7
Scrap 15	0.431	16	5.6

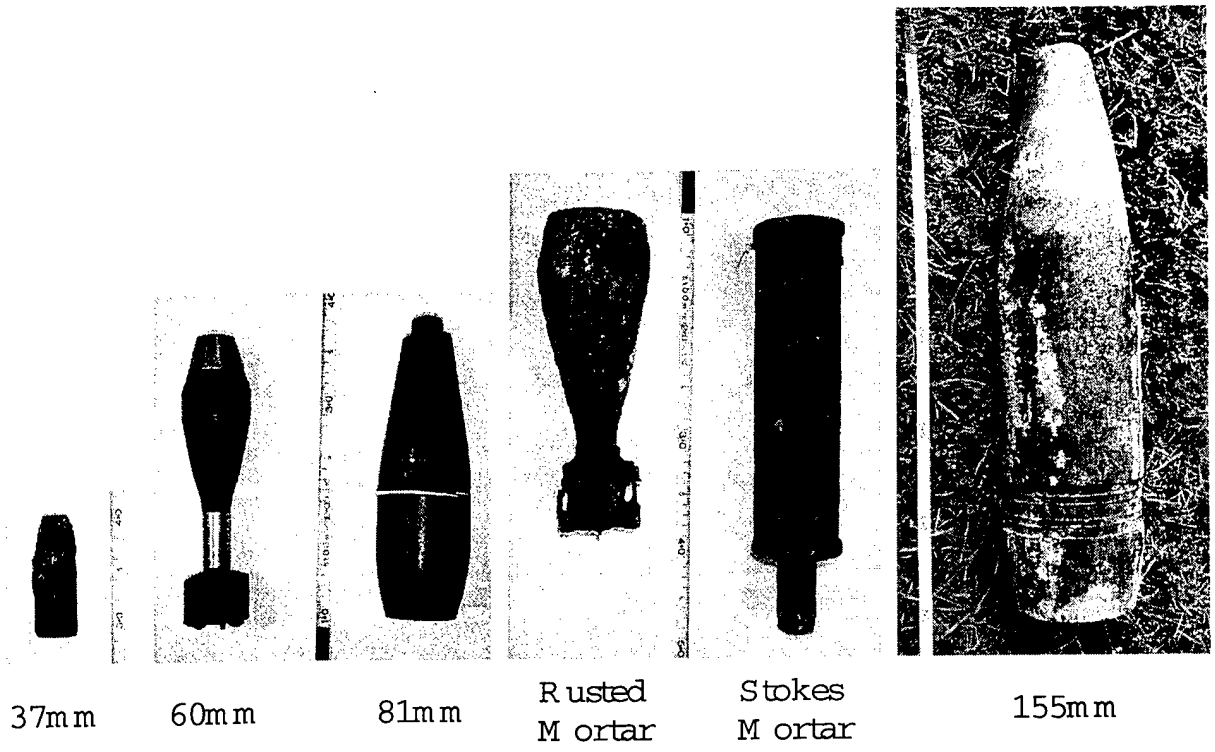

Figure 49: UXO targets analysed.

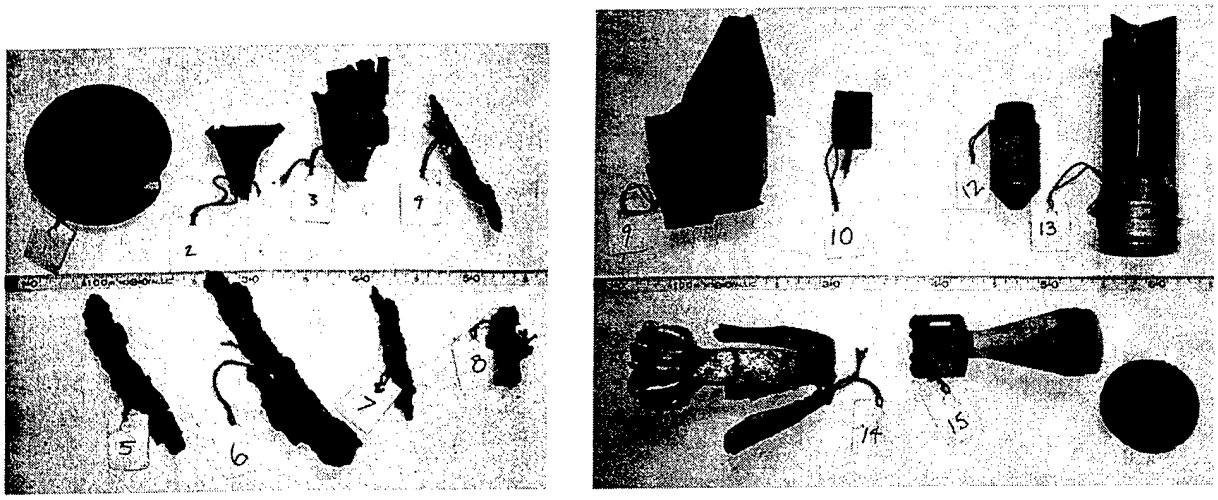

Figure 50: Scrap targets analysed.

B Recovered Polarization Dyadic for Various Targets

The magnetic polarization dyadic for the TEM problem is defined as

$$\bar{\bar{\mathbf{M}}} = \begin{bmatrix} L_2(t) & 0 & 0 \\ 0 & L_2(t) & 0 \\ 0 & 0 & L_1(t) \end{bmatrix} \tag{33}$$

where

$$\begin{aligned} L_1(t) &= k_1 (t+\alpha_1)^{-\beta_1} e^{-t/\gamma_1} \\ L_2(t) &= k_2 (t+\alpha_2)^{-\beta_2} e^{-t/\gamma_2} \end{aligned} \tag{34}$$

The recovered magnetic polarization dyadic acquired for a number of targets are reported here. The procedure followed to obtained these results is described in Section 2 of this report. A photo and description of each target can be found in Appendix A.

a)

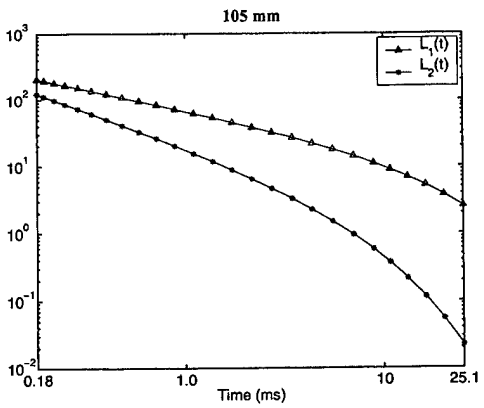

(b) Decay Parameters

m_i	Dipole 1	Dipole 2
k	69.6	20.1
α	0.002	0.005
β	0.64	1.08
γ	20.4	7.59

Figure 51: 105 mm Projectile

a)

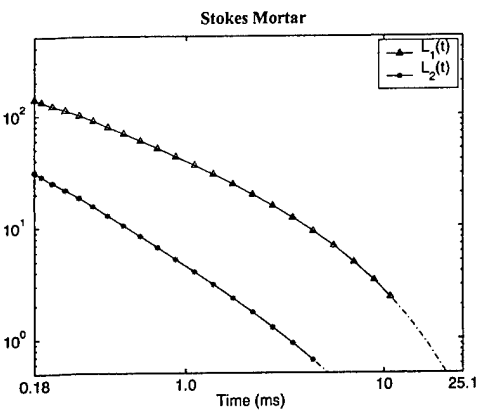

(b) Decay Parameters

m_i	Dipole 1	Dipole 2
k	43.9	4.9
α	0.02	0.001
β	0.73	1.09
γ	9.1	10.8

Figure 52: Stokes Mortar

a)

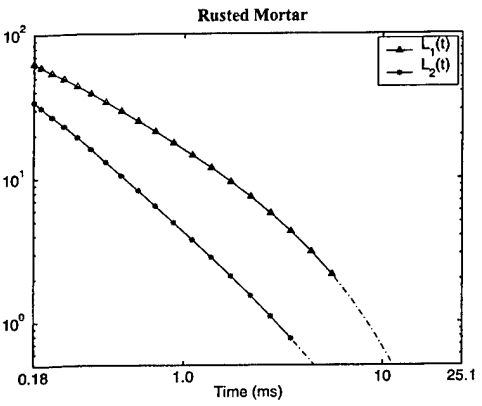

(b) Decay Parameters

m_i	Dipole 1	Dipole 2
k	18.7	4.8
α	0.002	0.001
β	0.73	1.2
γ	6.0	9.1

Figure 53: Rusted Mortar

a)

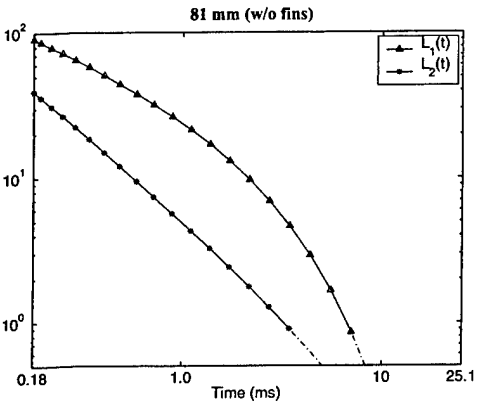

(b) Decay Parameters

m_i	Dipole 1	Dipole 2
k	33.3	5.4
α	0.002	0.001
β	0.62	1.18
γ	2.89	10.9

Figure 54: 81 mm, without fins

a)

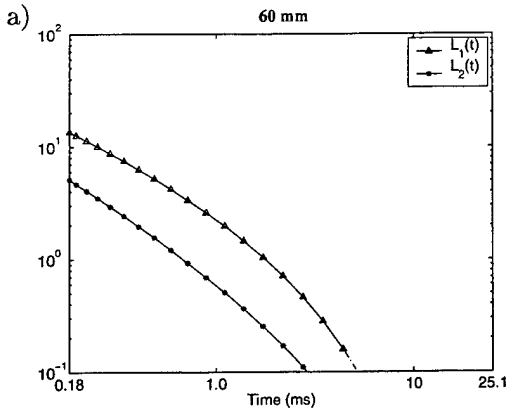

(b) Decay Parameters

m_i	Dipole 1	Dipole 2
k	3.38	0.79
α	0.019	0.02
β	0.90	1.19
γ	2.55	3.59

Figure 55: 60 mm Mortar

a)

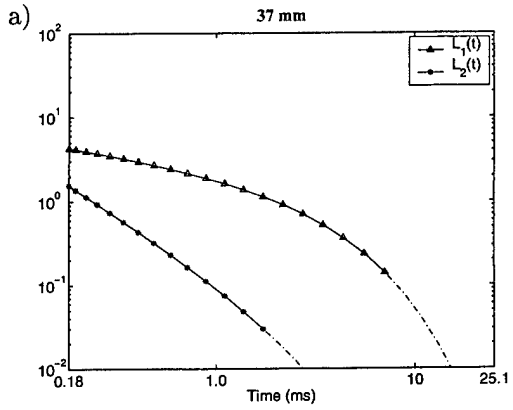

(b) Decay Parameters

m_i	Dipole 1	Dipole 2
k	2.33	0.14
α	0.02	0.001
β	0.40	1.46
γ	3.49	2.36

Figure 56: 37 mm Projectile

a)

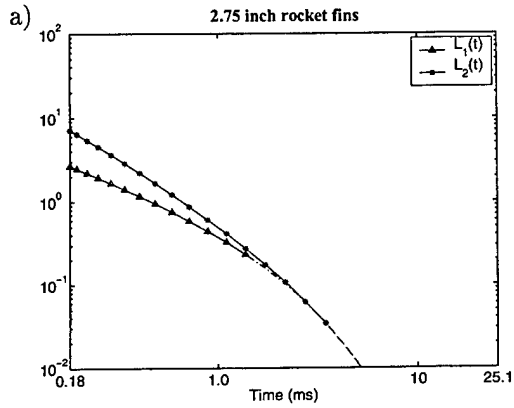

(b) Decay Parameters

m_i	Dipole 1	Dipole 2
k	0.63	0.74
α	0.02	0.02
β	0.94	1.45
γ	2.00	2.75

Figure 57: Fins from a 2.75 inch Rocket

a)

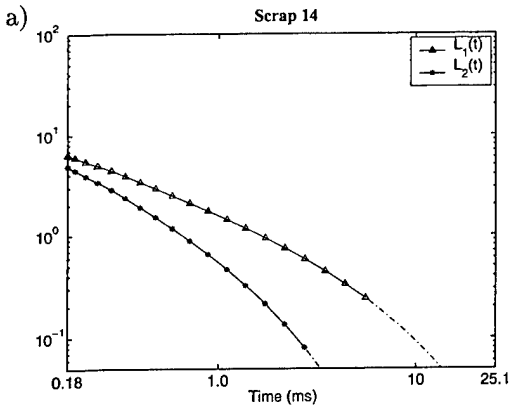

(b) Decay Parameters

m_i	Dipole 1	Dipole 2
k	1.78	0.89
α	0.02	0.02
β	0.80	1.11
γ	8.99	2.14

Figure 58: Scrap 14

a)

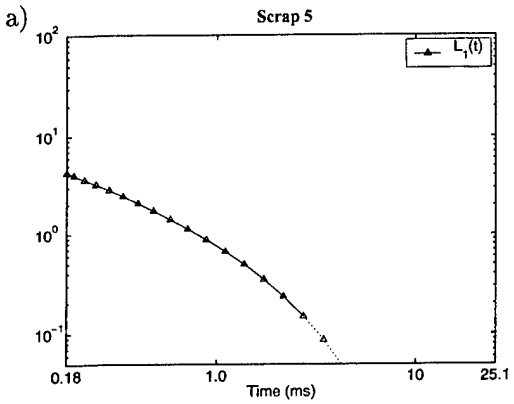

(b) Decay Parameters

m_i	Dipole 1	Dipole 2
k	1.26	na
α	0.02	na
β	0.81	na
γ	2.08	na

Figure 59: Scrap 5. The response of the $\mathbf{m}_2$ dipole did not generate a response above the noise level of the EM63.

a)

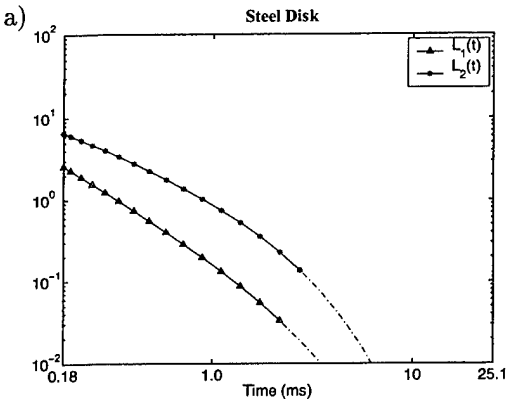

(b) Decay Parameters

m_i	Dipole 1	Dipole 2
k	0.23	1.45
α	0.001	0.02
β	1.44	0.99
γ	2.57	2.00

Figure 60: Steel Disk